UNIVERSIDAD NACIONAL AUTÓNOMA DE MÉXICO
PROGRAMA DE MAESTRÍA Y DOCTORADO EN INGENIERÍA
ENERGÍA - SOLAR FOTOTÉRMICA

NUMERICAL STUDY OF BUBBLE DYNAMICS

TESIS
QUE PARA OPTAR POR EL GRADO DE:
DOCTOR EN INGENIERÍA

PRESENTA:
SAÚL PIEDRA GONZÁLEZ

TUTOR:
DR. EDUARDO RAMOS MORA, IER-UNAM

MÉXICO D.F. JUNIO 2015

Contents

List of Figures

Resumen

En este estudio se presenta un análisis numérico de la dinámica de burbujas y gotas para diferentes condiciones de flujo. La tesis está enfocada a desarrollar herramientas numéricas eficientes para analizar el flujo generado por burbujas y gotas en un fluido viscoso y los mecanismos de transferencia de calor y masa en este tipo de flujos. La implemetación numérica desarrollada en este trabajo está basada en los métodos de fronteras inmersas, particularmente usando el método de "front-tracking" para representar una interfase entre dos fluidos inmiscibles, encontrando las fuerzas interfaciales y calculando las propiedades materiales de cada fluido en todo el dominio, esto permite resolver un solo conjunto de ecuaciones de conservación. En el primer Capítulo, se presentan la formulación matemática de los métodos de fronteras inmersas, su acoplamiento con las ecuaciones de Navier-Stokes y la estrategia de integración numérica. En el Capítulo 2, se reportan los resultados de las simulaciones numéricas en dos dimensiones del flujo generado por el ascenso de una burbuja, así como la comparación con resultados experimentales en una celda Hele-Shaw que fueron realizados como parte del proyecto. Los resultados demuestran que a pesar de que el modelo bidimensional logra capturar cualitativamente las principales caraterísticas del flujo de una burbuja en una celda Hele-Shaw, existen diferencias cuantitativas muy significativas en las diferentes variables que gobiernan el flujo. El código numérico fue extendido a tres dimensiones y diferentes simulaciones numéricas se presentan en el Capítulo 3. En la primera parte se muestran los resultados obtenidos para bajos números de Reynolds, en la segunda parte se reportan simulaciones numéricas de burbujas de aire en agua en donde la relación de densidades es del orden de 10^3 y en donde el número de Reynolds es del orden 10^2-10^3. Además se muestra la comparación con experimentos reportados en la literatura. En la parte final de este capítulo se presentan simulaciones del flujo generado por múltiples burbujas ascendiendo en un fluido, demostrando la capacidad de la implementación numérica desarrollada para la solución de flujos más complejos. En el Capítulo 4 se muestran los resultados para simulaciones del flujo de burbujas en un canal, analizando principalmente el efecto sobre la transferencia de calor debido a la presencia de las burbujas. En el Capítulo 5, se describe el desarrollo e implementación de un modelo de evaporación para gotas usando el método de "front-trackin". El modelo se valida mediante una solución analítica de las ecuaciones de conservación para el fenómeno de evaporación en un contenedor parcialmente lleno de líquido. En la segunda parte del capítulo se presentan diferentes simulaciones numéricas de la evaporación de gotas. Finalmente, en el Capítulo 6 se presenta la implementación del método de fronteras inmersas y resultados preliminares de la simulación de una Turbina de eje vertical.

Abstract

In this study, the dynamics of bubbles and drops is explored numerically for different flow conditions. The thesis is focused on the development of efficient numerical tools to analyze the flow generated by the motion of bubbles and drops in viscous fluids and by the heat and mass transfer mechanisms. The numerical implementation is based on the immersed boundary methods, specially, the front-tracking method to represent the interface between two fluids and calculate the material properties of each fluid into the domain. With this strategy, the solution of only one set of the conservation equations is required. In the first chapter, the mathematical formulation of the immersed boundary methods, the coupling with the Navier-Stokes equations and the strategy for the numerical integration are presented. In Chapter 2, the results of the numerical simulations of the flow generated by the ascent of a single bubble are reported and compared with experiments in a Hele-Shaw cell. The results showed that even when the two-dimensional model captures qualitatively the main features of the flow generated by a bubble rising in a Hele-Shaw cell, significant quantitative differences exist. The numerical code was extended to three dimensions and simulations for different flow conditions are presented in Chapter 3. In the first part, simulations at low Reynolds numbers are shown; in the second part, simulations of air bubbles in water are reported. In the cases analyzed, the density ratio is about 10^3 and the Reynolds numbers are in the range of 10^2-10^3. Also, the comparison with experimental data reported in the literature is shown. In the final part of the chapter, simulations of the flow generated by multiple air bubbles ascending in water are presented to test the robustness of the numerical implementation for solving more complex flows. In Chapter 4, the results of the simulations of non-isothermal bubbly flows in a channel are shown, paying attention on the effect of the presence of the bubbles on the heat transfer. In Chapter 5, the development and implementation of an evaporation model for falling drops are described. The model is validated by an analytical solution of the conservation equations for the evaporation phenomenon in a container partially filled with liquid. In the second part of the chapter, different simulations of the evaporation of a single and multiple droplets are presented. Finally, in Chapter 6, the implementation of the immersed boundary method and preliminary results of the simulation of the motion of a Vertical Axis Wind Turbine (VAWT) is presented to demonstrate the versatility of the code to solve problems of fluid-solid interactions with entirely different physical conditions than those described in previous chapters.

Introduction

Multi-fluid systems are of fundamental importance in many natural processes and in a host of industrial activities such as combustion, chemical reaction, petroleum refining and boiling. One of the simplest, yet most important of multi-fluid systems is the rising of bubbles in a viscous liquid due to buoyancy which has been studied extesively. However, even for the flow generated for a single bubble a comprehensive knowledge of the flow behavior and mechanism of such multi-fluid systems in full flow regimes is still lacking, although a number of experimental, theoretical analysis and numerical studies have addressed this problem. The first recorded observation of the rise of bubbles is to be found in the writings of Leonardo da Vinci. About five centuries ago, Da Vinci summarized his observations on the motion of air bubbles in a liquid in the following manner:

"The air that submerged itself with the water which percussed upon the other water, returns to the air, penetrating the water in sinuous movement, changing its substance into a great number of forms. And this happens because "the light thing cannot remain under the heavy"; rather it is continuously pressed by the part of the liquid which rests upon it; and because the water that stands there perpendicular is more powerful than the other in its decent, this water is always driven away by the part of the water that form its coverings, and so moves more continually sideways where it is less heavy and in consequence offers less resistance, according to the 5th [proposition] of the 2nd [book]; and because this "has to make its movement by the shortest way", it never spreads itself out from its path except the extent which it avoids the water which covers it above."

Leonardo da Vinci's words are translated in the picture presented in Figure 1 contained in the Codex Leicester and dates from approximately 1510. In modern times, many experimental works have reported several results about the behavior of a single rising bubble, Bhaga & Weber (1981), Sanada et al. (2007), de Vries (2001) and Mingming & Morteza (2002) are some examples. A comprehensive compilation of experimental results is available in the book Clift et al. (1978) where bubble shapes and terminal velocities of the bubbles for different flow conditions have been reported in the experimental works. It is now well known and documented that bubbles rise in axi-asymmetric trajectories, straight, spiral or zigzag. However, the mechanism of these motions of bubbles is not yet fully understood and this remains as an open question Mougin & Magnaudet (2002). For low Reynolds number the bubbles follow a straight path with a stable and axi-symmetric wake. When the Reynolds number is increased the wake of the bubble becomes unstable

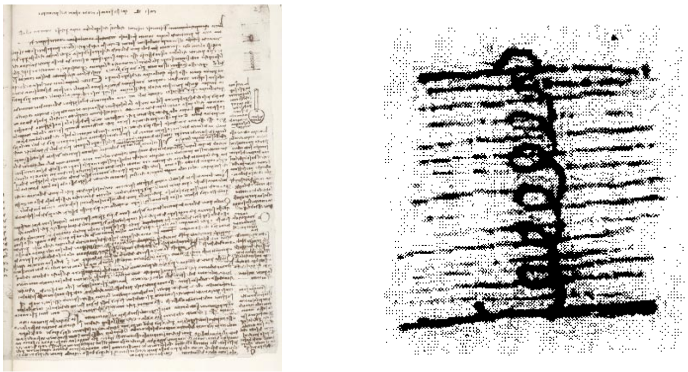

Figure 1: Leonardo's manuscript known as Codex Leicester. The small sketch in the right-hand side shows the spiraling motion of a rising bubble.

and the bubbles start to rise in a zigzag path or turn into a spiral trajectory. For the case of multiple bubbles, the dynamics is almost unexplored. Even when many experimental and theoretical studies have been reported in the literature that are focused in bubbly flows, there are many aspects in the dynamics and interactions of multiple bubbles that are still not understood. See for instance Sanada et al. (2005), Pfleger et al. (1999), Lu & Tryggvason (2008) and Drew & Passman (1999).

In real conditions it is very common that the multiphase flows are involved with other phenomena as heat and mass transfer and it is important to understand how the dynamics is affected due to the presence of such mechanisms and vice versa. In the case of the heat transfer in bubbly flows, it is well known that the presence of a disperse phase increases the heat transfer into the flow, but additional detailed studies for general flow conditions are necessary to understand the effect of the bubbles in the flow in order to take advantage of an specific system condition for a particular application. For the case of the mass transfer, evaporation and condensation processes appear in many cases into the flows with drops and bubbles. Although these mechanisms have been explored from the experimental point of view and there exist some analytical models, a detailed theoretical description is still lacking.

Considering the difficulties in experimental and theoretical investigations, numerical simulations provide an effective alternative approach to attain a better insight into the bubbles rising behavior, the development of bubble shape evolution and the heat and mass transfer in bubbly flows. In recent years, significant progress has been made in understanding and modeling bubbles rising in a column of fluid by advanced numerical simulations, particularly, using the immersed boundary methods (Hua & Lou (2007), Ohta et al. (2005), Chen et al. (1999), Bunner & Tryggvason (2002*a*), Lu & Tryggvason (2006)). In contrast with the average models (e.g. two-fluids models), the immersed boundary methods provide detailed information about the interface of the fluids; in these methods, the conservation equations are solved without any modeling assumptions.

The most popular methods based on this formulation are the volume-of-fluid, level-set, marker-particle, shock-capturing and front-tracking, to name a few. The numerical simulations of bubbles using the volume-of-fluid method have been widely used to try to understand the behavior of bubbles at different flow conditions, see for instance Scardovelli & Zaleski (1999). However, many problems are presented when this method is implemented, the most critical one being that artificial coalescence or rupture of bubbles can occur as discussed by van Sint Annaland et al. (2005). Another approach used to simulate multiphase flows is the level-set method (see Sussman et al. (1994) for details). The implementation of this method is very simple in two and three dimensions but its accuracy is limited because in most of the implementations disperse phases lose mass during the simulation and artificial coalescence and break up of the bubbles also occur. The front-tracking method is yet another alternative to compute multi-fluid systems as the rising of bubbles as described by Tryggvason et al. (2001), Hua & Lou (2007), Gunsing (2004). This method is extremely accurate because the interface is tracked explicitly using marker points connected to each other. Then, artificial coalescence does not occur due to the fact that a separate mesh is used to track the interface, but this method is difficult to implement since the interface of the fluids requires a remeshing algorithm each time step.

In the present project, a numerical study of the rising of bubbles in a column of fluid is presented, also heat and mass transfer mechanisms were implemented into the numerical simulations in order to explore more complex bubbly flows. The implementation is based on the solution of the Navier-Stokes equations using the standard finite volume method coupled with a front-tracking technique. The dynamics of bubbles was studied in two dimensions and the results are presented in Chapter 2. Also here, the simulations are compared with experiments that were carried out in a Hele-Shaw cell. The finite volume/front-tracking method was generalized for three dimensional flows and in Chapter 3, the dynamics of bubbles are presented in three parts; the first one is devoted to the analysis of the motion of bubbles at low Reynolds number, and a detailed study of the rising of bubbles at this flow conditions. The shape of the bubbles, terminal velocities and external flows are calculated. In the second part, the bubbles rising at high Reynolds are studied, the features of the oscillatory motion of the bubble and the unstable wake are explored. Finally in the third part, numerical simulations of multiple bubbles are presented and discussed in order to show the capabilities of the numerical code developed during this project. In chapter 4, the energy equation was solved in addition to the mass and momentum conservation equations in order to explore the heat transfer in bubbly flows in laminar and turbulent channels and interesting results are reported when the channel is inclined at different angles. In Chapter 5, an evaporation model of drops is described and implemented with the finite volume/front-tracking code; the complete implementation was validated with an analytical solution and it was used to explore the evaporation of drops falling by gravity. It is important to note that the main objective of this project was to have a robust numerical tool to explore in general the behavior of two-phase flows with disperse phases in realistic conditions using direct numerical simulations. Finally, in Chapter 6, the implementation of the immersed boundary method to simulate the flow around a Vertical Axis Wind Turbine is presented, the main objective of such numerical implementation was to demonstrate that the model and code developed in this thesis can be easily adapted to very different physical phenomena.

CHAPTER 1

Mathematical and numerical models

1.1 Mathematical Model

There are several ways to simulate multiphase flows; some classical examples are averaged models, boundary integral and Lattice Boltzmann methods. Other alternatives include immersed boundary methods for fluid interfaces. Commonly the immersed boundary methods are applied to simulate systems in which elastic structures interact with fluid flows Peskin (1977). However it is possible to extend this theory to the cases where fluid interfaces exist. The immersed boundary methods for multiphase flows have been widely applied in many different systems and various techniques based on that formulation such as volume of fluid, level set and the front tracking are available.

The mark-and-cell method can be conceived as the oldest version of the immersed boundary methods in which marker particles are used to identify each phase. Specifically, this method was used at Los Alamos National Laboratory in the early 1960s and allowed the first successful simulation of the finite Reynolds number motion of free surfaces and fluid interfaces. On the other hand, in the volume of fluid method, a marker function is used to find the interface between the two fluids, see Scardovelli & Zaleski (1999). This function is advected using the velocity field found when the momentum equations are solved in the domain. The level set is a widely used method, where a marker function is used to identify the different fluids in the domain and no assumption is made on the connectivity of the interface. This method allows an accurate computation of two phase flows including topological changes in the interface, like break up or coalescence of bubbles (Sussman et al. (1994)). However, in flow fields with appreciable vorticity or in cases where the interface is significantly deformed, level set methods suffer from loss of mass (volume) and hence loss of accuracy (van Sint Annaland et al. (2005)). The front tracking method avoids solving an equation for a marker function, but the interface between the fluids must be tagged using an unstructured mesh with connected marker points that are advected with the flow and then the surface tension and the material properties are computed from the new location of the interface. For a detailed discussion on this point, see Prosperetti & Tryggvason (2007).

In the present study, a fully three dimensional front tracking model that can be efficiently used to perform numerous computational experiments was implemented. The front tracking method was chosen because of its excellent capability to calculate the surface tension force, which significantly affects the bubble shape and dynamics. Other methods, like the classical volume of fluid, level set and mark-and-cell models, do not allow for such an accurate and detailed representation of the surface tension force and the mass of the bubble is not conserved during the simulations. Even in the front-tracking method the volume of the bubble is not intrinsically conserved exactly, the volume slowly changes in time. This is caused by the strategy used to move the interface, the applied filters and the remeshing of the interface mesh, but the loss of mass is less than that obtained with the other methods. The markers that span the surface elements are moved with their local velocities; and these local marker velocities are interpolated from the velocity field on the Cartesian grid. These interpolated velocities introduce minor small-scale anisotropy (Gunsing (2004)), but, using a finer computational grid this problem can effectively be suppressed.

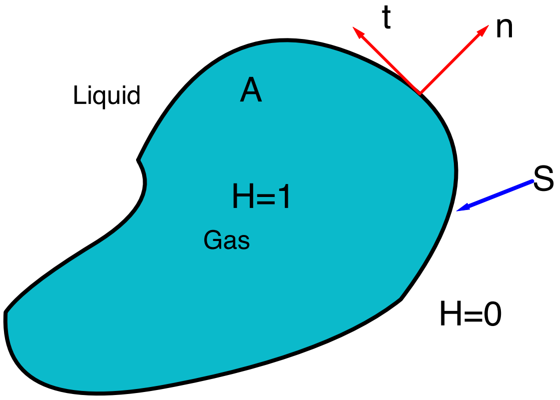

Figure 1.1: One fluid approach illustration in two dimensions.

In the immersed boundary methods it is possible to solve a single set of conservation equations using the “one fluid approach”. When a multiphase system is being analyzed, it is necessary to take into account the differences between the material properties of the fluids and the forces concentrated in the interface as the surface tension force. These forces can be represented as delta functions in the interface, and a Heaviside function is used in order to identify the different fluids in the domain [1] as illustrated in Figure 1.1 (Prosperetti & Tryggvason (2007)).

---

[1] The various fluids can be identified by a step (Heaviside) function H, which is 1 where one particular fluid is and 0 elsewhere Tryggvason et al. (2001).

Considering that the two fluids are incompressible, the mass conservation is given in terms of the velocity $\mathbf{u}$, by:

$$\nabla\cdot \mathbf{u} = 0. \tag{1.1}$$

The momentum conservation equation must take into account the different fluid properties of the two fluids and also the jump at the interface represented by the term of the surface tension.

$$\begin{aligned} \frac{\partial \rho \mathbf{u}}{\partial t} + \nabla\cdot \rho \mathbf{u}\mathbf{u} &= -\nabla p + \nabla\cdot \mu(\nabla \mathbf{u} + \nabla^T \mathbf{u}) \\ &\quad + \int \sigma \kappa_f \mathbf{n}_f \delta^\beta(\mathbf{x} - \mathbf{x}_f) dS_f + (\rho - \rho_l)\mathbf{g}. \end{aligned} \tag{1.2}$$

The pressure is denoted by p, μ is the viscosity, $\mathbf{g}$ is the gravity vector, ρ_l is the density of the continuous phase, σ is surface tension and κ_f is the curvature. The presence of the interface is incorporated by the term $\delta^\beta(\mathbf{x} - \mathbf{x}_f) = \delta(x - x_f)\delta(y - y_f)\delta(z - z_f)$, where $\mathbf{x}$ is the point at which the equations are evaluated and $\mathbf{x}_f$ is a point in the interface. Formally, the integral is over the entire front, thereby adding the delta functions together to create a force that is concentrated at the interface, but is smooth along the interface. It is important to note that this equation is valid for the whole field even when the density ρ and viscosity μ fields change discontinuously.

1.2 Front-tracking method in three-dimensions

1.2.1 Structure of the front

The front is constructed by points that are connected by triangular elements in order to form a non-unstructured grid. For each point, the only information stored is its coordinates. The triangular elements are characterized by its centroid coordinates and special arrays assigned to each element are used to store information on the points that connect the element itself, as well as the local structure of the front, including its neighboring elements. The elements also contain information about the physical properties associated with the interface, such as the surface tension, change in the value of the marker function across the front, and any other quantities that are needed for a particular simulation. Figure 1.2 shows the key variables that are stored for each of the three-dimensional front elements. The front motion is dictated by the velocity field on the regular grid properly interpolated at each front point. The surface tension force is calculated in the front points and interpolated to the regular grid to compute the conservation equations.

1.2.2 Remeshing the front

In general, an interface will stretch and deform as a result of the fluid motion. When marker points are used to track the interface, stretching results in an increased separation

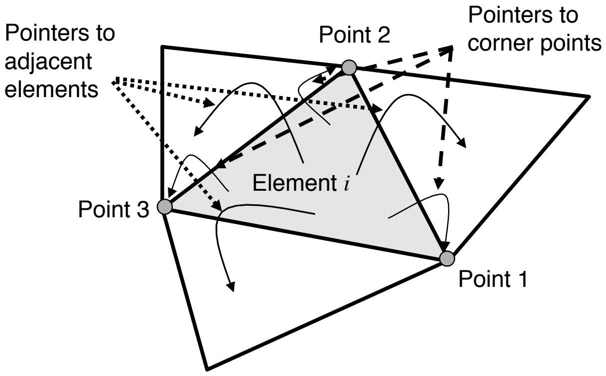

Figure 1.2: The structure of a three-dimensional front triangular element (Reprinted from Tryggvason et al. (2001)).

of the points and eventually it becomes necessary to insert new points to resolve the interface adequately. When the interface is compressed, the points are crowded together and although it is, in principle, not necessary to remove points, in practice it is generally better to do this, in order to avoid the formation of elements much smaller than the grid size.

When the interface is a surface embedded in a three- dimensional flow, this aspect literally takes on a whole new dimension. The regridding procedure consists of three basic steps: (a) node addition (for elements that become too large); (b) node deletion (when elements become small); and (c) reconnection or restructuring (to eliminate bad “aspect ratios”, i.e., elements that have a small area but a large perimeter). Figure 1.3 depicts these three basic regridding operations schematically.

1.2.3 Interpolating the front properties from the non-structured grid to the Cartesian grid

Since the Navier-Stokes equations are solved in the fixed grid and the interface forces like the surface tension are solved in the front, it is necessary to convert a quantity that exists in the front to a grid value. Since the front represents a delta function, the transfer corresponds to the construction of an approximation to this delta function on the fixed grid. The discrete expression required for the conversion of a quantity from the front to the fixed grid is given by:

$$\phi_{ijk} = \sum \phi_l \omega_{ijk}^l \frac{\Delta s_l}{h^3} \tag{1.3}$$

where ϕ_{ijk} is an approximation to the grid value, ϕ_l is an approximation to the front value, Δs_l is the area of the element l and ω_{ijk}^l is the discrete form of the Dirac delta function

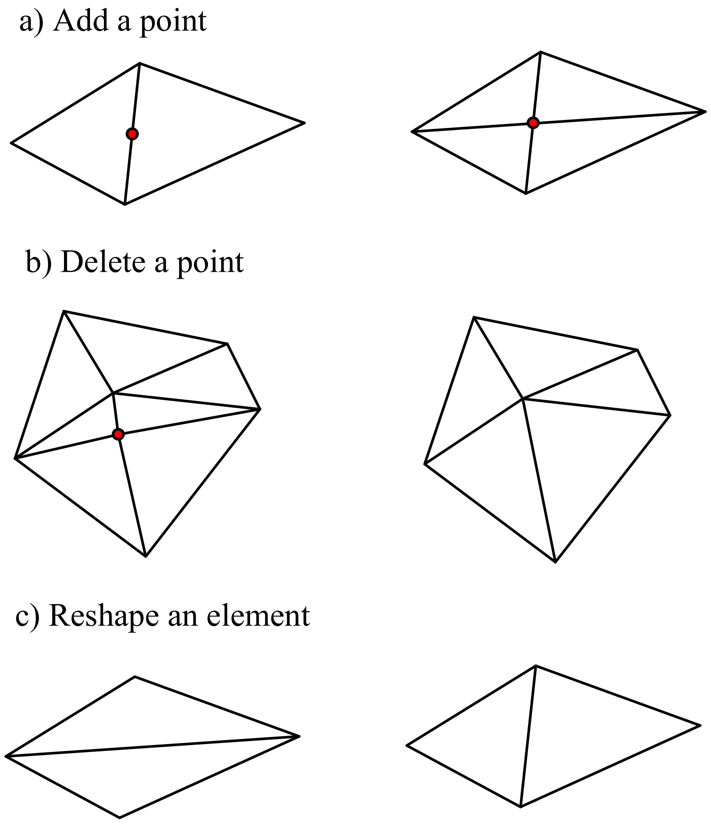

Figure 1.3: The basic operations in dynamic restructuring of the three- dimensional interface grid.

and is the weight of grid point ijk with respect to element l. The weighting functions can be expressed as a product of one-dimensional functions. In three dimensions the weight on the grid point (i, j, k) of the smoothing from $X_p = (x_p, y_p, z_p)$ is given by:

$$\omega^l_{ijk} = d(x_p - ih)d(y_p - jh)d(z_p - kh) \tag{1.4}$$

In the present work, the following form of the weighting function developed by Peskin (1977) is used in order to construct $d(r)$:

$$d(r) = \begin{cases} (1/4h)(1 + cos(\pi r/2h)), & |r| < 2h \\ 0, & |r| \geq 2h. \end{cases} \tag{1.5}$$

It is important to note that using the weighting function given by Peskin, sixty four points of the finite volume grid are affected for the quantity calculated on the front and the transition of the properties between the front and the regular grid is smooth compared with other weighting functions reported in the literature.

1.2.4 Computing the properties of the fluids

When the front-tracking method is used, the boundary between the different fluids is moved according to the previously stated steps, but the fluid properties such as the density and viscosity, are not advected directly, and it is therefore necessary to reset these quantities at every time step. In order to make a consistent calculation, we first define a indicator field $I(\mathbf{x})$ that is a constant within a fluid, but different for each fluid and then use it to set the physical properties. To construct the indicator field we use the fact that the front marks the jump in the density and that this jump is translated into a steep gradient on the fixed grid. The gradient of the indicator field in the one fluid formulation can be expressed as:

$$\nabla I = \int_S \Delta I \mathbf{n}_f \delta(\mathbf{x} - \mathbf{x}_f) dS_f, \tag{1.6}$$

and the integration is made over the surface of the front S. In a discrete form the indicator field can be written as:

$$\nabla I_{ijk} = \sum_l \Delta I \omega_{ijk}^l \mathbf{n}_l \Delta s_l, \tag{1.7}$$

where $\mathbf{n}_l$ is the unit normal vector to each front element. Once the grid gradient of the indicator field has been constructed, the field can be recovered. Taking the numerical divergence of the grid indicator field gradient results in:

$$\nabla^2 I = \nabla \cdot \nabla I_{ijk}. \tag{1.8}$$

The left-hand side is approximated by standard central differences, and solving the resulting Poisson equation with the appropriate boundary conditions yields the indicator field everywhere.

The field distribution $\phi(\mathbf{x}, t)$ of the fluid properties can be calculated with the indicator field using a linear interpolation,

$$\phi(\mathbf{x}, t) = \phi_b I(\mathbf{x}, t) - \phi_l(1 - I(\mathbf{x}, t)), \tag{1.9}$$

where the subscripts b and f represent properties of the bubble and the surrounding fluid, respectively.

1.2.5 Advecting the front

The front advancement must be found by interpolating from the fixed grid field velocity, using the same weighting function that was used to transfer the properties from the front to the fixed grid. Once the velocity of each front point is known, its new position can be found by a simple first order explicit Euler integration:

$$\mathbf{x}_f^{n+1} = \mathbf{x}_f^n + \mathbf{v}_f^n \Delta t, \tag{1.10}$$

where $\mathbf{x}_f$ is the front position, $\mathbf{v}_f$ is the front velocity, and Δt is the time step. It is important to comment that the front velocity is computed using the Peskin weighting function, i.e., the velocity of the sixteen closer points of the fixed grid to one point of the front are used to find its velocity.

1.2.6 Surface tension force

One of the most important elements in the immersed boundary methods implementation is the surface tension force calculation. This property depends of the curvature of the interface, and since the interface is deformed during the simulation, the curvature must be calculated in every time step. For three-dimensional problems, we use the fact that the mean curvature κ_f of a surface can be written as:

$$\kappa_f \mathbf{n}_f = (\mathbf{n}_f \times \nabla) \times \mathbf{n}_f. \tag{1.11}$$

Recalling that σ is the surface tension coefficient, the force on a surface element is therefore:

$$\delta F_\sigma = \sigma \int_{\Delta S} \kappa_f \mathbf{n}_f dS_f = \sigma \int_{\Delta S} (\mathbf{n}_f \times \nabla) \times \mathbf{n}_f dS_f \tag{1.12}$$

The Stokes theorem can be used to convert the area integral into a line integral along the edges of the element as suggested by Tryggvason et al. (2001). Here, $\mathbf{t}$ is a vector tangent to the edge of the element, and $\mathbf{n}$ is a normal vector to the surface. The cross product is a vector that lies on the surface and is normal to the edge of the element. The product of the surface-tension and this vector gives the “pull” on the edge and the net pull is obtained by integrating around the perimeter of the element.

$$\delta F_\sigma = \sigma \oint_S \mathbf{t} \times \mathbf{n} dS_f \tag{1.13}$$

1.2.7 Volume conservation of the front

As discussed previosuly, the flow inside the gas bubble is assumed to be incompressible. A consequence of this assumption is that the volume of the bubble should remain constant throughout the simulations; however, the mesh needs to be adapted at every time step and the motion of the interface can violate the incompressibility condition. Then it is necessary to enforce in a geometric manner that the volume of the gas bubble remains constant in the total time of the computational simulation. In Figure 1.4,the volume of the bubble as a function of time is plotted. The red line is the simulation without any correction of the volume of the bubble; it is clear that even when is a short simulation at least 2% of the volume is lost; On the other hand when the geometric correction is used the volume of the bubble is conserved (as indicated by the black line in Figure 1.4).

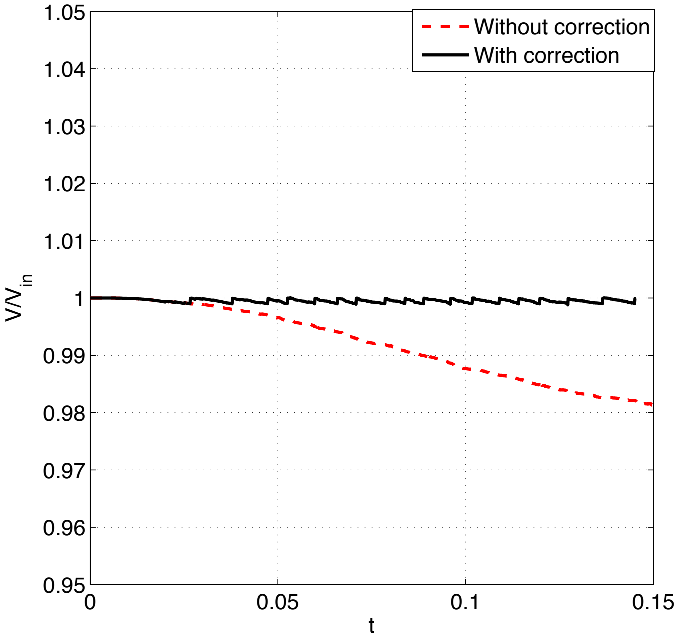

Figure 1.4: Volume conservation with and without geometric correction.

1.3 Numerical integration of the conservation equations

One of the main objectives of the present investigation was to simulate the motion of air bubbles in water. This requires the consideration of large density ratios ($\rho_l/\rho_b \sim 10^3$) and high Reynolds numbers. Before embarking in constructing the code, for integrating the conservation equations to simulate the motion of gas bubbles immersed in a liquid, we made a through literature review to find the different strategies reported by the authors to avoid the numerical problems that appear under certain flow conditions. The most recent work that was found in the literature was Stene (2010). In his thesis, this author presents simulations of a bubble using front-tracking method highlighting the cases where the density ratio is very large. Other authors have made simulations at high Reynolds numbers but not at high density ratios. For example van Sint Annaland et al. (2006) reported simulations of water-air systems in which the density of the air is artificially considered to be 10 kg/m^3 to be able to properly perform the integration. In some other works the authors try to justify the use of small density ratios by asserting that the results are not sensitive to this property when density ratio are larger than approximately 50.

The following Navier-Stokes equations:

$$\begin{aligned}\rho\left(\frac{\partial \mathbf{u}}{\partial t}+\nabla\cdot\mathbf{u}\mathbf{u}\right) &= -\nabla p+\nabla\cdot\mu(\nabla\mathbf{u}+\nabla^T\mathbf{u})\\ &\quad +\textstyle\int \sigma\kappa_f\mathbf{n}_f\delta^\beta(\mathbf{x}-\mathbf{x}_f)dS_f+(\rho-\rho_l)\mathbf{g}\end{aligned} \tag{1.14}$$

are solved in their non-conservative form using a standard finite volume discretization. Typically the error introduced when the density on the left hand side of the equation is evaluated explicitly is below 0.5% using an appropiate time step Gunsing (2004). The conservation equations can be solved with the projection method using a conventional first-order scheme (Tryggvason et al. (2011)). The temporal integration is splitted in two parts. The first part is a prediction step where the effect of the pressure is ignored,

$$\frac{\mathbf{u}^*-\mathbf{u}^n}{\Delta t}=-\frac{1}{\rho^n}(\nabla\cdot\rho^n\mathbf{u}^n\mathbf{u}^n+\nabla\cdot\mu^n(\nabla\mathbf{u}^n+\nabla^T\mathbf{u}^n)+\mathbf{F}_\sigma+\mathbf{F}_{buoyancy}). \tag{1.15}$$

The second part is a correction step in which the pressure term is included:

$$\frac{\mathbf{u}^{n+1}-\mathbf{u}^*}{\Delta t}=-\frac{1}{\rho^{n+1}}\nabla p. \tag{1.16}$$

The pressure is calculated in such a way that the velocity at the new time step satisfies the mass conservation equation:

$$\nabla\cdot\mathbf{u}^{n+1}=0. \tag{1.17}$$

Replacing Eq.(1.17) in Eq.(1.16) the pressure can be calculated as follows:

$$\nabla\frac{1}{\rho^{n+1}}\cdot\nabla p=\frac{1}{\Delta t}\nabla\cdot\mathbf{u}^*, \tag{1.18}$$

For solving the resulting pressure equation a special treatment is required since the density is not a constant in the interface. In early formulations of the front-tracking method, a simple successive over relaxation (SOR) method was used, but the results were not satisfactory in the cases which the material properties of the fluids are very different. Specially when the density ratio between the two fluids is large. Under these conditions, the SOR method takes a large computational time to solve the pressure Poisson equation, since the resulting linear system of equations is ill conditioned, this in turn occurs because some of the coefficients in the matrix are divided by the density of the bubble and others by the density of the continuous phase. However, with a high order discretization in the advection terms and a robust preconditioned solver the system can converge.

In this work, we used a Krylob preconditioned conjugate gradient to solve the pressure equation in a GPU, in order to solve large Reynolds numbers and large density ratios. The details about computational implementation will be presented in the next section. To compute the momentum advection, the pressure term, and the viscous forces, any number of standard discretization schemes can be used. Note however, that a robust discretization for the advection terms can be the key to solve correctly flows at high Reynolds numbers. In the present study, the calculation of the convection terms was improved significantly by using a third-order upwind-biased polynomial called QUICK(quadratic upstream interpolation for convective kinematics). In Figure 1.5, the diagram of how the interpolation must be done in the QUICK scheme for a regular finite volume grid is presented. As in the upwind first order scheme, the polynomial interpolation depends on the direction of the flow in the corresponding face of the control volume; using the notation of Figure 1.5 an example of a polynomial to calculate the variable ϕ in one of the faces can be constructed as follows:

$$\phi_w = \begin{cases} 1/8(3\phi_P + 6\phi_{W,j,k} + \phi_{WW}) & c_w > 0 \\ 1/8(3\phi_W + 6\phi_P + \phi_E) & c_w < 0 \end{cases} \tag{1.19}$$

In our discretization the Navier-Stokes equations are solved in a staggered grid, the QUICK scheme must be modified to calculate the three dimensional components of the velocity in the faces of the control volumes. For example, the interpolation required to calculate the component u of the velocity using the QUICK scheme is given by:

$$u_{i,j,k} = \begin{cases} 1/8(3u_{i+1/2,j,k} + 6u_{i-1/2,j,k} + u_{i-3/2,j,k}) & c_w > 0 \\ 1/8(3u_{i-1/2,j,k} + 6u_{i+1/2,j,k} + u_{i+3/2,j,k}) & c_w < 0, \end{cases} \tag{1.20}$$

where:

$$c_w = \frac{1}{2}(u_{i-1/2,j,k} + u_{i+1/2,j,k}). \tag{1.21}$$

1.4 Computational details

The first version of the code was developed in FORTRAN and works sequentially. In order to accelerate the numerical computations the code was adapted to use the GPU architecture. Most of the computational time is consumed in the solution of the pressure and indicator Poisson equations. Then, an efficient and parallel library to solve large sparse linear systems was used. There are many libraries to solve iteratively sparse linear

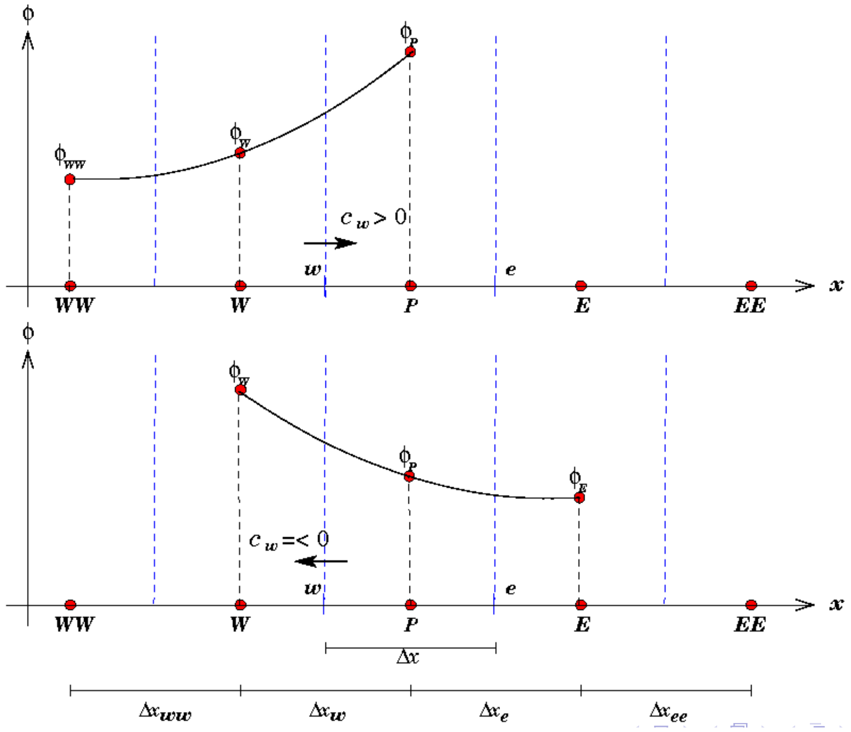

Figure 1.5: Interpolation for the QUICK scheme in a finite volume regular 1D grid.

systems, so we decided to take advantage of the GPU architecture to accelerate the solution of the linear systems obtained with our discretization. In many cases it is possible to get considerably speed up when the linear systems are solved in the GPU with respect to the CPU implementations. Currently, there are two tools available for this purpose: CUSPARSE a part of NVIDIA's CUDA, or the external library, CUSP. The CUSP library was developed by several NVIDIA employees with minimal software dependencies and released freely under an open-source license. We chose to use the CUSP library for several reasons: it is in continuous development and separate from the main CUDA distribution, allowing for faster addition of new features (such as new pre-conditioners, solvers, etc.); and, all objects/methods from the library are usable on both CPU and GPU.

While the use of a more robust solver offers more stability in the numerical solutions even in the cases of high density ratios, the use of the CUSP library implemented in the GPU gives a considerable speed up time in our simulations, since the linear systems of equations that results from the discretization of the pressure and indicator equations are solved in parallel in the GPU. In order to use an open source language to developed the new front-tracking code we decided to translate it from FORTRAN to CUDA C efficiently. As it is well known, one of the important limitation in the GPU implementation is the amount of memory available; then, the first improvement in this sense was to use a diagonal sparse matrix format to store the coefficient matrices of the linear systems. To solve the indicator and pressure equations we decided to use a conjugate gradient method with Jacobi pre-conditioner. Using such strategy of the solution we were able to solve bubbly-flows with a density ratio up to 2000 which is twice as large as that required for an air-water system. In Figure 1.6 , the comparison of the computational time required to solve the first time step of the front-tracking code with the two different implementations is shown. In both cases we use a projection method to solve the Navier-Stokes equations described in the previous section. It is demonstrated that the CUSP implementation is faster than the FORTRAN code, however, it is important to highlight that since the linear systems of the serial code are solved with the SOR method an important speed up of the CUSP code is obtained by using a more robust solver as it is the pre-conditioned conjugate gradient. Then a fairer comparison has to be done by using a robust solver in the FORTRAN like the MathKernel from intel. Avoiding such details, the speed up between the CPU and GPU implementations are notable, even if we use a basic GPU as GeForce GT 430 with 96 CUDA cores. Running the code in a better GPU as the NVIDIA GTX 660 with 986 CUDA cores the speed up increased and we were able to solve huge domains with over 15 millions of control volumes.

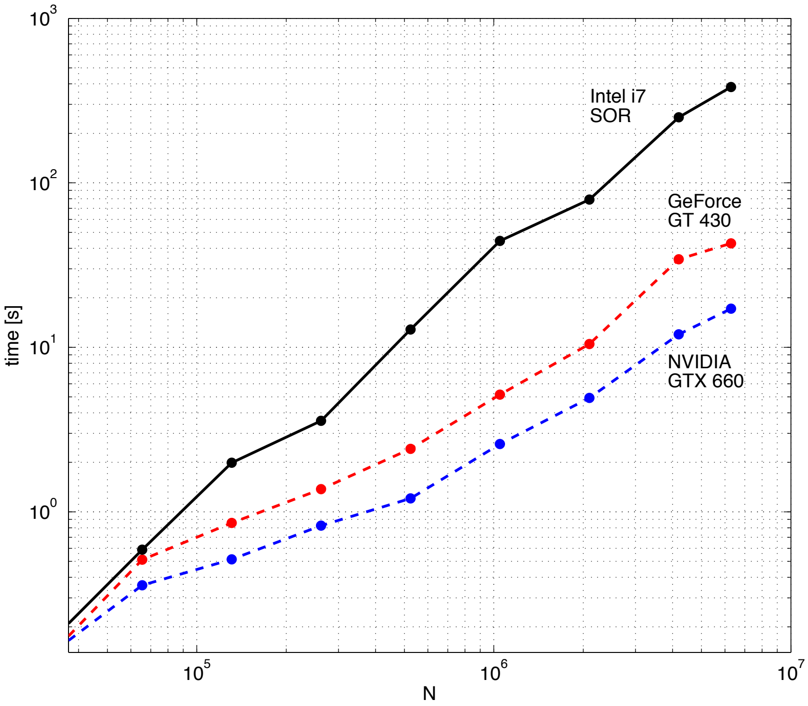

Figure 1.6: Calculation time for the CPU-SOR and GPU-CG codes, N is the number of control volumes. The black curve represents the FORTRAN implementation and the blue and red dashed lines the CUSP implementation computed in two different GPU's.

Chapter 2

Dynamics of two dimensional bubbles[1]

2.1 Background

The study of the dynamics of bubbles in Hele-Shaw cells have been proposed as an effort to simplify the study of ascending bubbles by restricting the motion in one horizontal direction. In this way, the available degrees of freedom are reduced since the description can be made in terms of the position and deformation in two spatial coordinates. Under these conditions, it is recognized that low velocity flows (small Reynolds numbers) can be described with linear equations of the Darcy type. For large Reynolds numbers, the inertial effects are important and the full Navier-Stokes equations are required to describe the motion. Experiments were conducted for bubble diameters larger than the cell gap by Maxworthy (1986), Kelley & Wu (2005) and recently by Roig et al. (2012). Under these conditions, the squashed bubble is more like a cylinder than a sphere. The qualitative properties of the dynamics of the bubbles and the flow around them can be described in terms of nondimensional parameters like the Archimedes (Ar) and Eötvos (Eo) numbers (for the definition of these parameters used in the present work see Section 2.3). Observe however that the terminal Reynolds number is a result of the balance of the buoyancy and drag forces and is not externally fixed. Roig et al. performed experiments using air bubbles in water moving in a cell with a gap between the plates of 1 mm and found a linear relationship between the Archimedes and terminal Reynolds numbers; namely $Re = 0.5Ar$. For later reference, it is convenient to remark that the characteristic length of the bubble used in the definition of the Archimedes and Reynolds numbers is the apparent diameter of the bubble as seen from the perpendicular direction of the plates. Kelley and Wu used a tilted Hele-Shaw cell with a gap of 1.6 mm and determined that the wake formed in the surrounding fluid due to the motion of the bubbles was similar to that observed behind solid cylinders, despite the different boundary conditions at the interface. The onset of vortex shedding for large enough terminal Reynolds numbers was found to be described as a supercritical bifurcation Kelley & Wu (2005). Beyond this transition, the bubbles followed a zigzag path due to the non-symmetric pressure field at the surface generated by the vortex shedding. It is important to emphasize that the vortex distribution behind a bubble in a Hele-Shaw cell is completely different from the wake

---

[1] Preliminary results are presented in Piedra & Ramos (2012). A more complete description is given in Piedra, Ramos & Herrera (2015)

for an unconfined sphere or bubble formed by an elongated horseshoe vortex Horowitz & Williamson (2010).
In this investigation, bubbles rising at moderate and high Reynolds numbers are studied, the features of the oscillatory motion of the bubble and the wake are explored. The implementation is based on the solution of the Navier-Stokes equations coupled with a front tracking method described in the previous chapter. However, in this case, the pressure-velocity decoupling was accomplished with the SIMPLEC algorithm Versteeg & Malalasekera (1995) which was demonstrated to be superior to the projection method for problems with markedly different densities Hua & Lou (2007). Also, the diffusive and convective terms were discretized with a second-order centered scheme and the time integration was done with a first-order scheme, the details of the numerical implementation are reported in Piedra (2011). The results are presented using the Eötvos (ratio of buoyancy to surface tension) and Archimedes numbers (ratio of buoyancy to viscous forces). For formal definitions of these parameters, see subsection 2.3.1. Also, the results of the numerical simulations are compared with experiments in a Hele-Shaw cell. This is an interesting physical situation that approximates the motion of bubbles in two dimensions. In order to be able to compare the results of the simulation with experimental observations, a robust code has been developed capable to solve the conservation equations considering air bubbles in water where the ratio of densities is approximately 10^3 for a total duration of the simulation long enough to allow the bubble to move 420 diameters.

2.2 Experimental device

The experimental observations reported in section 2.3, were made using a Hele-Shaw cell which consisted of two parallel rectangular glass plates (50 cm × 25 cm × 0.2 cm), separated by 0.1, 0.2 or 0.25 cm thick spacers and sealed with an o-ring. The plates were fixed in a vertical position with an aluminum frame and clamps. Distilled water filled the gap between the two glass plates. A needle is used to inject the bubbles at the bottom of the cell. Figure 2.1 shows the experimental arrangement. In order to accurately fix the volume of the bubbles and systematize the injection process, we used the methodology proposed by Tomiyama et al. (2002). The air bubble is fed into the needle through a thin hose whose other end is fitted to a **Y** type hose connector. The hose is filled with water but an air bubble with a known volume generated with a syringe pump is introduced in the hose via one leg of the connector (see detail in Figure 2.1). A static pressure nearly equal to that occurring at the bottom of the cell is put at the other end of the connector with a hydrostatic pressure head system. A small increase of the hydrostatic pressure gently moves the bubble through the hose to the needle and into the cell. The syringe pump used to inject a controlled amount of volume into the cell can introduce 0-100μl with a precision of 0.1μl. This allows us to inject bubbles for the three different cell gaps from 2 to 7.3 mm of apparent diameter.

The trajectory and shape of bubbles were recorded at 240 fps with a high-speed camera with resolution of 640 × 480 pixels and an image analysis algorithm is used to detect

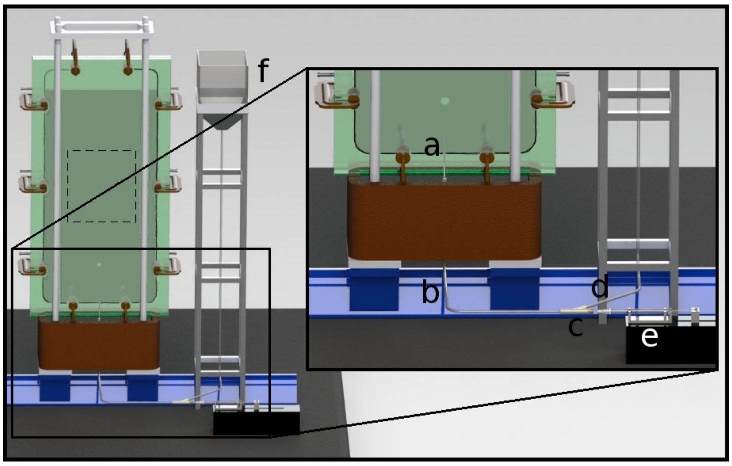

Figure 2.1: Hele-Shaw cell used to obtain the experimental results of Section 2.4. The amplified detail shows the arrangement to inject a bubble with controlled volume and negligible initial velocity. a) feeding needle, b) feeding hose, c) **Y** connector, d) pressure head hose, e) syringe pump, f) pressure head reservoir. The observation area is indicated by the broken line.

the pixels that correspond to the boundary of the bubble on the plane of the cell. The algorithm determines the time evolution of the bubble, its shape and locates the centroid of the bubble in all frames. Using this information the apparent diameter is found as $D = \sqrt{4A/\pi}$, where A is the projected area of the bubble on the plane of the cell. The velocity of the bubble as a function of time can be computed using the trajectory of its centroid. All observations were made at least 14 cm above the feeding needle where the details of the bubble formation and departure are negligible. The observation window is indicated by the broken line in figure 2.1. The goal in the image processing was to find the interface to calculate the area and the centroid of the bubbles. For large bubbles that do not have elliptical shape, the interface was tracked using an internal function of Matlab, the images were converted from gray scale to black and white and compared with a base image in which no bubbles are present. For smaller bubbles, an ellipse fit function was used to find the interface, the resulting images after the processing for both cases are illustrated in Figure 2.2.

2.3 Results

In the first part of this section, we present an overview of the phenomenon by making a parametric study in the (Eo, Ar) space to establish the general properties of the single bubble dynamics. Then, we describe the motion of the centroid, geometry and flow patterns of individual bubbles and then, we compare the numerical results with the observation of bubble dynamics in a Hele-Shaw cell which is an approximation of a two dimensional bubble dynamics.

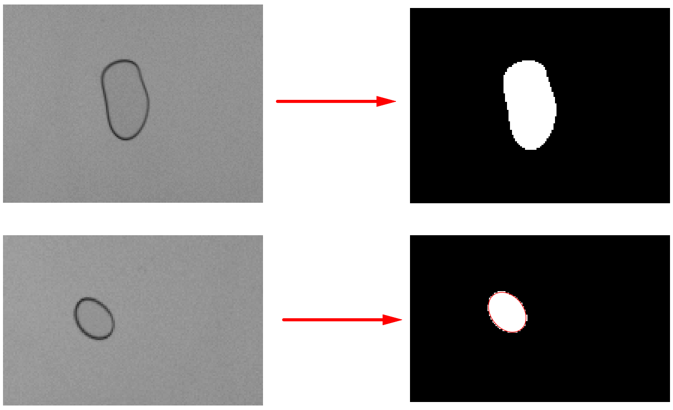

Figure 2.2: Images processed to find the geometrical features of the bubble. On the left side, the images taken from the high speed camera are presented. On the right side, the results after the image processing algorithm are shown.

2.3.1 General properties

It is convenient to make the description of the geometry and trajectories of the bubbles in terms of the Eötvos and Archimedes numbers which represent the ratio of buoyancy forces to surface tension and the ratio of buoyancy to viscous forces respectively and are defined by

$$Eo = \frac{D^2 g \Delta\rho}{\sigma} \qquad \text{and} \qquad Ar = \left(\frac{g D^3 \rho_l \Delta\rho}{\mu_l^2}\right)^{1/2}, \tag{2.1}$$

where $\Delta\rho = \rho_l - \rho_b$ and ρ_l and ρ_b are the density of the fluid and bubbles respectively. The viscosity of the continuous phase is μ_l and D is the initial diameter of the bubble. Observe that frequently, the Morton number defined by $Mo = Eo^3/Ar^4$, has been used in the literature to describe the features of the bubble motion. Note that the this parameter depends only on the physical properties of the bubbles and surrounding fluid.

A useful dimensionless parameter to characterize the flow is the Reynolds number, defined by

$$Re = \frac{\rho_l U_T D}{\mu_l}. \tag{2.2}$$

Note however that this Reynolds number depends on the terminal vertical velocity of the centroid of the bubbles U_T and cannot be prescribed *a priori* in the problem, but is the result of the interaction of buoyancy and drag forces.

The Re vs Eo chart that describes the geometry and dynamics of two dimensional bubbles constructed from our numerical simulations is shown in Figure 2.3. The examples analyzed are represented by small circles in the chart. Regarding the shape of the bubbles, the following regions, separated by continuous black lines, can be distinguished: a) Circular bubbles are found at the left bottom region of the (Eo, Re) map where surface tension dominates. b) Intermediate region where shear and surface tension effects have a similar influence leading to oblate ellipses and c) Region with relatively large Eötvos numbers where shear effects are large and bubbles develop flat bottom shapes. The aspect ratio (length of minor axis/length of major axis) has small variations as the bubble ascends, but its average value gets smaller as the Eötvos number grows. The boundary between the elliptical flat bubbles is diffuse since the evolution is gradual and it is difficult to determine the precise parameters when the lower part of the ellipse develops a flat region. Cases calculated with constant Archimedes numbers are joined by broken lines. As it can be observed, bubbles with equal Archimedes number reach a larger terminal Reynolds number for smaller Eötvos number. *i.e.* all red broken lines are monotonously decreasing. This effect is due to the modification of the bubble shapes since, as commented before, the aspect ratio of bubbles becomes smaller for larger Eötvos numbers. Regarding the motion of bubbles, it is found that cases under the black broken line follow straight ascending trajectories, while those above it ascend following zigzag trajectories due to vortex shedding. In the next subsection we present a more detailed discussion on this feature, here we only observe that the critical Reynolds number for circular bubbles is 44.2 approximately coinciding with the critical Reynolds number for vortex shedding by a fixed, rigid cylinder of 45 Williamson (1996). In contrast, for elliptical shapes, the critical Reynolds number is a decreasing function of the Eötvos number, i.e. the critical Reynolds number is dependent on the aspect ratio of the elliptical bubbles. This phenomenon was observed for rigid elliptical bodies Johnson et al. (2001). The case $Eo = 0.84$, $Ar = 392$ is described somewhat in detail in the next sections.

An interesting property of the dynamics of individual bubbles with fixed Morton number is displayed in Figure 2.4 where the terminal Reynolds number is plotted as a function of the Archimedes number for $Mo = 2.5 \times 10^{-11}$. As can be appreciated, the terminal Reynolds number is approximately equal to the Archimedes number in the range $2 \times 10^2 < Ar < 2 \times 10^3$. In the interval of validity, the approximation is better for the larger values of Archimedes numbers. In the specific example of this figure, $Re = Ar$. It should be noticed that this property is verified for both circular and elliptic bubbles shedding vortices, where the vertical velocity pulsates and we report the average, (see Section 2.3.2). The linear relation between the terminal Reynolds number and the Archimedes number was experimentally discovered by Roig et al. (2012) for air bubbles in a Hele-Shaw cell filled with water. In their observations, they found $Re = 0.5Ar$. The difference between the proportionality constant obtained with the two-dimensional model and the observations in the Hele-Shaw cell is further discussed in Section 2.4. The relation between the terminal Reynolds and the Archimedes numbers is important since the terminal Reynolds number is very informative with respect to the flow around the bubbles and cannot be set *a priori* in an experiment.

As commented before, the cases above the black broken line in Figure 2.3 ascend in zigzag with a characteristic frequency f. It is found that the non dimensional frequency (Strouhal number $St = fD/U_T$) of the ascending bubbles is a monotonic increasing function of

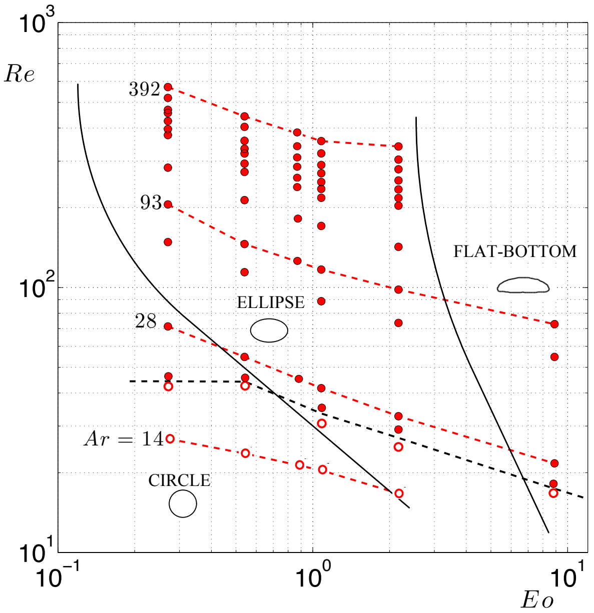

Figure 2.3: Map of qualitative behavior of the two dimensional bubble motion. The black broken line indicates the critical Reynolds number. Below this line, the bubbles follow straight trajectories (circles) and above it the bubbles ascend in zigzag (filled circles).

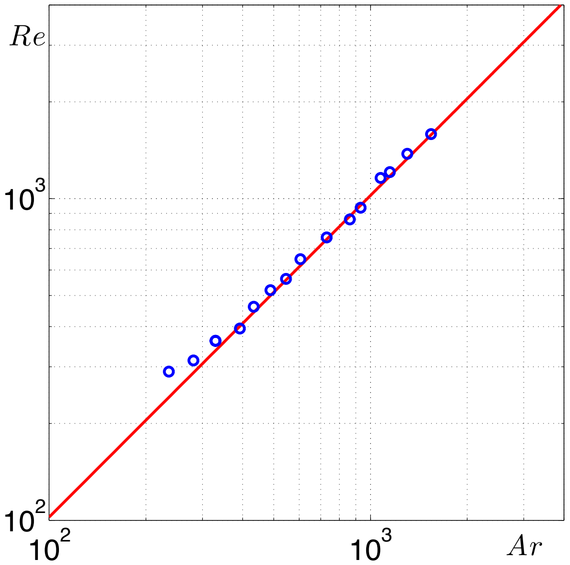

Figure 2.4: Terminal Reynolds number as a function of Archimedes number. The Morton number is 2.5×10^{-11}. The line represents Re= Ar.

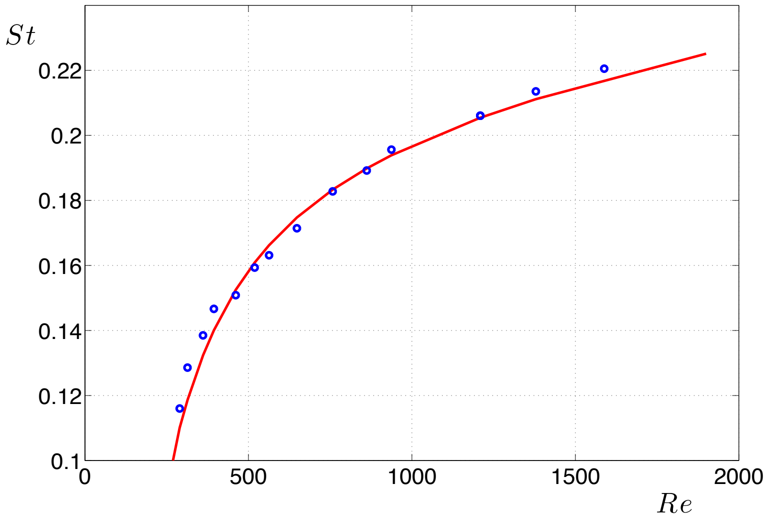

Figure 2.5: Strouhal number as a function of terminal Reynolds number (blue points) for $Mo = 2.5 \times 10^{-11}$. This case correspond to air bubbles in water. The line is St=A/Re+B+CRe with A= -31.1, B= 0.213, C= 1.5×10^{-5}.

the terminal Reynolds number, as it is demonstrated in Figure 2.5. The points plotted correspond to those presented in Figure 2.4. The data can be fitted with a function of the form St=A/Re+B+CRe which was proposed as a universal curve to describe the vortex shedding in the wake of rigid, fixed cylinders Williamson (1988). This curve also describes the Strouhal number of air bubbles ascending in a a Hele-Shaw cell Kelley & Wu (2005). Note however, that the Reynolds number ranges in the two cases are different. For air bubbles in water the range is $200 < Re < 2000$ while for fixed cylinders and experimental bubbles it is approximately $45 < Re < 180$. Also, the coefficients A,B and C in the expression are different. It would be tempting to compare the coefficients A, B and C in the two cases. We find that the first coefficient is an order of magnitude larger in the two dimensional bubble model, the second coefficient is 20% larger and the third is an order of magnitude smaller. The coefficients for cylinders are taken from Williamson (1988). Now, it should be emphasized that the comparison is not direct since there are three major differences in the two physical conditions. One is the boundary condition at the interface; while the no-slip condition for the rigid cylinders is imposed, for the bubbles, we use the slip condition. The second one is that the ratio of the density of the surrounding fluid to the density of the body is about 10^3 for the bubbles and essentially zero for the rigid obstacle since by definition, the cylinder remains motionless in spite of the forces acting on its surface. Finally, the bubbles deform due to the interaction with the surrounding fluid and the cylinder does not. These effects account for the differences in the Reynolds numbers where vortices are shed and consequently for the different coefficients obtained.

2.3.2 Trajectory of the centroid

Representative trajectories of the centroids of individual bubbles with $Eo = 0.84$, $Ar = 14, 28, 70$ and 392 are shown in Figure 2.6. In order to present the results in a non-dimensional form the variables were normalized using the diameter D as a characteristic length and $(D/g)^{0.5}$ as the characteristic time. The scaled variables are $x^* = x/D$, $y^* = y/D$ and $t^* = t/(D/g)^{0.5}$. All trajectories display initial straight vertical lines where the motion is accelerated. For the case with smaller Archimedes number ($Ar = 14$), the bubble ascends in a straight line with a Reynolds number smaller than the critical one for vortex shedding as established in Figure 2.3. For the cases with larger Archimedes numbers, the short vertical segment where the bubbles have a monotonously accelerated motion, is followed by a zigzag oscillation in which the amplitude and frequency depend on the Reynolds number (see Figure 2.7). The point where the zigzag motion starts is where the bubble begins shedding vortices and forms a complex wake similar to a von Karman vortex street (a more complete description of the bubble wake is presented in sub-section 3.4.1). It is found that except in the region near the departure position at the bottom of the cell, the transversal oscillation of a bubble with $Ar = 28$ increases monotonically its amplitude as the bubble ascends to reach a terminal value of approximately 3.5 bubble diameters. In the flow regime where the bubble exhibits elliptical shapes, (Archimedes numbers 70 and 392), the trajectories display a zigzag motion with almost a constant amplitude along their trajectories, as it is shown in Figure 2.6. The amplitude of the oscillation in this range is an increasing function of the Archimedes number that saturates at about 5.5 diameters. Besides the oscillations described in the previous lines, we also observe transient oscillations with much lower frequency, that die out after approximately 300 bubble diameters for the range of Archimedes numbers explored.

In Figure 2.7, we show the instantaneous Reynolds numbers calculated with the horizontal (Re_x) and vertical (Re_y) components of the velocity as functions of time for $Eo = 0.84$, $Ar = 392$ and $Mo = 2.5 \times 10^{-11}$ which correspond to one of the trajectories presented in Figure 2.6. Since the kinematic viscosity and diameter of the bubble are constant, the Reynolds number can be considered as a non dimensional velocity. The large oscillation in the horizontal component is expected from the zigzag motion, as the red broken line in the figure indicates, but it is found that the vertical motion also displays a small oscillation superposed to its average value, with an amplitude of approximately 1/6 of the horizontal oscillation. The fact that the average vertical Reynolds number is much larger than the its horizontal counterpart (almost zero) is a consequence of the ascending motion of the bubble. The maximum Reynolds numbers attained by the two components are similar, but the frequency of the vertical velocity is twice as that of the horizontal component with the maxima of the vertical velocity coinciding with the zeroes of the vertical velocity trace. An analogous behavior was found in a fluttering solid ellipse that falls due to gravity as it is explained in Andersen et al. (2005). This phenomenon is generic to periodic and side-to-side oscillations superimposed to a constant average ascent or descent speed. It is interesting to note that the origin of this dynamic behavior is found in the small amplitude solutions of the Kirchhoff equations (see Andersen et al. (2005)). Although the comments above refer to the dominant harmonics of the velocity traces, it is important to observe

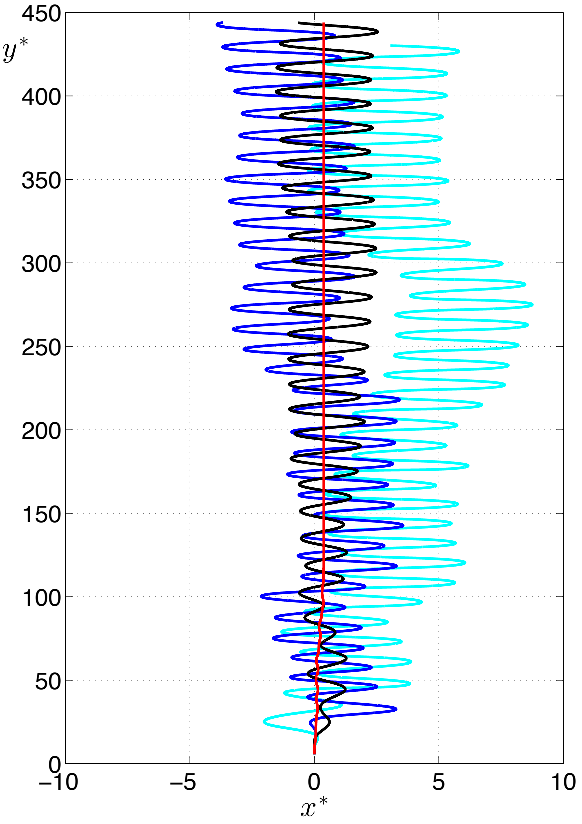

Figure 2.6: Trajectory of the centroid of individual bubbles for $Eo = 0.84$ and $Ar = 14$ (red), 28 (black), 70 (blue) and 392 (cyan). Note that the horizontal dimension has been amplified.

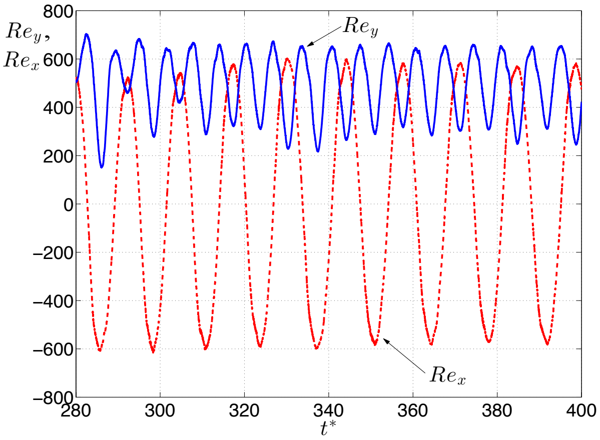

Figure 2.7: Horizontal and vertical Reynolds numbers as functions of time after the initial transient has died out. The blue trace is the Reynolds number defined with the vertical component of the velocity. The red trace is the Reynolds number defined with the horizontal component of the velocity. $Eo = 0.84$, $Ar = 392$ and $Mo = 2.5 \times 10^{-11}$.

that the vertical velocity is clearly not a simple harmonic and displays small variations in the amplitude. These relatively small effects can be attributed to the interaction of the bubble with the surrounding fluid. Due to viscosity and deformation, the interaction becomes much more complex (see section 3.4.1).

2.3.3 Shape and orientation of bubbles

As explained in the description of the chart in Figure 2.3, the geometry of the bubbles varies from essentially circular at small Eötvos numbers to ellipses and to deformed ellipses with flat bottom. The shape of the bubbles results from the interaction of the surface tension at the interface and the shear flow outside the bubbles which in turn depends on the phase of the zigzag oscillation. The shape of bubbles with small Eötvos numbers, is circular and they ascend in straight trajectories, accelerating at the initial stages and up to the point where a terminal velocity is attained. If the terminal Reynolds number is smaller than the critical one (black broken line in Figure 2.3), no vortices are shed and the stress at the surface is symmetric and not large enough to deform the bubble. In contrast, in the region of the map where the bubble acquires a zigzag motion, its shape and inclination is changing periodically during the whole ascending trajectory. This behavior is illustrated in Figure 2.8. In the left panel of the upper row, the inclination of the major axis of the elliptical bubble with respect to the horizontal during one cycle is shown as a function of its position in the horizontal coordinate. The time evolution of the inclination is indicated by the arrow. The shapes of the bubble at points A) and B) are shown in the mid row of this figure. In the right panel of the upper row, the aspect ratio of the bubble is plotted as a function of the horizontal position for one cycle of the bubble trajectory. As can be appreciated, under these conditions, the shape of the bubble is always elliptical, but there is a small (10%) change in the aspect ratio as the bubble ascends. The aspect ratio has a maximum and minimum value when it changes its direction in the zigzag motion. In the middle row of Figure 2.8, snapshots of the shape of the bubble are presented, the dynamical features of the motion can be also interpreted in terms of the inclination of the bubble as it ascends. In the left panel of the middle row, the inclination of the major axis of the bubble with respect to the horizontal in one cycle of oscillation is approximately -40°. The bubble has a positive inclination in position A) and a negative inclination in position B). The pressure fields near the bubble are also plotted for these positions. This oscillation in the inclination is consistent with an oscillatory, non-symmetric pressure field around the surface of the bubble. The vorticity field corresponding to the pressure fields of the mid row of Figure 2.8 are given in the lower row. Vorticity is generated more efficiently at the region of the bubble where the radius of curvature is minimum and two zones of concentrated vorticity appear. Vorticity is swept downstream by the relative velocity and evolves to form the wake. The dynamic behavior described above is summarized in Figure 2.9. The orientation of the bubble swings from - 45° to + 55° and the largest inclinations are found in the mid-line of the zigzag motion of the horizontal oscillation while the smallest inclinations are found where the bubble is in the extremes of the zigzag trajectory.

2.3.4 Forces and Torque on the bubble

As part of the post-processing of the data obtained, it is important to comment that the velocity of the centroid of the bubble was obtained by interpolating the velocity in the regular grid using the weighting function given by Peskin (1977). The hydrodynamical total force and the torque were calculated around the bubble, the force was computed integrating the stress tensor over a surface that surrounds the bubble. Such surface is constructed with the points $\mathbf{X}' = \mathbf{X}_p + h\mathbf{n}$, where $\mathbf{X}_p$ are the points of the interface and $\mathbf{n}$ is the unit normal vector to the interface. The main reason due to which the force was not integrated directly over the interface of the bubble is to avoid the pressure jump that exists through the surface of the bubble and then constructing a new surface out of the bubble the calculation of the force is more accurate. The expression to compute the force is given by:

$$\mathbf{F} = \int_s \left[-p\mathbf{I} + \mu\left(\nabla\mathbf{u} + (\nabla\mathbf{u})^T\right)\right] \cdot \mathbf{n}dS, \tag{2.3}$$

the integration was done by interpolating the values of the pressure and the tangential terms of the stress tensor to the surface using the Peskin weighting function. Once the components of the force given in the laboratory reference frame were computed, the force was projected to a reference frame (x', y') that moves with the bubble and it is oriented in accordance with the angle of inclination of the bubble.

The description of the forces exerted on the bubble that result in the trajectories presented in section 2.3.2, can be done in terms of two sets of axes of coordinates. The first one (x, y) is fixed in the laboratory frame of reference and the gravity force runs anti-parallel to the

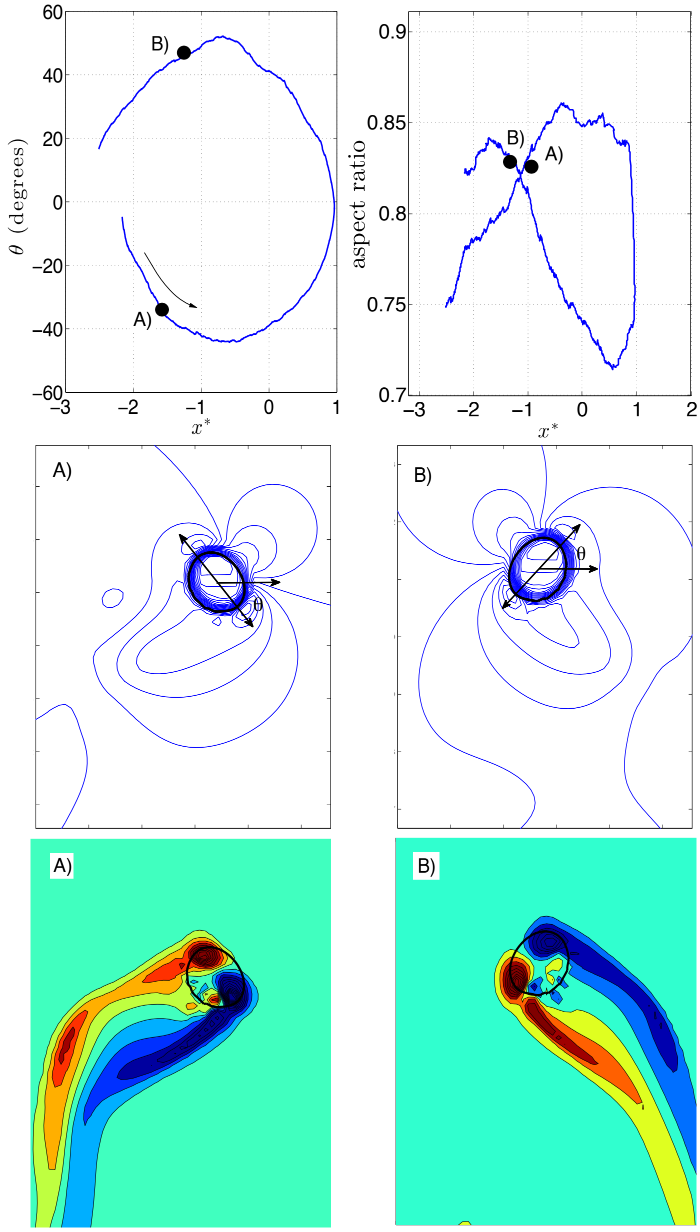

Figure 2.8: Orientation and aspect ratio of a bubble rising during one oscillation cycle with $Eo = 0.84$, $Ar = 392$ and $Mo = 2.5 \times 10^{-11}$. Upper row left: Inclination of the major axis of the elliptical bubble with respect to horizontal as a function of the horizontal coordinate. Time evolves in the direction of the arrow. The shape and orientation of the bubble at points labeled A) and B) are illustrated in the graphs in the lower rows. Upper row right: Aspect ratio as a function of the horizontal coordinate. Middle row: Shape and orientation of the bubble at points A) and B). The major axis is denoted by a double arrow line, the horizontal axis and the inclination angle θ are explicitly shown for reference. The lines denote isochores and their relative values near the bubble indicate the zones where pressure contributes to the deformation of the originally circular bubble. Lower row: vorticity field for positions A) and B).

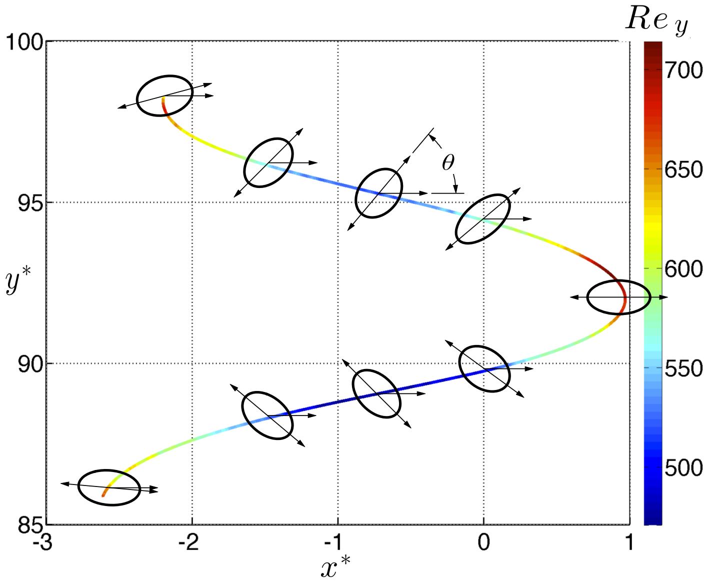

Figure 2.9: Orientation and aspect ratio as functions of the bubble trajectory for $Eo = 0.84$, $Ar = 392$ and $Mo = 2.5 \times 10^{-11}$. The color in the trajectory indicates the magnitude of the vertical velocity according to the color bar.

vertical coordinate. The second (x', y'), is fixed on the bubble and the axes of coordinates coincide with the major and minor axes of the ellipse that best approximates the shape of the bubble. In Figure 2.10, we show the projections of the resultant instantaneous force on the two axes of coordinates for four cycles in the case $Eo = 0.84$, $Ar = 392$ and $M = 2.5 \times 10^{-11}$, together with the corresponding x-position of the bubble. All forces in the figure have been scaled with $\rho g D^2 \pi$. As can be observed, the frequency of the F_y is twice that of F_x. This feature is consistent with the observation that the oscillation of the bubble trajectory oscillates in the y direction with the double frequency than that in the x direction. See Figure 2.7. The force in the horizontal direction alternates between positive and negative values to generate the zigzag motion. The force in the vertical direction F_y is always negative and it can be interpreted as a drag force that is balanced with the buoyancy force. The buoyancy force is a constant equal to $g(\rho_l - \rho_b)\pi D^2/4$, the sum of the vertical force and the buoyancy force must oscillate around zero when the bubble reaches an average vertical velocity. On the right hand scale of figure 2.10 c), the sum of the buoyancy and the calculated force is shown. The forces projected in directions parallel and perpendicular to the instantaneous displacement vector $\mathrm{F}_{x'}$ and $\mathrm{F}_{y'}$ respectively show a similar behavior as the forces in the laboratory reference frame, however, $\mathrm{F}_{x'}$ is in phase with the bubble position x and the maximum absolute value of F'_y coincides always with the point in which $\mathrm{F}_{x'}$ is zero. The trace of the torque as a function of time is composed of a small amplitude smooth oscillation and periodic positive and negative pulses that occur at the extreme positions of the zigzag motion where the tilt of the bubble changes sign.

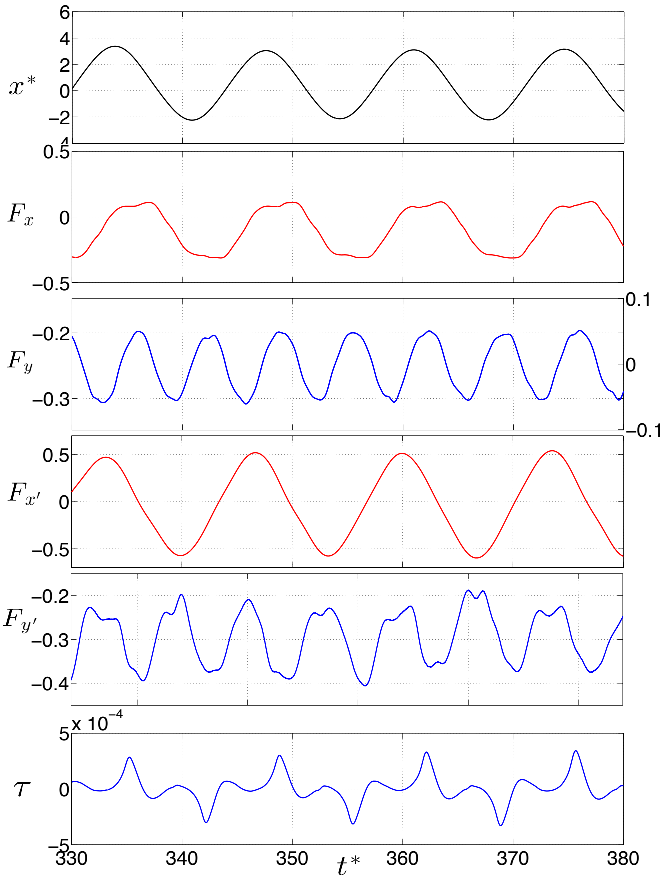

Figure 2.10: a) x position of the bubble as a function of time. b) and c) projection of the resultant force on the axes of coordinates fixed in the laboratory as functions of time. The scale on the right hand side of c) indicates F$_y$-$g(\rho_l - \rho_b)$d) and e) projection of the resultant force on the axes of coordinates fixed on the bubble as functions of time. f) Torque on the bubble as a function of time.

2.3.5 Bubble Wake

The motion of individual bubbles has been discussed focusing on the description of bubble trajectories, shape and orientation, but as it will be described in this section the dynamics of the rising bubble is also related to its wake structure. When the bubble ascending velocity is small, a wake with symmetric, closed recirculation rings is formed, and a low pressure zone is generated at the recirculation centers (Piedra 2011). For larger vertical Reynolds numbers, the attached vortical pocket becomes unstable and the wake detaches from the bubble. This phenomenon was found when the bubbles exceed the critical Reynolds number reported with a black broken line in the chart of Figure 2.3. In order to illustrate the flow generated by the motion of the bubble, a snapshot of the velocity, pressure and vorticity fields in the wake of the ascending bubble are shown in Figure 2.11 for the case $Eo = 0.84$, $Ar = 392$ and $Mo = 2.5 \times 10^{-11}$. The most conspicuous feature observed is that vortices are created on the lee side of the bubble and detach periodically from either side. As commented in the previous section, vorticity is generated more efficiently at the regions of the bubble with the smallest radius of curvature and as the bubbles pitch as they ascend, the regions of concentrated vorticity move up and down in the frame of reference moving with the vertical average velocity of the bubble. When the translation velocity is large enough, slender regions of concentrated vorticity are swept and trail behind the bubble. Inside the elongated vortex regions the vorticity is not uniform and the fluid rotates around locations with maximum vorticity forming localized vortices. This picture is similar to the one presented by Perry et al. (1982) to describe the wake formation behind a fixed rigid cylinder where the alternate position of the vortices shed by the cylinder is brought about by a different mechanism, namely, the symmetry breaking of the attached vorticity bubble. The collection of vortices shed by the bubbles is similar to the von Karman vortex street generated by a rigid cylinder in relative motion with respect to a fluid. Alternate single vortices with vorticity of opposite sign are shed (2S in the terminology introduced by Williamson & Roshko (1988)). The geometry of the wake can be characterized by the separation between adjacent vortices in the streamwise and traversal directions as indicated in Figure 2.11. As expected, the local minima in the pressure field correspond to the maximum concentration of vorticity. We find that streamwise and traversal distances between vortices normalized with the bubble diameter, a and b are 10.3 and 4.4 respectively. We find that these parameters are approximately constant for the range of terminal Reynolds numbers explored. This vortex distribution yields $b/a = 0.43$ which is almost twice as large as that reported by von Karman ($b/a = 0.28$) for a stable distribution of an infinite row of alternate vortices (see Williamson (1996)). Due to the asymmetric wake structure, the forces acting on the bubble will also become unbalanced, and the bubble tilt changes periodically. This effect adds to the oscillation induced by the geometry discussed in the previous sections.

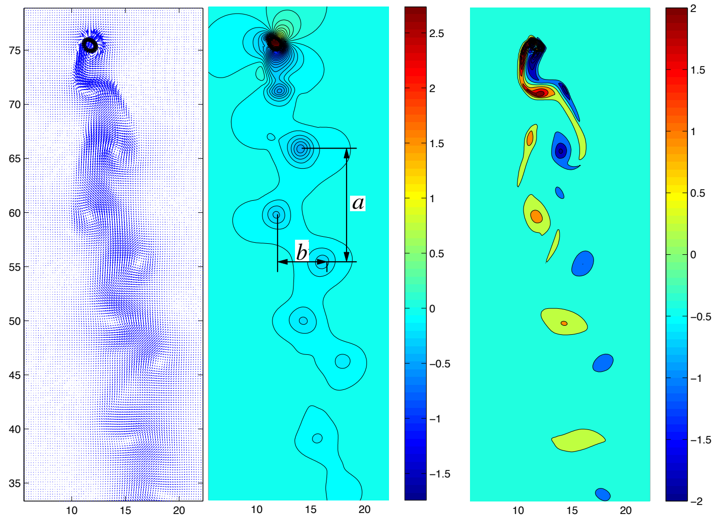

Figure 2.11: Vortex shedding around a single bubble, velocity, pressure and vorticity fields for $Eo = 0.84$, $Ar = 392$ and $Mo = 2.5 \times 10^{-11}$. a= 10, b= 4.4.

2.4 Comparison with experimental results in a Hele-Shaw cell

Here, we compare the results obtained with the two dimensional model described in the previous sections with experimental observations. No two dimensional bubbles can be generated in the laboratory but a reasonable approximation can be achieved by feeding bubbles in a liquid filled Hele-Shaw cell where the motion in one of the horizontal directions is restricted by the plates that form the cell. The most important difference between the idealized two dimensional model and a bubble dynamics is the flow and bubble interaction with the vertical parallel walls of the cell. A very informative study of the dynamics of individual bubbles in a Hele-Shaw cell is that of Roig et al. (2012) where air bubbles were observed ascending in water in a cell with a 1 mm gap. The observations were reported in terms of the apparent diameter of bubbles D. A crucial observation is that the terminal Reynolds number is a linear function of the Archimedes number, with the constant of proportionality being 1/2. Inspection of Figure 2.12 indicates that the two dimensional model does predict the linearity between the Reynolds and Archimedes numbers but with the proportionality constant of unity. We set to explore the dynamics of the ascending bubbles, but using Hele-Shaw cells with different gaps where bubbles of the same apparent diameter but different actual volume could be formed. In spite of having the same apparent diameter, the different gaps make the total volume of the bubbles different and consequently different buoyancy force.

Experiments were carried out for three different cells with gaps of 1 mm, 2 mm and 2.5 mm, and in a range of Archimedes number of $2 \times 10^2 < Ar < 2 \times 10^3$, with apparent diameter of the bubbles from 2 mm to 7.3 mm. In Figure 2.12, the relation between the Archimedes and Reynolds numbers resulting for the experiments of the three different gaps is shown. In all cases, the linear behavior of the Reynolds respect to the Archimedes number can be observed. However, we find that the slope of the line changes as a function of the gap. For the cell with a gap of 1 mm (black circles), the slope of the line is 0.5 confirming the value reported by Roig et al. (2012); in the case of the cell with gap of 2 mm (blue squares), the slope of the line that describes the Reynolds number results is 0.6, and in the cell with a gap of 2.5 mm the slope is 0.65. In Figure 2.12 we also plot the result of the numerical simulations, i.e. the Reynolds number is a linear function proportional to the Archimedes number with slope equal to 1 (red stars). We conclude that even when the simulations cannot be compared in quantitative form with the experiments in a Hele-Shaw cell, they can give us all the qualitative information of the dynamics of bubbles as the linear dependency of the Reynolds number respect to the Archimedes number. In Figure 2.13, the experimental trajectory of the bubble in the Hele-Shaw cell with gap of 2 mm is shown (left hand side) and the trajectory computed from the numerical simulation for $Ar = 392$, $Eo = 0.84$ and $Mo = 2.5 \times 10^{-11}$ is plotted on the right hand side. In both experiment and simulation, the bubble has a diameter of 2.5 mm. As can be observed, the qualitative agreement with the simulations is satisfactory, but the model overestimates the trajectory swing yielding an oscillation with amplitude larger by a factor of four and smaller frequency (factor of two). These estimates were also observed for the other two cases explored (gaps with 1 and 2.5 mm). The Strouhal numbers found for the different gaps can be represented by the expression A/Re + B+C Re with A= -3.3, B= 0.34 ± 0.05 and 5×10^{-4} <C< 10^{-3} which differ from the two dimensional theoretical calculation (see Section 2.3.1) and are consistent to those found by Kelley and Wu Kelley & Wu (2005) with a similar experimental arrangement.

In the experiments as well as in the simulations, the vertical position of the bubble as a function of time is a wavy line that can be approximately represented by a straight line; the slope of this line is the average vertical velocity. The quantitative mismatch is again interpreted as the failure of the model to incorporate the effect of the glass plates. The side by side oscillation of the trajectory is better described in the frame of reference of a system that travels with the average vertical velocity. A result obtained in this way is given in Figure 2.14 where the orbit of the centroid of the bubble in the $(x, y - y_{ave})$ space is shown. The results of the simulation are in qualitative agreement with the experimental data with quantitative differences similar to those that have been discussed previously. Another feature that can be captured by the two dimensional model is the instantaneous Reynolds number. In Figure 2.15, the Reynolds numbers calculated with the vertical and horizontal velocity components as functions of time were found from the experimental observations. The results are very similar to those computed with the numerical simulations plotted in Figure 2.7. Specifically, we observe that the frequency of the oscillation of the vertical velocity is twice that of the horizontal velocity. Experimental observations of the external flow generated by the motion of the bubble are illustrated in Figure 2.16. Visualization of the wake of the bubbles ascending in cells with different gaps was done using Kalliroscope speckles. Figure 2.16 shows that the wake of bubbles with the same apparent diameter (2.5 mm) in cells of 2 and 2.5 mm are formed by alternating vortices shed by the bubbles. The vortices conform a structure very similar to the von Karman vortex street, in qualitative agreement with the corresponding numerical

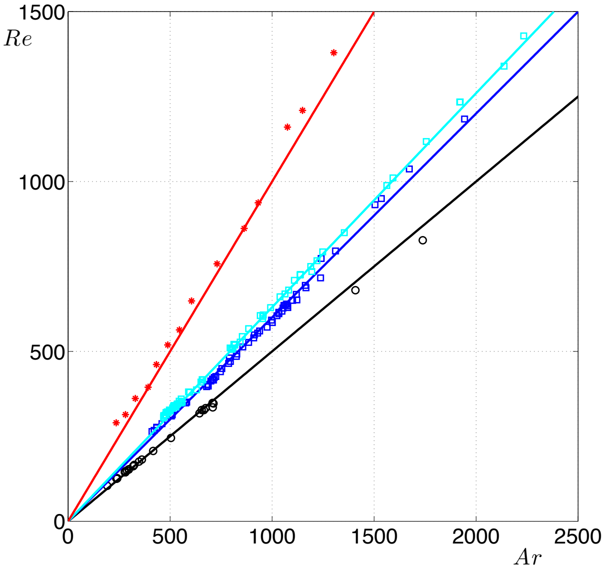

Figure 2.12: Relation between the Reynolds and Archimedes numbers for the Hele-Shaw cells with the three different gaps and the numerical simulations. The black circles, blue squares and cyan squares correspond to the experiments with gaps 1 mm, 2 mm and 2.5 mm, respectively. Red stars correspond to the results from the numerical simulations.

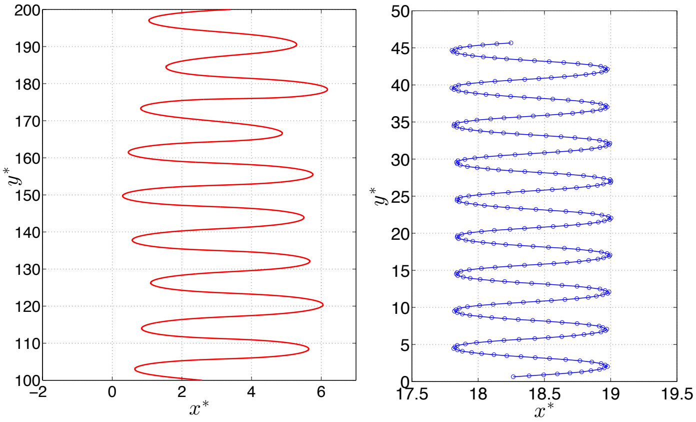

Figure 2.13: Comparison of the numerical trajectory of the bubble with experiment in a Hele-Shaw cell. The left panel presents the numerical simulation ($Ar = 392$, $Eo = 0.84$ and $Mo = 2.5 \times 10^{-11}$) and the right panel corresponds to the experimental observation in a cell with a gap of 2 mm .

	2.0 mm	2.5 mm (near)	2.5 (far)	Numerical
a	5.5	3.6	8.6	10.3
b	2.5	2.9	3.3	4.4
b/a	0.45	0.81	0.38	0.44

Table 2.1: Geometrical parameters in the wake of bubbles

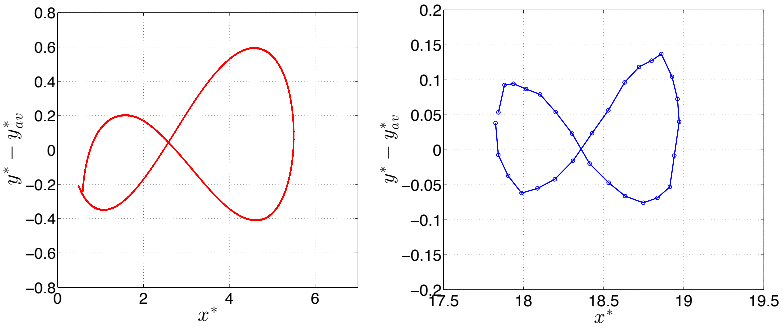

Figure 2.14: Position of the centroid of a single bubble as recorded in a frame of reference ascending with the average vertical velocity. On the left side is the numerical simulation result ($Ar = 392$, $Eo = 0.84$ and $Mo = 2.5 \times 10^{-11}$) and on the right side is the experimental observation.

results. However, there are important quantitative discrepancies. In order to illustrate the differences, the inter-vortex spacing in one row (a) and the distance between vortex rows (b) and their ratio are given in Table 2.1 for two representative cases of bubbles with apparent diameter of 2.5 mm. In the case of the 2 mm gap cell, the ratio b/a does not depend on the distance to the bubble and, is approximately equal to that obtained with the numerical calculation. This feature can be understood since the vertical velocity of the model is twice as that of the experiment (see Figures 2.7 and 2.15) and the oscillation frequency of the model is half that of the experiment (see Figures 2.13). In contrast, for the 2.5 mm gap cell, the ratio b/a is a function of the distance from the bubbles and notably reduces for vortices located further downstream. Although the wake is clearly composed of alternate, opposite sign vortices characteristic of the von Karman wake, the evolution of the vortices in wake is an indicative that the flow is not totally confined by the plates of the Hele-Shaw since the diameter of the bubble and the distance between the plates is the same.

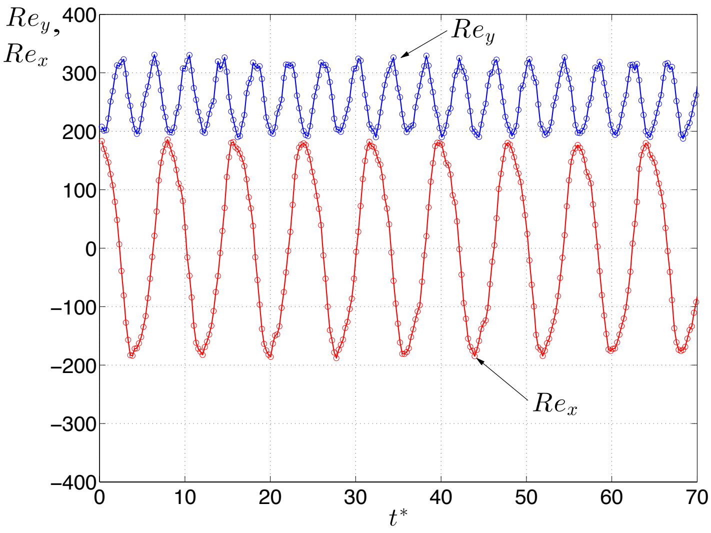

Figure 2.15: Experimental Reynolds number as a function of time. The blue trace is the vertical Reynolds number. The red trace is the horizontal Reynolds number.

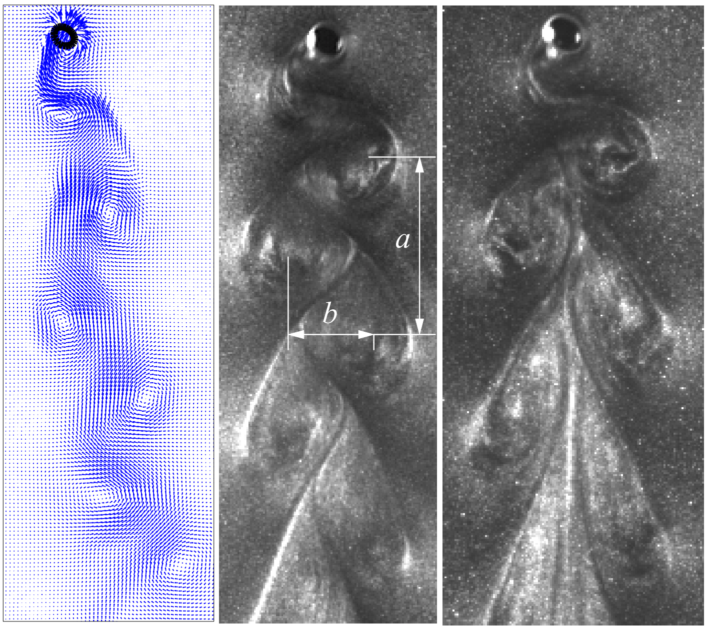

Figure 2.16: Vortex shedding in the wake of the bubble. Left, the numerical velocity field. In the center, the experimental visualization in the cell with a gap of 2.0 mm and on the right, the experimental visualization in the cell with a gap of 2.5 mm are presented.

Chapter 3

Dynamics of three dimensional bubbles

3.1 Background

The dynamics of bubbles has been studied from the experimental, theoretical and numerical points of view for many years due to its importance in many applications. However, it is only in recent years that direct numerical simulations have been developed in order to understand in detail the physical effects that determine the motion of bubbles at different flow conditions (see for instance Hua & Lou (2007), Ohta et al. (2005), Chen et al. (1999) and van Sint Annaland et al. (2005)). Some authors reported numerical studies of the interaction of multiple bubbles at different flow conditions paying attention to the average behavior of the flow and the influence of the presence of the bubbles in the flow. Examples of specific flows are given in Bunner & Tryggvason (2002*a*), Bunner & Tryggvason (2002*b*), Lu et al. (2005) Lu & Tryggvason (2006) and Lu & Tryggvason (2008). Although this has then a major improvement in understanding the dominant physical effects of the bubble dynamics, there is a prevalent problem in most of the studies available in the literature, namely that in most of the cases the flow conditions considered are at low to moderate Reynolds numbers and, consequently, that the systems are very far from the real experimental conditions. In this work, the finite volume/front-tracking method described in the second chapter was implemented to simulate the motion of bubbles in a stagnant fluid considering real conditions for air bubbles in water and we will try to compare some features of the flow with experimental data reported in the literature. In the first part of the chapter the results of the simulations for single bubbles at low and high Reynolds numbers are presented. In the last part, the simulations of the interaction of multiple bubbles are shown in order to demonstrate the applicability of the code developed in this project to model bubbles at different conditions. The main objective is to simulate real systems of air bubbles and water and have a numerical tool to study the bubble dynamics in a large range of flow conditions and for a single and multiple bubbles.

3.2 General comments

In the early literature, bubbles rising in a viscous fluid were grouped in three categories: “Spherical”, where the surface tension and viscous forces are much more important than the inertia forces. “Ellipsoidal”; the name usually given to bubbles which are oblate with a convex interface around the entire surface, and “Spherical cap” or “Ellipsoidal cap”, that are large bubbles that tend to adopt flat or indented bases and that lack any semblance of fore-and-aft symmetry. If the bubble has an indentation at the rear, it is often called “dimpled”. Large spherical- or ellipsoidal-cap bubbles may also trail thin envelopes of dispersed fluid referred to as “skirts”. The qualitative classification of bubble shapes and dynamics are based on non dimensional numbers which reflect the dominant physical effects. Recall that the definition of those non-dimensional numbers was introduce in the previous chapter (Equations 2.1 and 2.2).

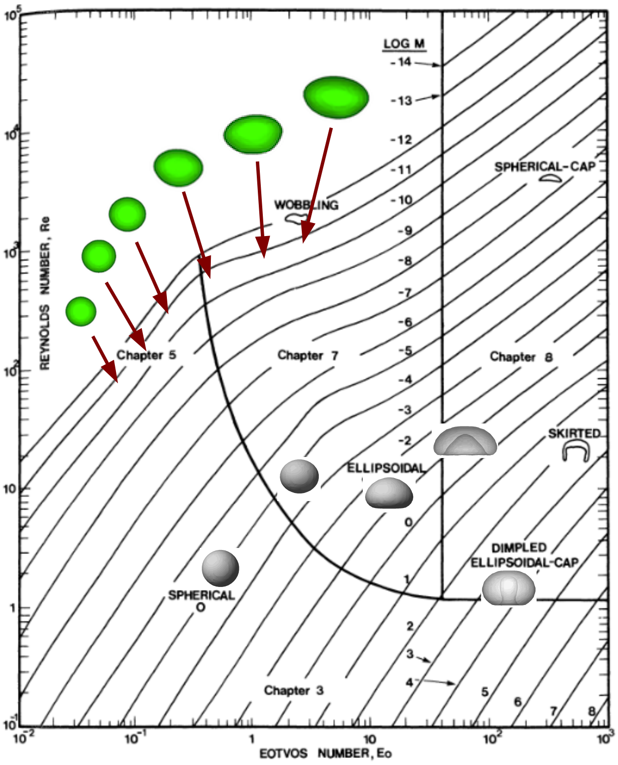

Figure 3.1: Shape regime for bubbles through liquids (Clift et al. 1978).

Many efforts to experimentally observe individual bubbles rising in a viscous fluid have been done for a wide range of flow conditions. The results presented in Sanada et al. (2007), Bhaga & Weber (1981), Veldhuis et al. (2008) and Mingming & Morteza (2002) are some examples of them. However, the best known reference in the bubbles research is the work of Clift et al. (1978) where a comprehensive chart of the qualitative shape of the bubbles for a wide range of flow conditions as function of the non dimensional parameters was reported (see Figure 3.1), shapes of the bubbles are separated by continuous lines). While the boundaries between the principal shape regimes are plotted somewhat arbitrarily it is clear that bubbles are ellipsoidal at relatively high Reynolds numbers and intermediate Eötvos numbers and spherical-cap and ellipsoidal-cap bubbles appear when both, Eötvos and Reynolds are large.

3.3 Numerical Simulations of single bubbles at low terminal Reynolds number

In this section, the results for the simulation of individual bubbles for different flow conditions are presented. We focus on cases with low Reynolds numbers in which the wake behind the bubbles is axis-symmetric and the bubbles follows a straight trajectory. The numerical solutions were obtained in a periodic parallelepiped domain with a quadrilateral base whose size is 6 bubble diameters in the horizontal sides and 24 bubble diameters of height, such domain was discretized in a grid of 100 × 100 × 300 control volumes. Notice that a spherical shape of the bubble was imposed as an initial condition for all the numerical simulations.

Examples of the bubble shapes predicted by our calculations are shown in Figure 3.2 for the flow conditions marked in the chart and as can be observed, the qualitative shape of the bubbles obtained with our numerical simulations coincides in all cases with the chart. As we increase the Eötvos number, the bubble shape changes from the spherical to the ellipsoidal and dimpled form. This is because the increment of this non-dimensional parameter is equivalent to decrease the surface tension.

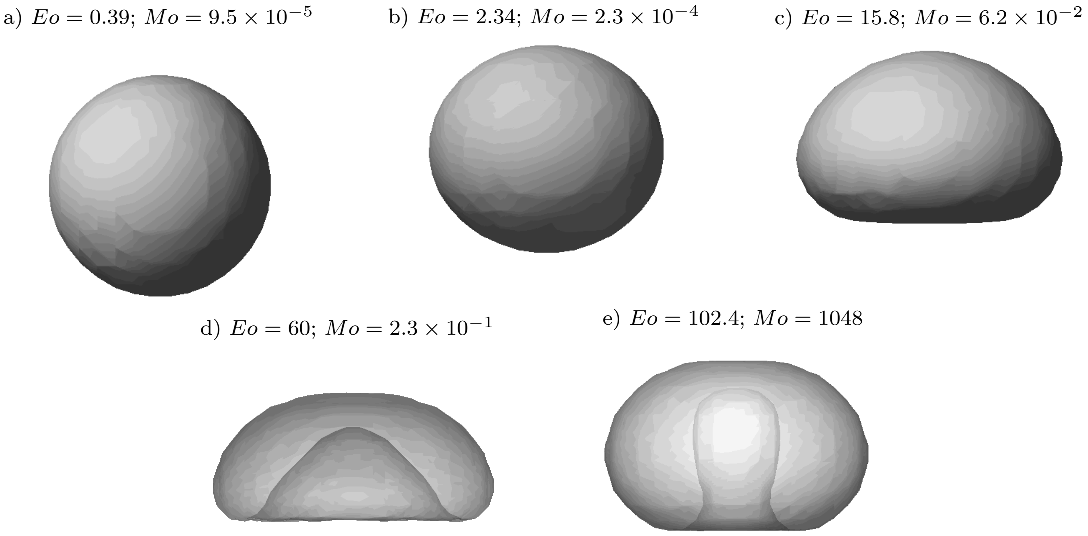
a) $Eo = 0.39$; $Mo = 9.5 \times 10^{-5}$
b) $Eo = 2.34$; $Mo = 2.3 \times 10^{-4}$
c) $Eo = 15.8$; $Mo = 6.2 \times 10^{-2}$
d) $Eo = 60$; $Mo = 2.3 \times 10^{-1}$
e) $Eo = 102.4$; $Mo = 1048$

Figure 3.2: Bubble shapes for different flow conditions.

The velocity of the centroid or, equivalently, its Reynolds number, is an important parameter for the description of the bubble dynamics. The Reynolds number depends on the vertical velocity, which is computed with the expression:

$$w_b = \frac{1}{V_b} \int_{V_b} w dv. \tag{3.1}$$

The velocity of the centroid of the bubble is calculated at each time step in our simulations. With such velocity, the instantaneous Reynolds number was computed; in Figure 3.3 the Reynolds numbers are plotted as functions of time for the simulations of the Table below. As it is shown, in cases with $Eo \leq 60$, the Reynolds number increases until it reaches a constant value, called the terminal Reynolds number; this is the value plotted in the shape chart given by Clift et al. (1978). For $Eo = 102$, the evolution of the Reynolds number displays subsequent maxima before attaining the terminal velocity value. This is caused by the extra drag produced due to the deformation of the bubbles at those large Eötvos numbers. In the first stage of the rising, the bubble initializes with spherical shape and it accelerates until a maximum value; however, as the bubble deforms the drag force is larger and produces a decrement in the velocity of the bubble until it reaches a steady state and its shape does not change anymore.

The flow around the bubble is presented in Figure 3.4, for $Eo = 15.8$, $Mo = 6.2 \times 10^{-2}$ and terminal $Re = 8.9$, where a slice of the velocity field is also plotted. As can be observed, the flow formed around the bubble is a dipole vortex, the features of which depend on the non-dimensional numbers. The axisymmetric nature of the wake of the bubbles causes that the bubbles at low Reynolds numbers rise in a rectilinear path. Additionally, to illustrate the disturbance that the transit of a bubble causes on the pressure field of the fluid, Figure 3.4 displays the pressure field for the parameters given in case c) of Figure 3.3. The hydrostatic pressure field can be identified as a gentle constant background pressure gradient. The surface tension forces on the bubble keep the pressure inside it nearly constant and higher than the ambient pressure. Also the center of the vortices move away from the bubble and the low pressure zones intensify behind the bubble.

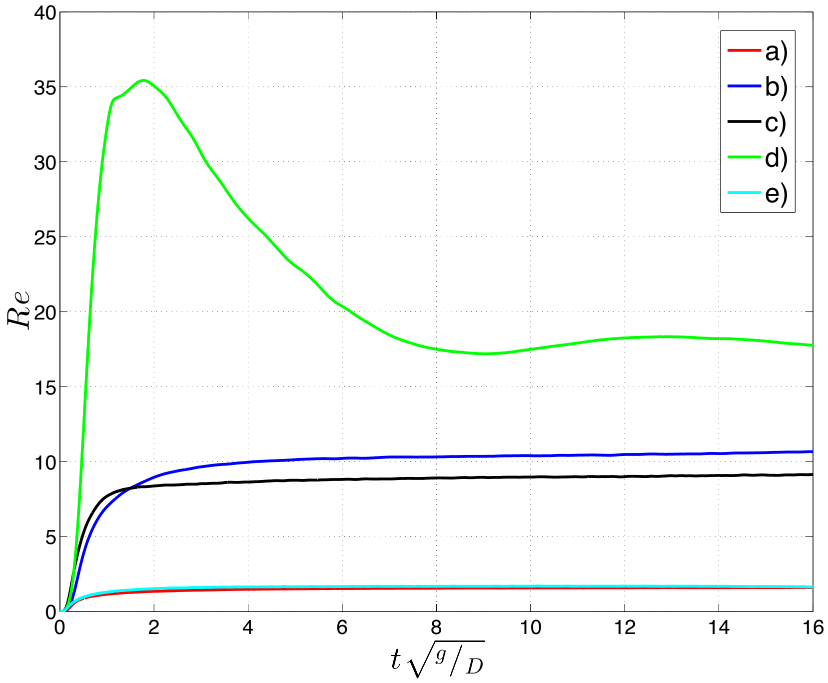

Case	Eo	Mo	Re_{sim}
a)	0.39	9.5×10^{-5}	1.58
b)	2.34	2.3×10^{-4}	10.59
c)	15.8	6.2×10^{-2}	8.9
d)	60	2.3×10^{-1}	17.06
e)	102.4	1048	1.67

Figure 3.3: Temporal evolution of the Reynolds number, and a Table indicating the parameters used in the simulations shown in the plot.

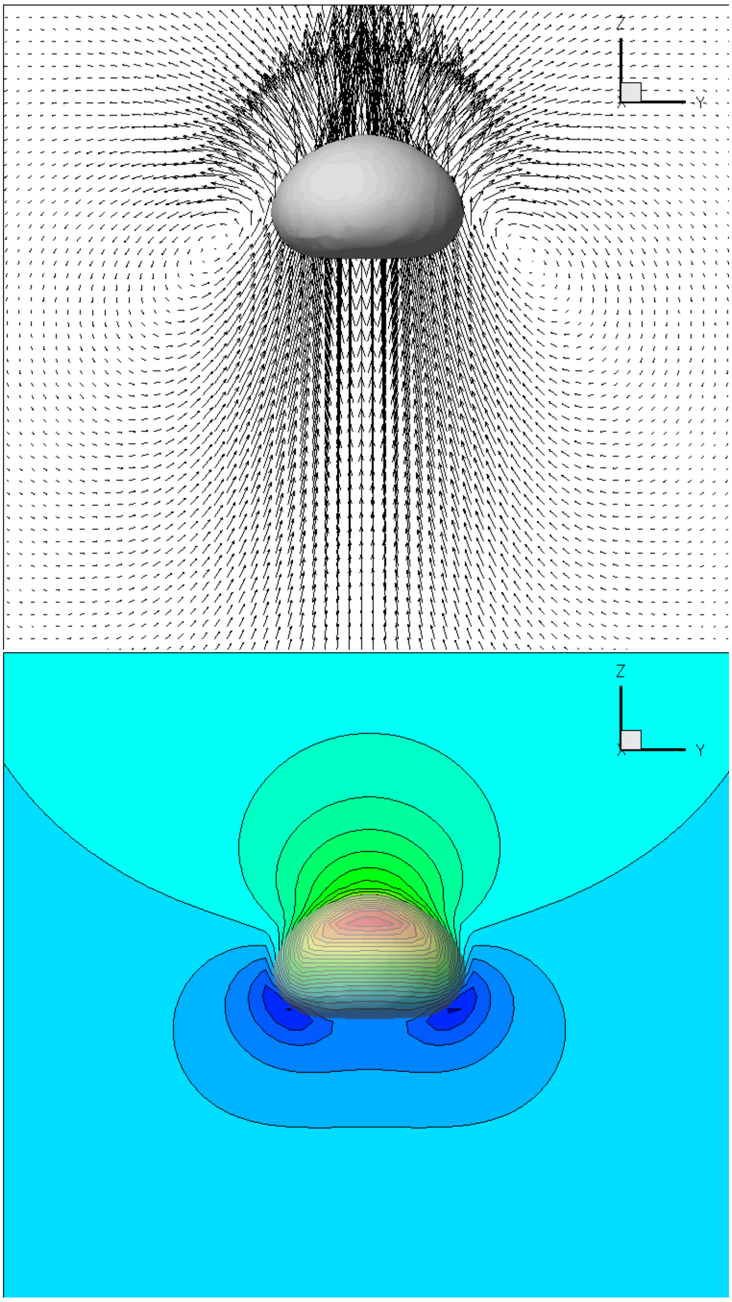

Figure 3.4: Velocity and pressure fields around the bubble for $Eo = 15.8$ and $Mo = 6.2 \times 10^{-2}$.

3.4 Numerical Simulations of single bubbles at high Reynolds number

Experimental conditions of interest in many industrial applications indicate that the terminal Reynolds numbers based on the ascending velocity in a column of fluid are on the order of 10^2 or larger. As will be explained in detail below, the dynamics of the bubbles and their wakes are very different from those described in the previous section. For this reason, we proposed as one of the main objectives of this project to simulate bubble dynamics under conditions similar to those found in industrial applications where qualitative changes in their motion patterns are found. In this section the simulations at high Reynolds numbers of an individual bubble motion are presented. In the chart given by Clift et al. (1978) (Figure 3.1), the shape of the bubbles for different flow conditions can be observed. The resulting shape of our numerical simulations for high Reynolds numbers are plotted in green color in Figure 3.1, and as it can be seen the numerical results are in agreement with those reported in the chart. The simulations correspond to air bubbles in water; the Reynolds number varies from about 10^2 to 10^3. Since the simulations correspond to the same pair of fluids the Morton number is constant and equal to 2.5×10^{-11} for all cases presented in this section. The shape of the bubbles changes from spherical to ellipsoidal as we increase the Eötvos and Reynolds numbers and the motion of the bubbles is more complex than the cases shown in the previous section.

The results presented in this section correspond to air bubbles in water, the simulations were performed in a large liquid column with dimensions $8 \times 8 \times 80$ bubble diameters discretized by a uniform mesh of $128 \times 128 \times 1280$. For the lateral walls, non-slip boundary conditions were imposed and the domain is periodic in the vertical direction. The bubble path and the wake behind the bubble are analyzed for single bubbles and also, the results are compared with the experiments reported in the literature in order to validate the code.

3.4.1 Wake and its influence on the bubble path

When the bubbles rising in a viscous fluid exceed a critical Reynolds number they do not rise in a rectilinear path, but in zig zag or a spiral path. The cause of this instability in the motion of the bubbles is not well understood and there are many differences of the value of the critical Reynolds number in the experimental studies reported in the literature (see Table 3.1). Mingming & Morteza (2002) and some experimental works in the literature report that for the same bubble size but different initial conditions the motion of the bubble is very different (Mingming & Morteza (2002)). Then it is very difficult to validate the numerical simulations with experimental data at this flow regime. Direct numerical simulations of bubbles have been presented in Esmaeeli & Tryggvason (1999*a*), Esmaeeli & Tryggvason (1999*b*), Gunsing (2004) and Hua & Lou (2007). Most numerical simulations are restricted to low Reynolds numbers or short time simulations or both. Experimentally, the rising of single bubbles has been studied and the three different

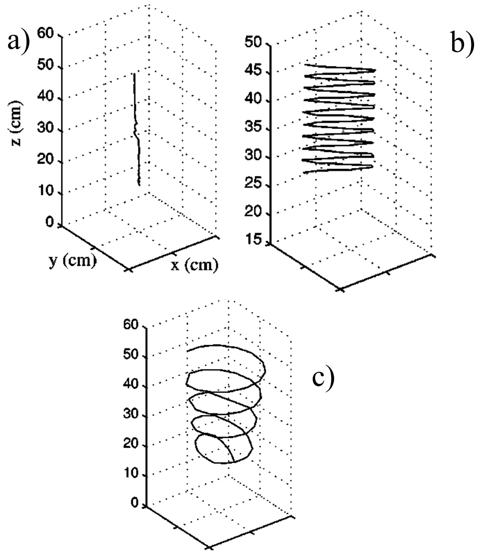

Figure 3.5: Motion patterns for different bubble sizes (Mingming & Morteza (2002)).

Authors	Re_c
Clift et al. (1978)	450
Veldhuis et al. (2008)	500
Mingming & Morteza (2002)	275 ± 25

Table 3.1: Different values of the critical Reynolds number reported in the literature.

motion patterns of the bubble are reported in the literature (Mingming & Morteza (2002), de Vries (2001) and Shew et al. (2006)). In Figure 3.5 the path of three different bubbles found experimentally is illustrated with the reconstruction of the position of the centroid of the bubble as a function of time.

Simulations were performed using the numerical implementation described in the previous chapters in order to find the instability in the path of the bubbles that produces the change in the motion pattern. One of the main objectives of the study was to demonstrate that our code is able to capture this dramatic change in the path of the individual bubbles.

In Figure 3.6, the two dimensional projections of the trajectories for three different simulations with D = 0.8, 2.5, 3.5 and 4 mm are shown. The trajectories are presented in a non-dimensional form and the variables were normalized using the diameter D as the characteristic length. As can be observed, for the bubble of 0.8 mm in diameter the trajectory is almost a straight line, for the bubble of 2.5 mm in diameter, the trajectory exhibits an irregular oscillation and for the bubble of 3.5 mm and 4 mm in diameter the trajectory of the bubble oscillates in the x and y directions with a well defined frequency. As it has been reported in the literature, the numerical simulations reproduce the instability in the path of the bubbles when the Reynolds number exceeds a critical value. For the case of the bubble of 3.5mm in diameter, in Figure 3.7 the three dimensional trajectory of the centroid of the bubble is plotted. As can be observed, the trajectory describes a spiral motion that has been reported by several authors in the experimental studies. After the initial vertical rectilinear motion, the lateral motion appears and the bubble rotates forming a (non-perfect) spiral trajectory.

After the computation of the centroid of the bubbles as a function of time, it is possible to calculate the velocity of the centroid; for the case where the bubbles follow a rectilinear path, the velocity of the bubbles at those Reynolds numbers was presented in the previous section. In Figure 3.8, the vertical velocity as a function of time is shown for the case of the bubble of 3.5mm in diameter. It is clear that as the path of the bubble, its vertical velocity oscillates with a constant frequency after the initial period of time in which the bubble is accelerated. It is possible to calculate an average vertical velocity and a Reynolds number for this case that is equal to 921. On the right side of Figure 3.8, the components of the velocity in the x and y coordinates are plotted, the lateral velocities oscillate around zero and are out of phase approximately half period from each other. Also, it is important to highlight that as in the two dimensional results, the frequency of the vertical velocity is twice the frequency of the lateral motion of the bubble.

The trigger of the instability in the path of a single bubble rising can be explained when the nature of the wakes for different flow conditions is explored. For bubbles when the Reynolds number does not exceed the critical value for the vortex shedding, we found an axisymmetric wake behind the bubbles. In the left side of Figure 3.9 the flow around a single air bubble of 0.8mm in diameter is plotted. In order to visualize the wake, we used streamwise vorticity isosurfaces and it is clear that the wake is conformed by two elongated and symmetric vortices; since the pressure field is axisymmetric, the bubble follows a rectilinear path as it was shown in the first trajectories of Figure 3.6. The vortices formed in this case are similar to the vortices generated by the flow around a solid sphere (see for example Ormieres & Provansal (1999)). On the other hand, when the Reynolds number is increased and exceeds a threshold, the qualitative pattern of the vortices in the wake of the bubble changes dramatically. In the right side of Figure 3.9, a snapshot of the flow around an air bubble of 3.5mm in diameter is represented using again the isosurfaces of the streamwise vorticity. Unlike the smaller bubbles, in this case the vortices in the wake of the bubble exhibit an irregular behavior; at a certain instant of time the two vortices break down and near the bubble two new vortices are generated and detached with a regular frequency. For the case plotted in Figure 3.9, the frequency of the vortex shedding calculated from our simulations was about 6.4Hz. Since the flow is non-axisymmetric, new components of the forces over the bubble are produced and the bubble is accelerated along the horizontal axes. Also, the acceleration in these directions is periodic due to the vortex shedding and the bubble moves in a spiral trajectory.

3.4.2 Comparison with experiments

The numerical code was validated using experimental data found in the literature. There are several experimental results for air-water systems, but, as commented before, from

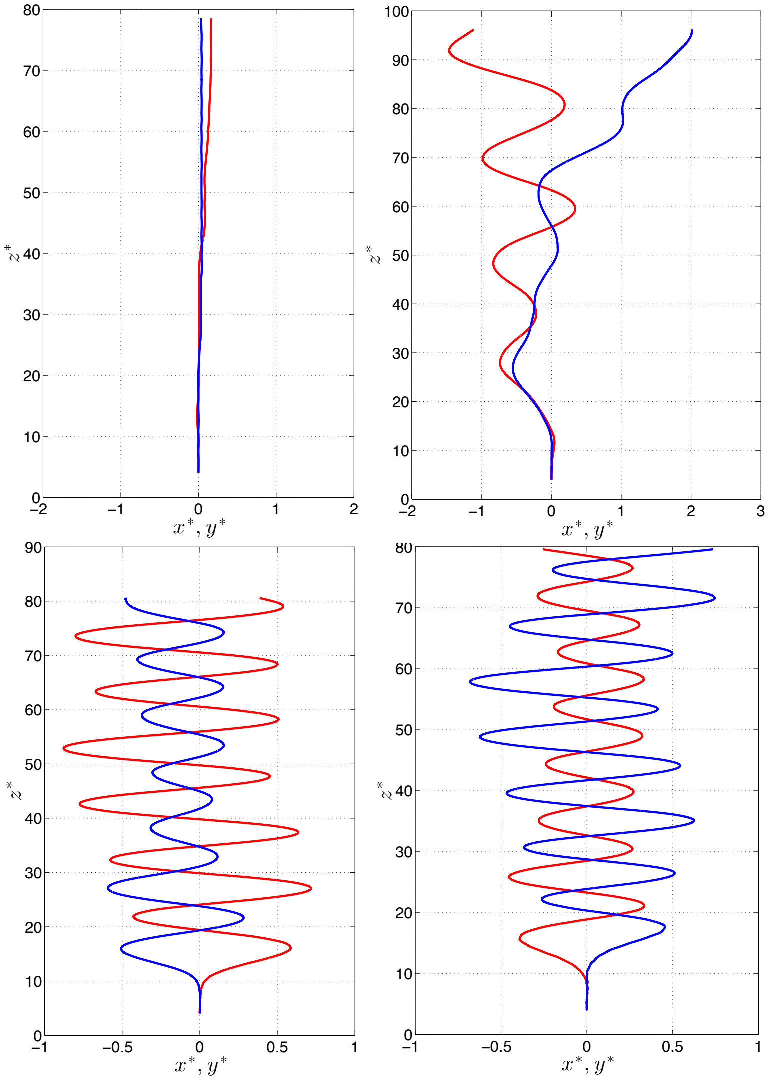

Figure 3.6: Two dimensional projections of the non-dimensional trajectory of an air bubble in water. The red curve is the trajectory in the x direction and the blue one is in the y direction, a) D =0.8mm, b) D =2.5mm, c) D =3.5mm and D =4mm ($M = 2.5 \times 10^{-11}$ and Eo =0.086, 0.84, 1.64 and 2.5, respectively).

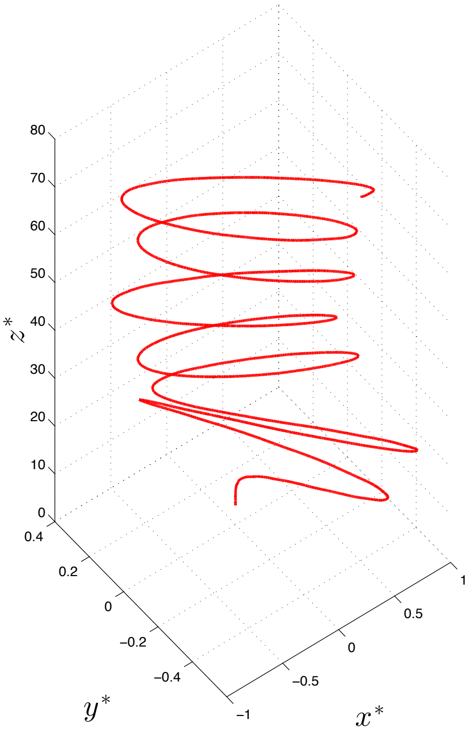

Figure 3.7: Helical trajectory followed by an air bubble in water, D =3.5mm ($Eo = 1.64$, $Ar = 720$ and $Re = 921$).

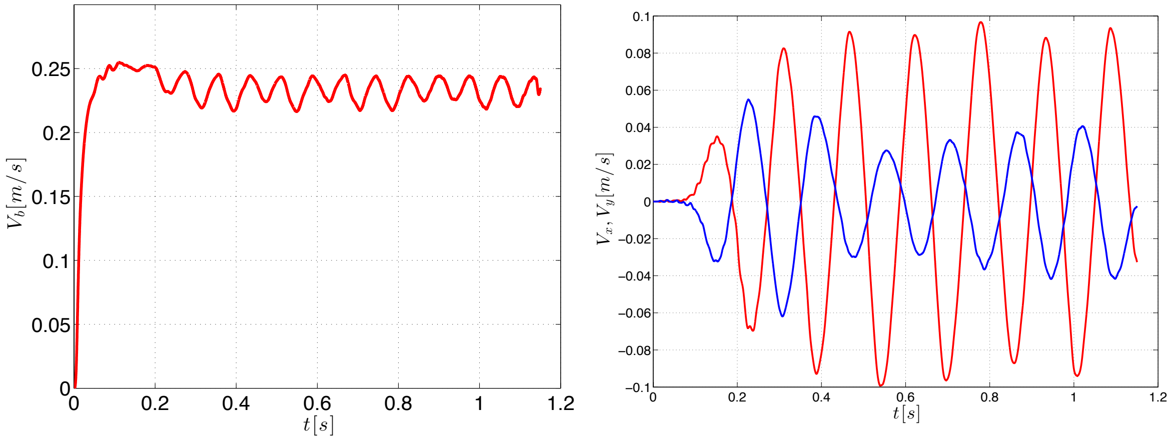

Figure 3.8: Velocity of the centroid of the bubble, left side: vertical velocity, right side: horizontal velocity components ($Eo = 1.64$, $Ar = 720$ and $Re = 921$).

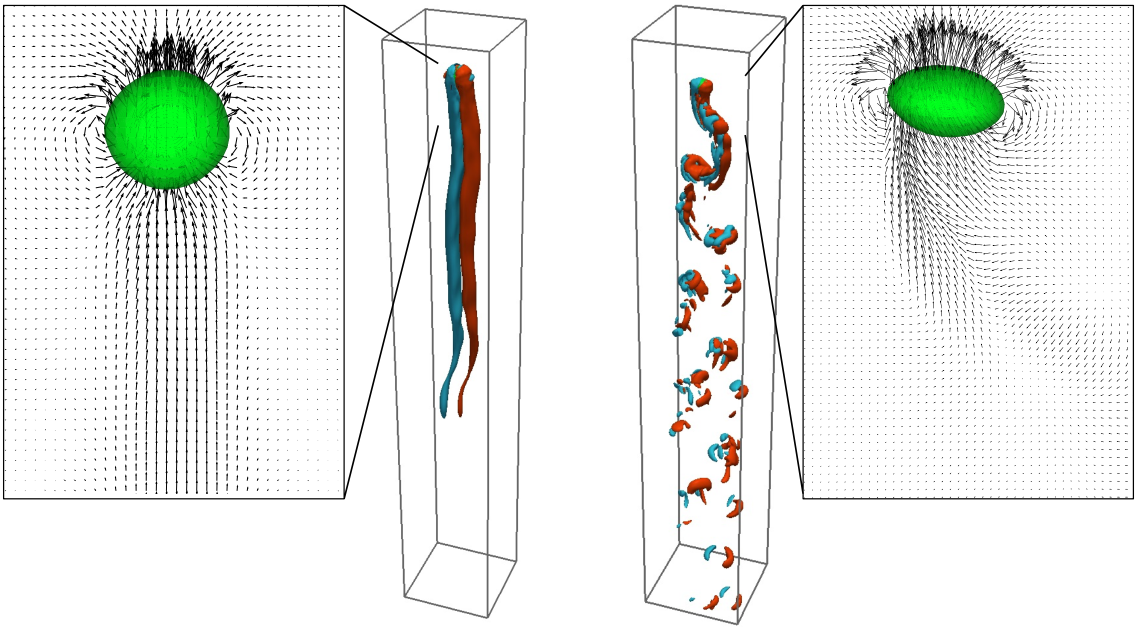

Figure 3.9: Velocity field slice and isosurfaces $\omega_x = \pm 30$ of the streamwise vorticity for two different bubble diameters, left side: D =0.8mm, right side: D =3.5mm.

the numerical point of view simulations of air bubbles in water are very difficult since the density ratio of the fluids is about 1/1000. Using our implementation we were able to solve efficiently systems with these parameters. Even when it was demonstrated that the simulations can reproduce the qualitative behavior of the path of the bubbles, it is necessary to validate the code in quantitative form. Then, we tried to compare the path of the bubbles calculated with the numerical code and the experiments reported by Veldhuis et al. (2008). In Table 3.2, this comparison is described. Experiments for five different bubble diameters were done by Veldhuis et al. (2008) and we computed the same bubble sizes, to compare the average Reynolds number of the bubbles.

As can be appreciated from Table 3.2, the numerical results are in quantitative agreement

D (mm)	Re_{exp}	Re_{calc}	$error$ %
3	899	844	6.11
3.4	973	912	6.16
3.6	1018	946	7.07
4.0	1096	1029	6.11
4.5	1162	1121	3.57

Table 3.2: Comparison of the bubble velocity computed and experimental data Veldhuis et al. (2008).

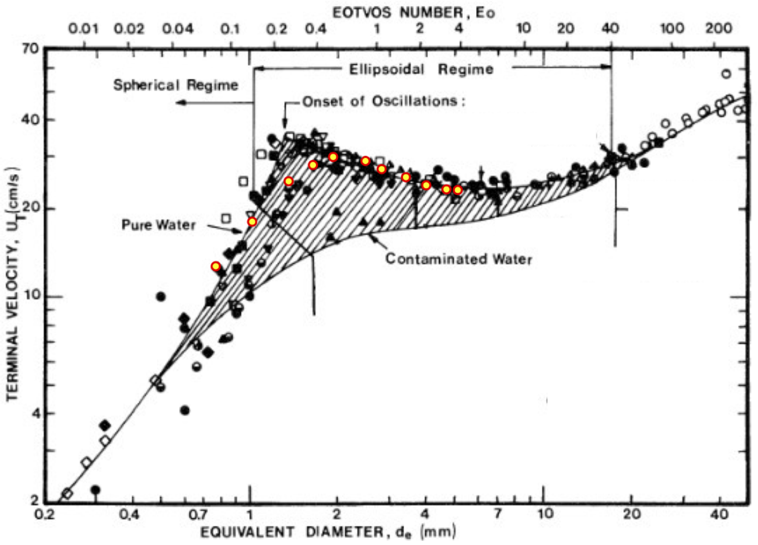

Figure 3.10: Terminal velocity of air bubbles in water, the yellow points are the results of our numerical simulations.

with the experimental data, the maximum error in the Reynolds number calculated with our code was about 7 %.

In order to continue the validation of our numerical code and knowing the importance of the experimental results given by Clift et al. (1978), the vertical velocity of the bubble resulting from our simulations was compared with the compendium of such experiments condensed in Figure 3.10 . The curve drawn with a solid line represents an empirical model proposed for the terminal velocity of bubbles and the scattered points are experiments, the red dots represent our simulations and as can be observed, there is a good quantitative comparison between the experimental points and our numerical results. In Table 3.3, the Reynolds numbers and terminal velocities for the simulations plotted in Figure 3.10 are shown. The terminal velocity as a function of equivalent diameter has not a monotonic behavior; for small bubbles when they rise in straight path, the terminal velocity is linearly proportional to the equivalent diameter. However, when the size of the air bubble exceeds certain value the terminal velocity decrease as the bubble diameter increase, this coincides with the bubble diameter in which the path instability appears and the bubble wake starts to shed vortices. As it can be seen in Figure 3.10, the numerical simulations reproduced this behavior although the maximum terminal velocity has an offset to the right. The main reason of the difference between our numerical simulations and the experimental data might be the boundary conditions of the lateral walls that can affect the dynamics of the bubbles. Also the small sub estimation of the terminal velocity can be caused by the same reason. To avoid this effect a larger computational domain must be used in the simulations, but, it would require more computer memory which was not available during the project.

D (mm)	V_T (cm/s)	Re_T
0.8	13.06	116
1.0	19.12	212
1.2	22.36	298
1.5	26.41	440
2.0	28.07	624
2.5	27.07	752
3.0	25.32	844
3.4	24.18	912
3.5	23.68	921
3.6	23.65	946
4.0	23.15	1029
4.5	22.41	1121

Table 3.3: Comparison of the bubble velocity computed and experimental data Clift et al. (1978).

3.4.3 Simulations of multiple bubbles

The numerical implementation of the front-tracking method in three dimensions was extended in order to simulate multiple bubbles ascending in a viscous fluid. The main idea is to have a computational tool to study the interactions of bubbles at different flow conditions. In such implementation the bubbles are initialized one by one at the bottom of the column of fluid with certain frequency trying to emulate the injection process of multiple bubbles. At the onset of the simulation one bubble is created and this first bubble motion is similar to that described in the previous subsection for individual bubbles, however, after some time, another bubble is generated at the same initial position of the first bubble. The bubbles evolve as a chain and the dynamics of such arrangement and the flow around the bubbles depends on the dimensionless parameters as the Reynolds, Archimedes and Eötvos numbers, and also on the number of bubbles and frequency of the injection.

We present the results of the simulation of a collection of eight bubbles of air in water of 1mm in diameter, released with a frequency of 40 Hz. The Reynolds number calculated for a single bubble with these properties is 212, and the trajectory is linear in the entire domain. In contrast, the behavior of a chain of bubbles is quite different. In Figure 3.11 the trajectories and the vertical velocities of the bubbles are plotted, and as can be observed, the first bubble (purple curve) follows a mostly rectilinear path as occurs for the single bubble case, which is obvious because the first bubble does not interact with the wakes of any other bubble and its dynamics is not altered. However, the first bubble produces low pressure zones in its wake and the disturbances last until the vorticity is dissipated. When the second bubble is injected those low pressure zones have strong influence on its dynamics and the second bubble follows initially an straight path but in a certain place its path changes dramatically; the vorticity produced by the wake of the first bubble generate a lateral motion of the second bubble, as is observed in Figure 3.11. Once the bubble is far from the wake of the first bubble the path becomes rectilinear again during its ascension. An interesting feature of this flow is that the path of all bubbles changes at the same spot, but each bubble moves in a different direction. The explanation of this phenomenon can be given in the following terms: the vortices behind the bubbles interact with the bubbles and depending on the strength be the motion of the bubbles can altered or not. The interaction between multiple bubbles is extremely complex and is far from being fully characterized.

The vertical velocity of each bubble was calculated as a function of time and in the right side of Figure 3.11 the curves are shown. For the case of the first bubble again, the velocity behaves as in the single bubble motion; after an initial period of acceleration the velocity of the bubble reaches a constant value known as terminal velocity. For the case of the other bubbles, an over-acceleration can be observed before they reach the terminal velocities due to the low pressure zones generated in the wakes of the preceding bubbles. It is clear that the dynamics of the flow are dominated by the interactions between the bubbles and their wakes and then, it is crucial to determine the structures behind the bubbles as a function of the dimensionless numbers, the number of bubbles and the frequency of the injection. For the simulation presented above, the flow around the bubbles is visualized using vorticity isosurfaces and a snapshot of the flow is plotted in Figure 3.12. As it was commented, the bubbles follow the same path like a chain, but in certain zone the trajectory of the bubbles diverges and each one follows its own rectilinear motion. The flow generated behind each bubble consists of two elongated vortices very similar to the vortices generated at moderate Reynolds numbers around and behind a rigid sphere.

If the size of the bubbles is increased (larger Reynolds number), it is well established that in the case of a single bubble, the path of the bubble changes to a helical motion. This qualitative change in the pattern was well reproduced by our code when the simulations for single bubbles were carried out. We performed the simulation of sixteen bubbles of air in water of 3.6 mm in diameter; the bubbles are injected with a frequency of 20 Hz, the Reynolds number calculated for a single bubble flow is about 946 where the simulation for a single bubble featured a helical motion. In the simulation of sixteen bubbles, the interactions between the wakes and the bubbles are more complex. In the left side of Figure 3.13 the trajectories of the first eight bubbles are shown, the natural path of the bubbles is helical, unlike the simulations of smaller bubbles. In this case the general helical motion of the bubbles is not changed; this is because larger bubbles have more inertia and the vortices generated behind the bubbles are not sufficiently strong to change the path of the bubbles in a qualitative way. However, the disturbances in the motion of the bubbles can be appreciated in the rise velocities. In the right side of Figure 3.13, the vertical velocities of the bubbles are presented. Again, the first bubble follows its natural path and then its vertical velocity is quasi-periodic around an average value after an initial acceleration (purple curve), but the other bubbles rise with velocities with many fluctuations that are promoted by the interactions between the bubbles and the wakes generated by other bubbles. To visualize the flow around the bubbles we used again isosurfaces of one component of the vorticity. In Figure 3.14 a snapshot of the flow is

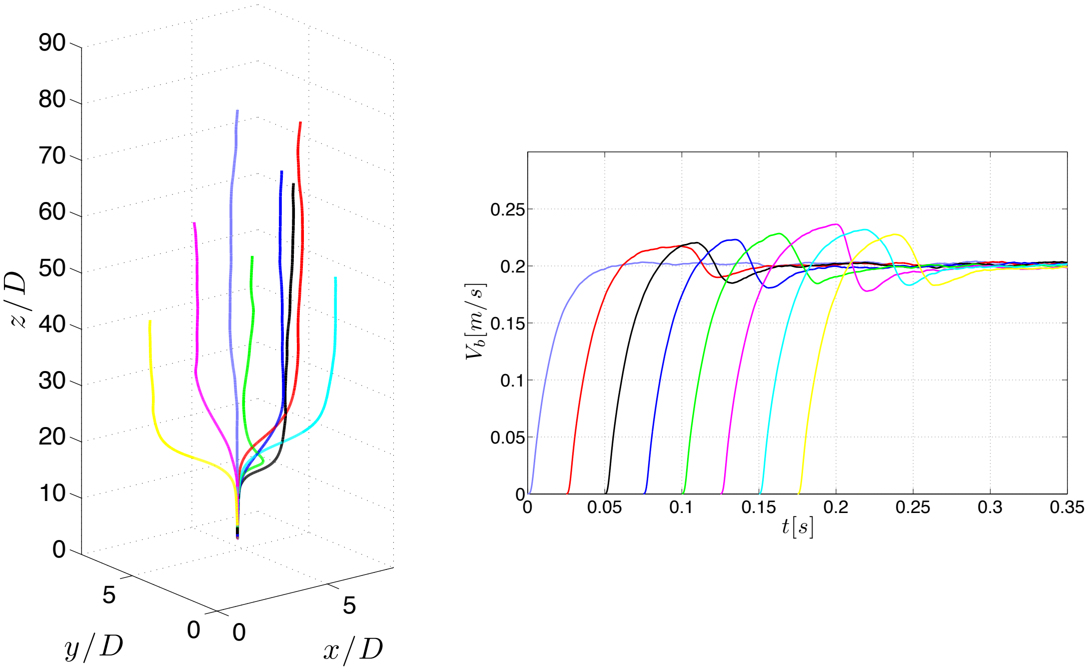

Figure 3.11: Trajectories and vertical velocities of eight bubbles of air in water of 1mm of diameter ($Eo = 0.134$, $Ar = 110$ and $Re = 212$).

presented and it is clear that it is more complex than in the case of moderate Reynolds numbers; vortex shedding appears in the wakes of the bubbles and the vortices join each other forming other structures more difficult to identify.

The interactions of multiple bubbles in this range of Reynolds numbers are more much complex, the characterization of the dynamics is very complicated to understand and many simplifications are done when engineering models are applied to bubbly flows. With direct numerical simulations as the developed in this project, we can find general aspects to include them in the engineering models; however, systematic simulations and post-processing must be done in order to characterize these flows. For example, if the purpose of the injection of the bubbles is to mix the continuous phase, from the results of the direct numerical simulations, it seems that injecting large bubbles is much more efficient than small bubbles, since the wakes generated by large bubbles when the vortex shedding appears interact in a larger zone of the column than the wakes produced by small bubbles that follow straight paths.

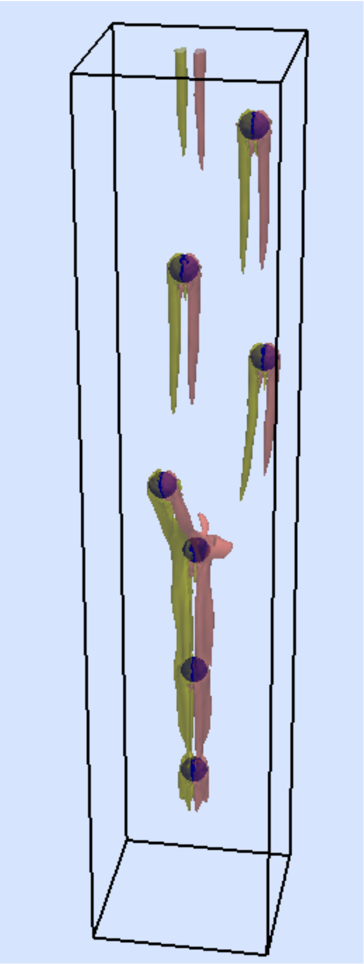

Figure 3.12: Isosurfaces $\omega_x = \pm 50$ of the streamwise vorticity of eight bubbles of air in water of 1mm of diameter.

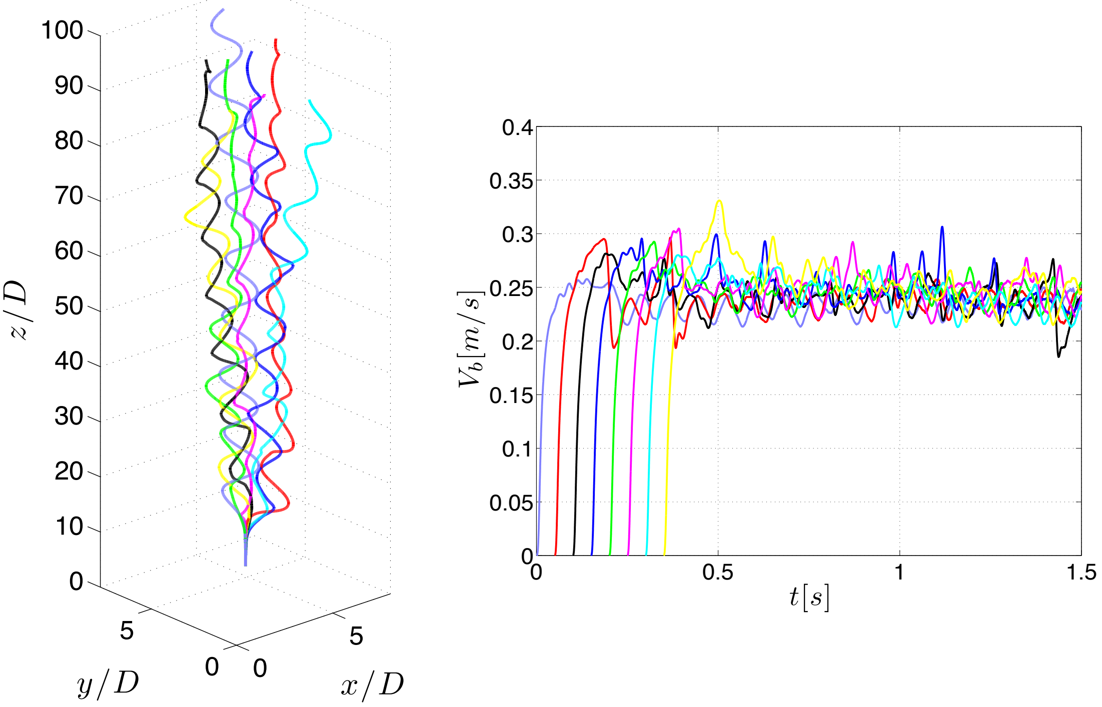

Figure 3.13: Trajectories and vertical velocities of eight bubbles of air in water of 3.6mm of diameter ($Eo = 1.74$, $Ar = 751$ and $Re = 946$).

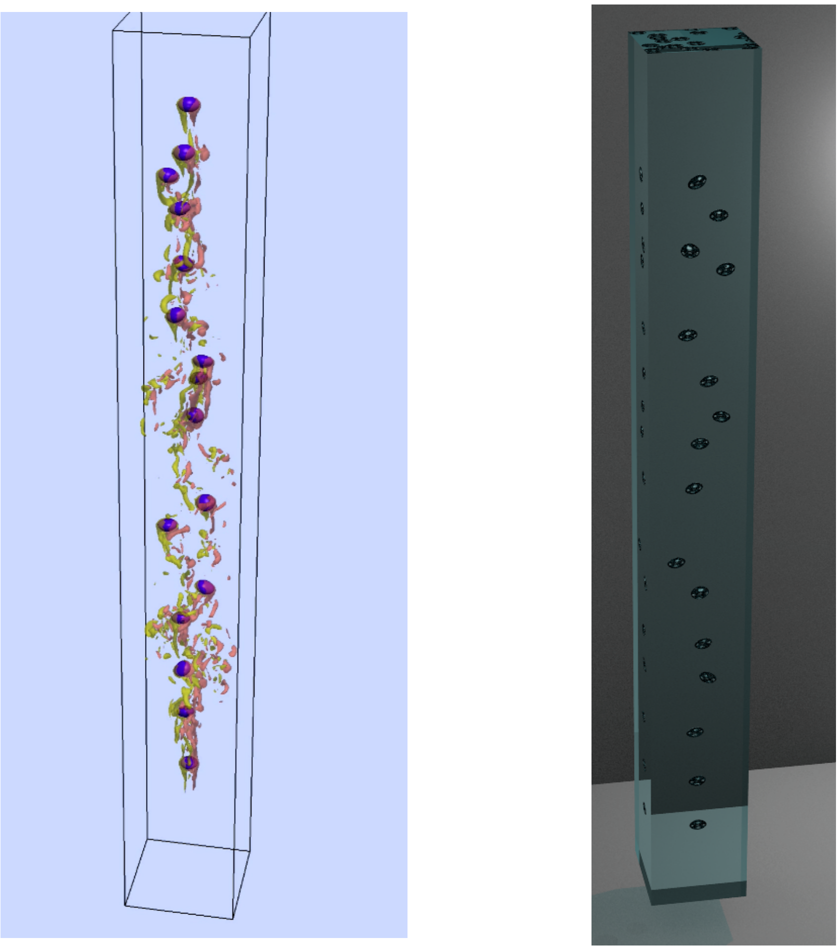

Figure 3.14: Left side: Isosurfaces $\omega_x = \pm 50$ of the streamwise vorticity of sixteen bubbles of air in water of 3.6mm of diameter. Right side: Snapshot of the sixteen bubbles flow rendered with BLENDER.

Chapter 4

Numerical study of the flow and heat transfer of bubbly flows in inclined channels[1]

4.1 Background

The study of multiphase systems has a great relevance for many industrial and natural processes. In many cases the multiphase processes involve not only fluid flow but other mechanisms, such as heat transfer, mass transfer and chemical reactions, as well. Computations of the large-scale motion of bubbly flows are usually done using averaged models (see for instance Drew & Passman (1999), Chahed et al. (2003), Troshko & Hassan (2001) and Zhang et al. (2006)), which require closure terms to account for the effect of the unresolved fluid motion. The closures are usually based on experimental results, but recently direct numerical simulations (DNS) have emerged as a powerful way to examine the dynamics of the small-scale motion and how the small-scales interact with the larger scales. DNS have, in particular, been used to examine bubbly flows in channels. The dynamics of several bubbles in a laminar flow was examined in Bunner & Tryggvason (2002*a*), Bunner & Tryggvason (2002*b*) and in Lu et al. (2005) Lu & Tryggvason (2006) and Lu & Tryggvason (2008), the study was extended to turbulent flows. The results have shed considerable light on how the dynamics depends on the size of the bubbles and the flow direction. Industrial processes often involve heat transfer in bubbly flows and since the bubbles change the flow in significant ways, compared with single-phase flows, the heat transfer is also modified. It is, in particular, known that the presence of bubbles can enhance the heat transfer. Direct numerical simulations of heat transfer in turbulent single phase channel flow were reported by Kawamura et al. (1998) and Kozuka et al. (2009), but direct numerical simulations of heat transfer in bubbly flows are more recent. Studies of the modification of heat transfer in a quiescent fluid due to rising bubbles, (Deen et al. (2006) and Deen & Kuipers (2013)), have shown that the local heat transfer coefficient between the liquid and a hot wall at constant temperature has a maximum in the vicinity of the bubbles and this maximum increases when the bubbles coalesce. The heat transfer in bubbly flows in a turbulent channel was studied in Dabiri & Tryggvason (2015), using the same front tracking/finite volume method used here. The results of several simulations for vertical turbulent channel flows with bubbles were reported and

---

[1] This chapter is based on Piedra, Lu, Ramos & Tryggvason (2015)

a significant increase in the average heat transfer coefficient due to the presence of the bubbles was found, specially when the bubbles retain a spherical shape and accumulate near the walls. The heat transfer in bubbly flows has also been studied experimentally. In general, experimental results show that the heat transfer is improved by the presence of a dispersed phase. For the case of laminar natural convection, it has been found that the injection of sub-milimeter bubbles enhances the heat transfer due to mixing and advection effects (Kitagawa & Murai (2013)). This effect is maximized when bubbles impact and slide along hot walls (Donnelly et al. (2009)). More recently, experiments of bubble flows in vertical and inclined channels have shown that, for high void fraction of gas and low friction Reynolds numbers the effect on the heat transfer coefficient and the wall shear stress are strongly dependent on the inclination angle (Kashinsky et al. (2013) and Kashinsky et al. (2014)). In the present work, the dependency of the flow and the heat transfer in low void fraction bubbly flows on the inclination angle of a channel are studied using direct numerical simulations. It is important to highlight that the results presented in this section were computed modifying the finite volume/front-tracking code from the group of the University of Notre Dame and not from the code developed in our group of UNAM.

4.2 Problem setup and numerical implementation of the heat transfer equation

The computational domain is an inclined channel, bounded by two parallel plates, shown in Figure 4.1. The size of the domain is $\pi \times 2 \times \pi/2$ in the streamwise, wall-normal and spanwise direction, respectively. The flow is driven by imposing a constant pressure gradient in the x direction and the gravity acceleration depends on the inclination angle of the channel (γ). For the horizontal channel, gravity acts in the y direction and in the x direction for the vertical channel. Periodic boundary conditions are imposed in the streamwise and spanwise directions and no-slip boundary conditions are enforced at the walls.

The numerical simulations were carried out using a finite volume/front-tracking method described in the first chapter. Also, the energy equation is solved using the same strategy as in Dabiri & Tryggvason (2015) to account for the periodic boundary conditions in the streamwise direction. The energy equation, in terms of the temperature for the whole domain, can be written as:

$$\rho c_p \left(\frac{\partial T}{\partial t} + \nabla \cdot (\mathbf{u}T) \right) = \nabla \cdot (k \nabla T), \tag{4.1}$$

where c_p and k are the specific heat and conductivity, respectively. In this case the bulk temperature $\langle T_m \rangle$, increases linearly with the streamwise coordinate due to the uniform

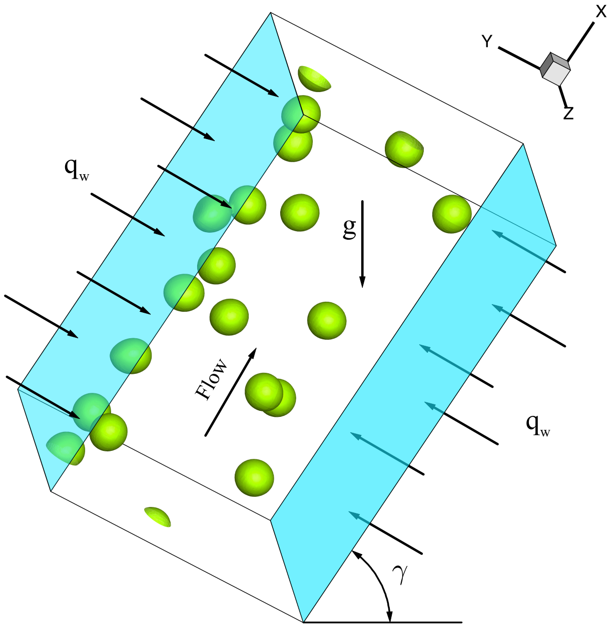

Figure 4.1: Sketch of the problem configuration.

heat flux at the walls (Kawamura et al. (1998)). Thus, the instantaneous temperature is split in two parts:

$$T = \frac{d\langle T_m \rangle}{dx_1} x_1 - \theta, \tag{4.2}$$

where, θ is the transformed temperature in the channel and the streamwise gradient of the bulk temperature is given by:

$$\frac{d\langle T_m \rangle}{dx_1} = \frac{2q_w}{\int_0^{2\delta} \langle \rho c_p u_1 \rangle dy}. \tag{4.3}$$

Substituting equation (4.2) into (4.1), the energy equation written for the transformed temperature θ is:

$$\frac{\partial \theta}{\partial t} + u_j \frac{\partial \theta}{\partial x_j} - u_1 \frac{d\langle T_m \rangle}{dx_1} = \frac{1}{\rho c_p} \frac{\partial}{\partial x_j} \left(k \frac{\partial \theta}{\partial x_j} - k \frac{d\langle T_m \rangle}{dx_1} \delta_j \right). \tag{4.4}$$

This equation is solved along with the mass and momentum conservation equations, described in chapter 1.

The simulations are done using computational units, but the flow is determined by the characteristics dimensionless parameters described below. The fluid density is $\rho_l = 1$ and the kinematic viscosity is $\nu_l = 0.000333$. The density of the bubbles was one-fortieth the density of the liquid, and the kinematic viscosity of the bubbles was forty times that

of the liquid. The bubble diameter is 0.25, the surface tension coefficient is $\sigma = 0.01$ and the gravity acceleration is $g = 0.05$. For the simulations reported the dimensionless parameters are $M = 5.93 \times 10^{-10}$ and $Eo = 0.3125$. Two sets of simulations were carried out for two different pressure gradients in the channel. For all the simulations we define a friction Reynolds number as $\mathrm{Re}_\tau = hu_\tau/\nu_l$, where h is the half-width of the channel, the friction velocity is $u_\tau = \sqrt{(\tau_w/\rho_l)}$, and τ_w is the averaged wall shear stress. For the first set of simulations the friction Reynolds number is $Re_\tau = 150$ and the bulk Reynolds number based on the bulk velocity, $U_b = 0.7638$, of the single phase flow and the width of the channel is $Re = 4582$. For the second set of simulations the friction Reynolds number is $Re_\tau = 49$ and the bulk Reynolds number is $Re = 1600$. For the first set the initial flow field is turbulent but for the second set it is laminar. The flow is driven by a specified pressure gradient, which is modified as the inclination of channel is changed in such a way that the imposed pressure gradient and the average weight of the mixture are constant. Thus, if the flow structure remained the same, the inclination angle would have no influence on the flow rate. In reality, however, the buoyancy changes the flow structure in two ways as the inclination angle changes. First of all, buoyancy drives the bubbles to the top of the horizontal channel and this effect decreases as the inclination angle is increased. Secondly, buoyancy causes the bubbles to move faster than the liquid in the vertical channel, but the slip velocity decreases as the inclination angle is decreased.
To characterize the heat transfer we used the Prandtl number ($Pr = c_p\mu_l/k$) and the Nusselt number, defined by:

$$Nu = \frac{2h}{k} = \frac{2PrRe_\tau}{\langle\theta_m\rangle - \langle\theta_w\rangle}. \tag{4.5}$$

Here h is the heat transfer coefficient, $\langle\theta_m\rangle$ is the bulk temperature and $\langle\theta_w\rangle$ is the average wall temperature. Since we expect that bubbles will accumulate near the top wall, because the direction of the gravity force, the Nusselt number was calculated separately for each wall.

The equations were discretized using a mesh with 192 × 160 × 96 grid points that are uniformly spaced in the x and z directions but non-uniformly in the y direction with Δy ranging from 0.0062 to 0.0172. This is similar to the discretization used in Lu & Tryggvason (2006). The initial velocity for the simulations where the flow is turbulent was taken from simulations of single phase turbulent flow in a channel, solved with a spectral method (Gibson (2014)) with 128 × 65 × 64 modes, and interpolated to the grid used for the bubbly flows.

4.3 Results

We have examined the turbulent channel flow for several different inclinations. The parameters for both cases are listed in Table 4.1. The cases reported in this paper are for inclination angles of 0°, 30°, 60° and 90°, with respect to the horizontal coordinate.

Average Void fraction	3%
Friction Reynolds number (Re_τ)	150, 49
Bulk Reynolds number (Re)	4582, 1600
Kinematic viscosity ratio(ν_b/ν_l)	40
Density ratio (ρ_l/ρ_b)	40
Prandtl number (Pr)	2

Table 4.1: Flow conditions for the simulations.

4.3.1 Simulations of flow and heat transfer in a turbulent channel

For the first set of simulations, in which Re_τ=150, the temperature field in a plane cutting through the channel and the bubble distributions are presented for three cases ($\gamma = 0°, 60°, 90°$) in Figure 4.2, after the flow has reached an approximate average steady state. The bubbles remain spherical and for the horizontal and inclined channels they are concentrated near the top wall. For the vertical channel the bubbles form one layer near each wall. The isocontours of the streamwise velocity are also plotted in the same plane as the temperature field and it is clear that the flow is perturbed near the top wall due to the presence of the bubbles.

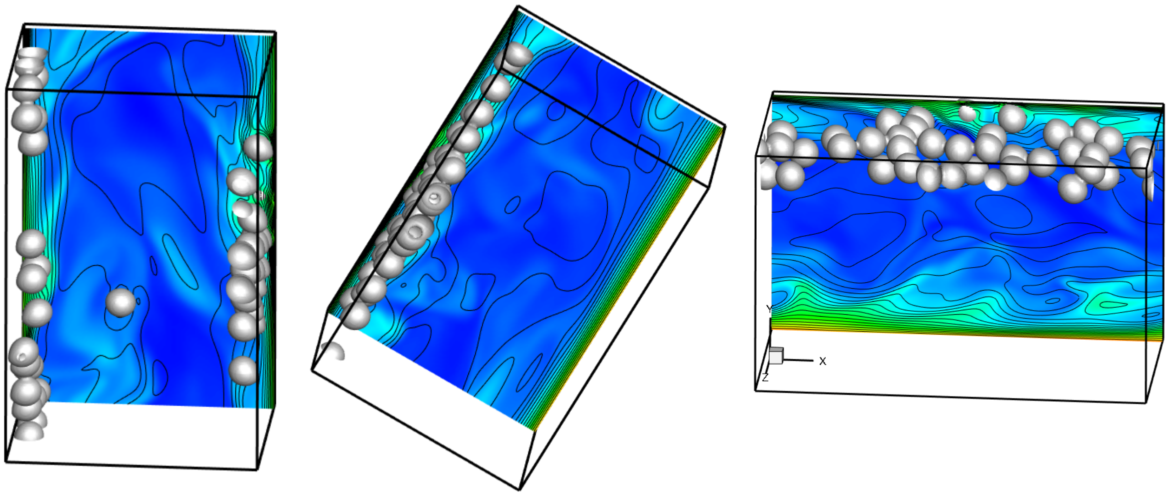

Figure 4.2: The isocontours of a plane of the temperature field, the isolines of the streamwise velocity and the bubble distribution into the channel with Re_τ=150, left: $\gamma = 90°$, center: $\gamma = 60°$, right: $\gamma = 0°$.

In order to guarrantee that the flow is at steady state, the average wall shear is plotted as a function of the non-dimensional time ($t^* = tg^{\frac{1}{2}}/D^{\frac{1}{2}}$) in Figure 4.3. At steady state the averaged theoretical value of the wall shear is equal to the sum of the constant pressure gradient and the weight of the mixture. For the simulations reported here, this value is 0.0025 and is shown by a horizontal line. It can be seen that the wall shear obtained from the simulations matches well with the theoretical value for $\gamma = 0°$ and $\gamma = 30°$ after time 500 or so. For $\gamma = 60°$ and $\gamma = 90°$, it takes longer to reach the steady state.

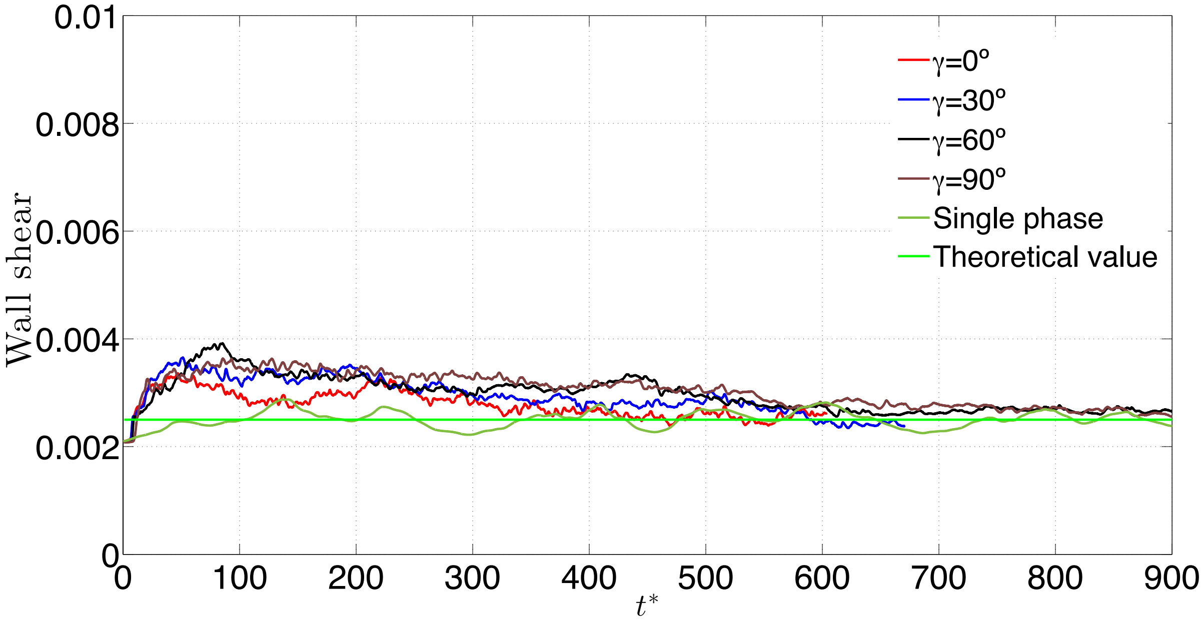

Figure 4.3: Averaged wall shear as a function of time for different inclinations of the channel at steady state, Re_τ=150.

The dynamics of the bubbles is shown in Figure 4.4, where the y coordinates of the bubble centroids are plotted as a function of time. For γ=0° the bubbles migrate rapidly to the wall and form bubble layers, although bubble-bubble interactions also result in some bubbles moving slightly away from the wall. Almost the same behavior is found for γ=60°, but the time that the bubbles take to migrate to the wall is longer, since the gravity force is weaker. However, in this case, as can be seen in Figure 4.2, the bubbles hug the wall as a mono-layer. This is also seen in the middle panel of the left hand side of Figure 4.4, where the trajectories are almost straight lines near the top wall. For the vertical channel (γ=90°) it is well-known that the bubbles migrate to both walls due to the lift force and two wall-layers are formed (Dabiri & Tryggvason (2015)).

In the right frame of Figure 4.4 the void fraction is plotted for the different simulations. For the vertical channel the void fraction peak is similar at both walls. In the other cases, as we incline the channel, the maximum of the void fraction at the top wall increases and the bubbles are constrained to move along the wall due to the lift force.

The averaged velocity profile and the Reynolds stress are plotted in Figure 4.5, for the different simulations, and compared with the single phase flow. The liquid velocities for all the bubbly flows are smaller than the velocity without bubbles, and unlike the single phase flow the profiles are not symmetric for the inclined channels, since the velocity

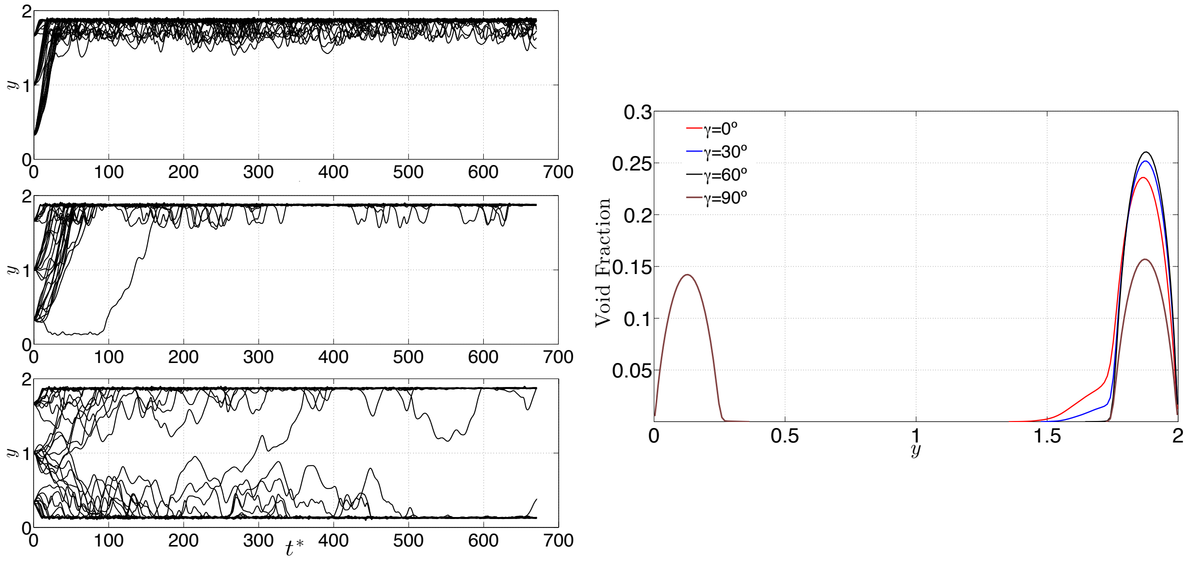

Figure 4.4: Left: Trajectories of the the bubbles in the y-coordinate, a) γ=0°, b) γ=60°, c) γ=90°. Right: Void fraction across the channel for different inclination angles for the set of simulations with Re_τ=150.

decreases near the wall where the bubbles are concentrated. The velocity near the top wall is minimum for the horizontal channel but increases rapidly outside the bubble layer. As we incline the channel, the velocity increases near the top wall as the buoyancy in the streamwise direction becomes larger, but the averaged velocity in the core region decreases due to the mixture weight.

The off-diagonal components of the Reynolds stresses, non-dimensionalized with the square of the friction velocity, are plotted in the right frame of Figure 4.5, as functions of the wall-normal coordinate. For the single phase flow we find the classical linear behavior and for the horizontal channel the Reynolds stress is very similar near the bottom wall. However, the maximum value close to the top wall is larger than in single phase flow. The extra turbulent stress in this part of the channel can be attributed to increased mixing due to the presence of the bubbles and the fact that they do not form a single layer sliding smoothly along the wall.

To analyze the effect of the bubbles on the heat transfer, the Nusselt number at the top wall is shown in Figure 4.6, for the different inclination angles. It is clear that the Nusselt number does not change much as the channel is inclined, although for completely vertical channel it decreases slightly. This can be explained by the fact that the bubbles go to both walls and the void fraction at the top wall is lower than for the other cases, thus reducing the efficiency of the bubble induced mixing. Compared with the single phase flow the Nusselt number increases for all the bubbly flows by about 25 %.

The temperature profiles for the different cases are plotted in Figure 4.7, where the difference of the temperature averaged over the streamwise and spanwise directions and the top wall temperature is shown. For the bubbly flows the difference from the wall temperature

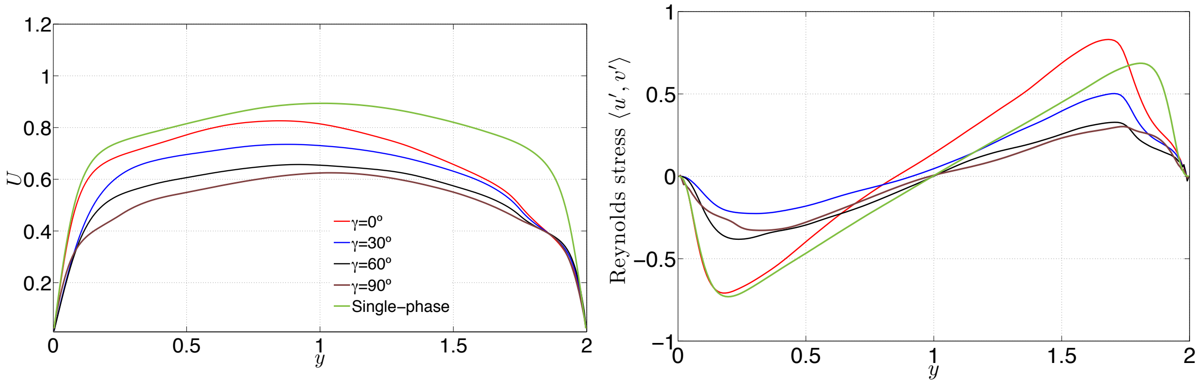

Figure 4.5: Average velocity profiles and Reynolds stresses for different angles of inclination of the channel, Re_τ=150.

is smaller near the top wall than in the single phase flow, indicating that the bubbles cause heat to be transported more efficiently from the wall to the fluid. The temperature profiles also suggest that the heat is transported most efficiently for the channel with a slope of γ=60°. This effect is explained by the fact that at this inclination angle the reduction of the velocity due to the wall friction near the top wall is less than for the horizontal channel since the lift force in the wall-normal direction stabilizes the wall-layer, resulting in a more constant convective mixing. To illustrate this effect, slices of the temperature field are plotted in Figure 4.8 for the different cases and compared with flow without bubbles. For the single phase flow it is clear that the high temperature zones are near the walls but local turbulent convection transports heat from the wall to the interior of the channel. For the inclined channels the bubbles concentrated at the top wall mix the fluid and promote an efficient heat transport in a larger region of the channel than in the single phase flow. This is specially the case when the angle of inclination is 60° and the hot zone near the top is thickest. This effect is produced near both walls for the vertical channel where the efficient mixing zones suggest that the average heat transfer coefficient along both walls is larger than for the other cases.

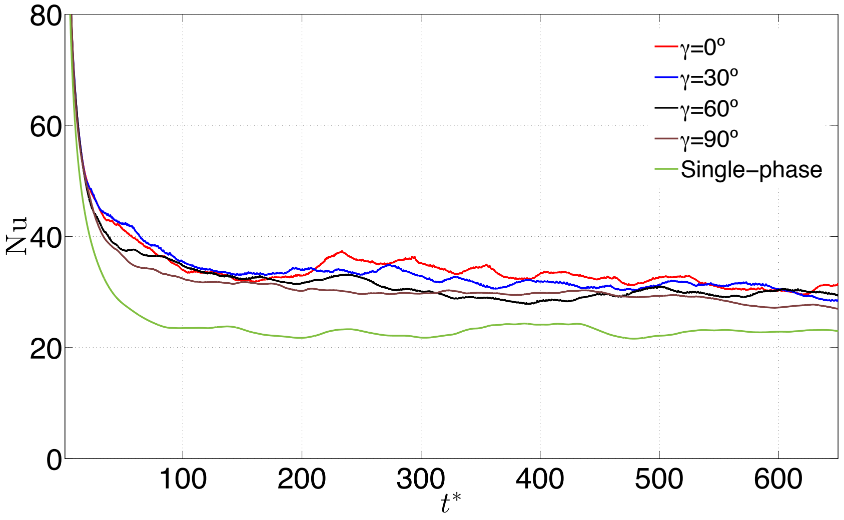

Figure 4.6: Nusselt number at the top wall versus time for the different inclinations of the channel, Re_τ=150.

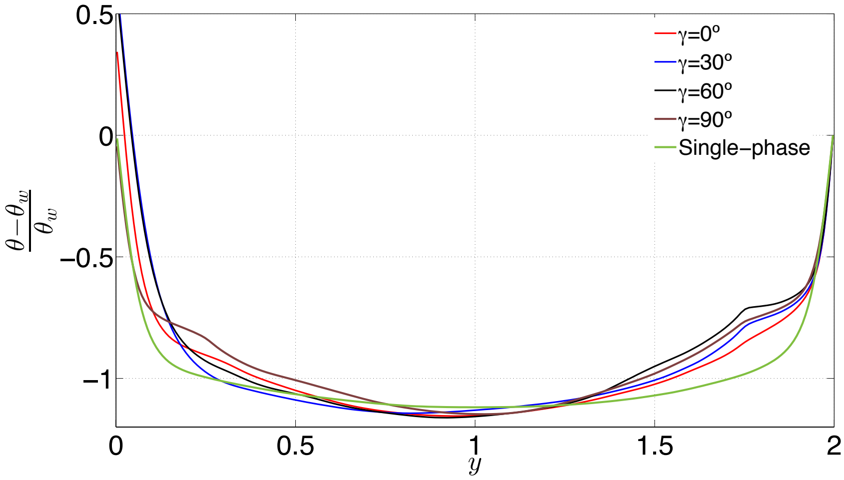

Figure 4.7: Profiles of the difference of the average temperature and the top wall temperature across the channel for different inclination angles, Re_τ=150

.

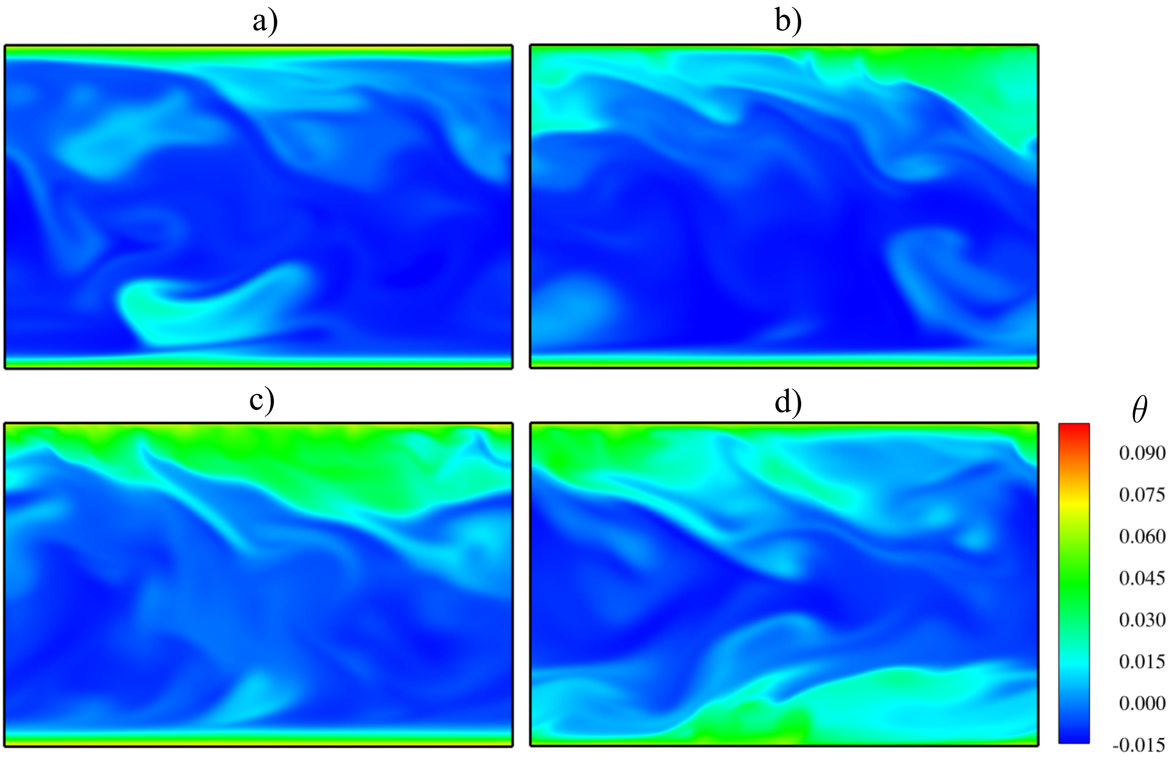

Figure 4.8: Temperature field slices for different inclination angles compared with the single phase flow, a) single phase flow in a horizontal channel, b) γ=0°, c)γ=60° and d) γ=90°, Re_τ=150.

4.3.2 Simulations of flow and heat transfer in a laminar channel

For the second set of simulations, where Re_τ=49 and the flow is laminar, the temperature fields in a plane cutting through the channel and the bubble distributions are presented in Figure 4.9 for three angles of inclination ($\gamma = 0°, 60°, 90°$). For sloping and horizontal channels it is clear that the temperature is higher at the bottom wall, since the bubbles are concentrated near the top and the convection produced by the bubbles transports the heat from the wall more efficiently. The distribution of the bubbles in the channel is very similar to the turbulent flow, but since the driving force is comparable with the buoyancy, the lift force that pushes the bubbles to the walls is much smaller. As a result, in the vertical channel the bubbles are distributed more uniformly with only a slightly larger concentration in the walls. For the sloping and horizontal channels, the bubbles migrate to the top wall due to the component of the gravity force in the wall-normal direction. In Figure 4.9, isolines of the streamwise velocity, in the same plane as the temperature field, are also plotted, and it is clear that the flow in the horizontal channel is laminar, especially in the bottom part of the channel where there are no bubbles and the isolines of the velocity are almost straight. In the top part of the channel, however, the bubbles alter the flow by creating a layer with strong velocity fluctuations that promote mixing of the fluid. The flow in the sloping channels looks similar, but in these cases the buoyancy force in the streamwise direction produces stronger fluctuations in the flow where the bubbles are packed together.

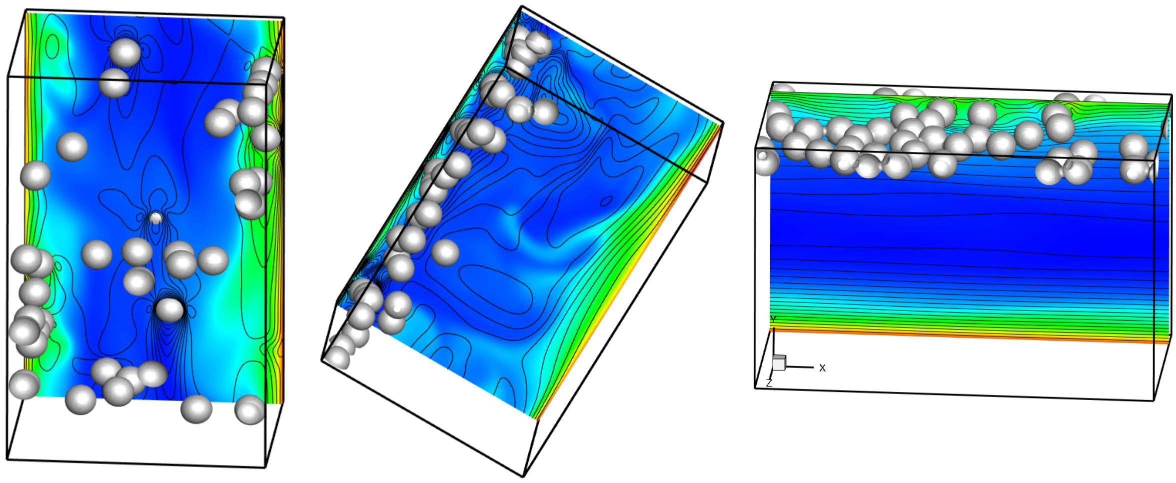

Figure 4.9: The isocontours of a plane of the temperature field, the isolines of the streamwise velocity and the bubble distribution into the channel for Re_τ=49, left: $\gamma = 90°$, center: $\gamma = 60°$, right: $\gamma = 0°$.

In Figure 4.10, the averaged velocity and void fraction profiles for the different inclination angles are shown, along with the velocity for the single phase flow. In the horizontal channel the velocity decreases near the top wall, where the void fraction is maximum. The figure shows that the redistribution of the bubbles leads to dramatic changes in the flow. For the horizontal and vertical channels the average velocity is positive but for the inclined channels where the bubbles are forced to the top wall, the liquid is sufficiently heavy so that it flows backward. While this effect is due to the particular ratio of mixture weight and pressure gradient used here, we include this case to show how non-trivial the effect of the inclination angle can be. The velocity for the sloping channels becomes negative in the zones without presence of bubbles since the total pressure gradient (the sum of the imposed pressure gradient and the weight of the mixture) is smaller than the weight of the liquid phase. However, this effect was not observed for the vertical channel since the bubbles in this case are distributed more uniformly and the weight of the fluids in the entire channel is always compensated with the total pressure gradient. Unlike in the turbulent flows, the void fraction of the bubbles decreases near the top walls as the inclination of the channel is increased (see left side of Figure 4.10). This is due to the lift force not being strong enough to keep the bubbles in a layer near the top wall as for the turbulent channel.

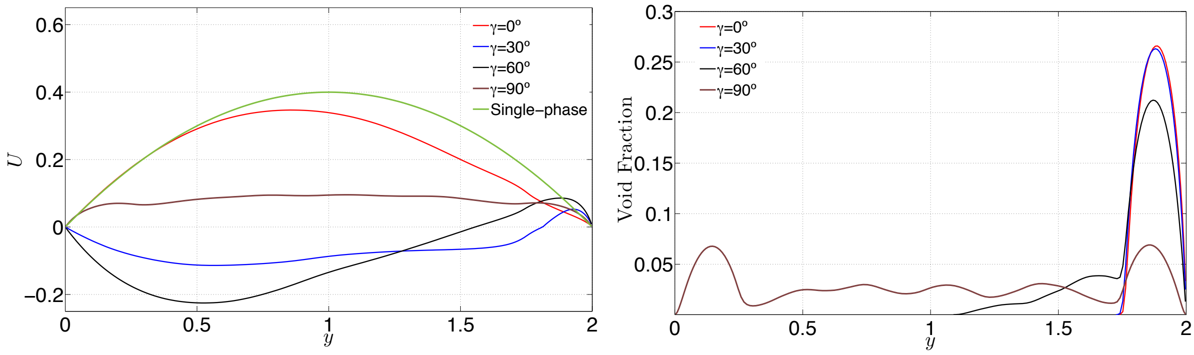

Figure 4.10: Velocity and void fraction profiles across the channel for different inclination angles, Re_τ=49.

The global effect of the inclination angle on the heat transfer in the channels was analyzed by computing the Nusselt number. In Figure 4.11, the evolution of the Nusselt number for the top wall is plotted for the single phase and bubbly flows for the different inclination angles. Once the flow reaches a steady state, the Nusselt number remains approximately constant, as for the turbulent flows. For all cases the Nusselt number in the bubbly flows inscreases compared to the single phase flow. However, in contrast to the turbulent flows where the Nusselt number is almost independent of the inclination angle, for laminar flows, it was found that the Nusselt number for sloping channels is considerably larger than for the horizontal and vertical channels. For the channel inclined 60° the Nusselt number increases about 3.7 times with respect to the single phase flow.

The temperature profiles for the laminar flows are presented in Figure 4.12, in the same way as for the first set of simulations. It can be seen, that the average temperature profile for those flows is very dependent on the inclination angle. When the channel is inclined to 30° and 60°, the temperature decreases, but for the vertical channel the temperature is larger than in the sloping channels but still lower than in the horizontal channel.
In order to illustrate better the effect of the inclination angle on the heat transfer, slices

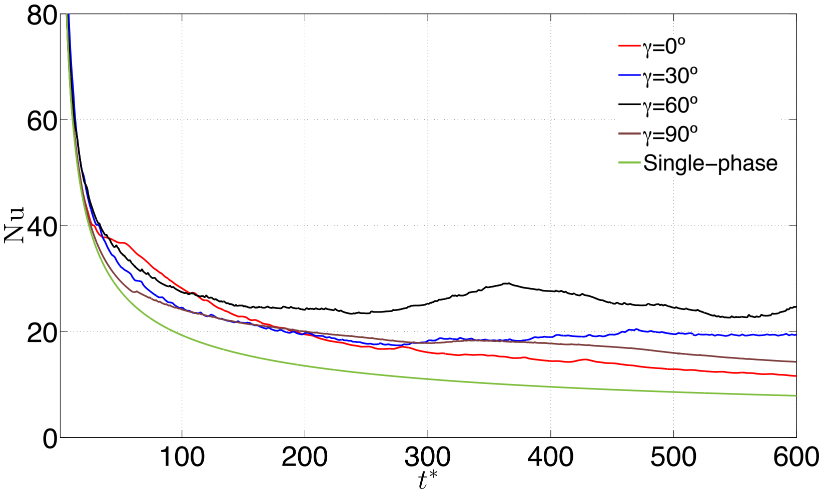

Figure 4.11: Nusselt number at the top wall versus time for the different inclinations of the channel, Re_τ=49.

of the temperature field are shown in Figure 4.13 (as Figure 4.8 shows for the turbulent flows). In the single phase flow the heat accumulates near the walls, and for the bubbly flow in the horizontal channel it is clear that the heat is transported from the top wall to the fluid due to convection flow by the bubbles. However, for the channel inclined 60° this effect is amplified by the buoyancy force in the streamwise direction and the mixing is much better than in the other cases. Finally in the vertical channel, the lower concentration of bubbles near the walls produces mixing that decreases the heat transfer near the walls.

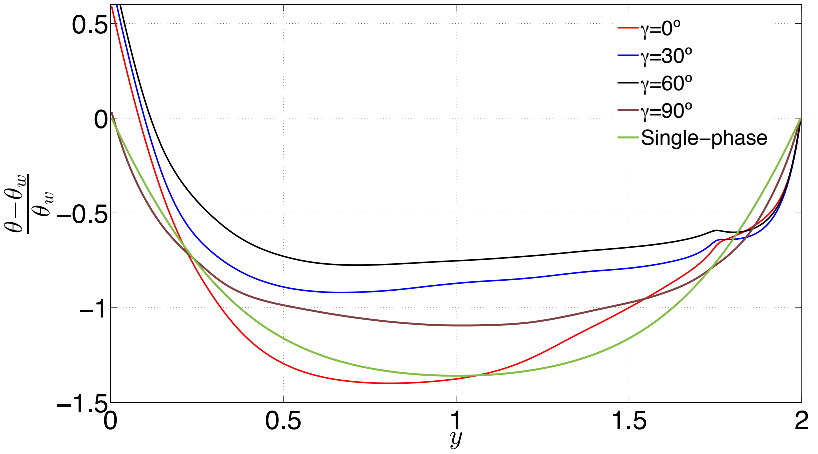

Figure 4.12: Profiles of the difference of the average temperature and the top wall temperature across the channel for different inclination angles, Re_τ=49.

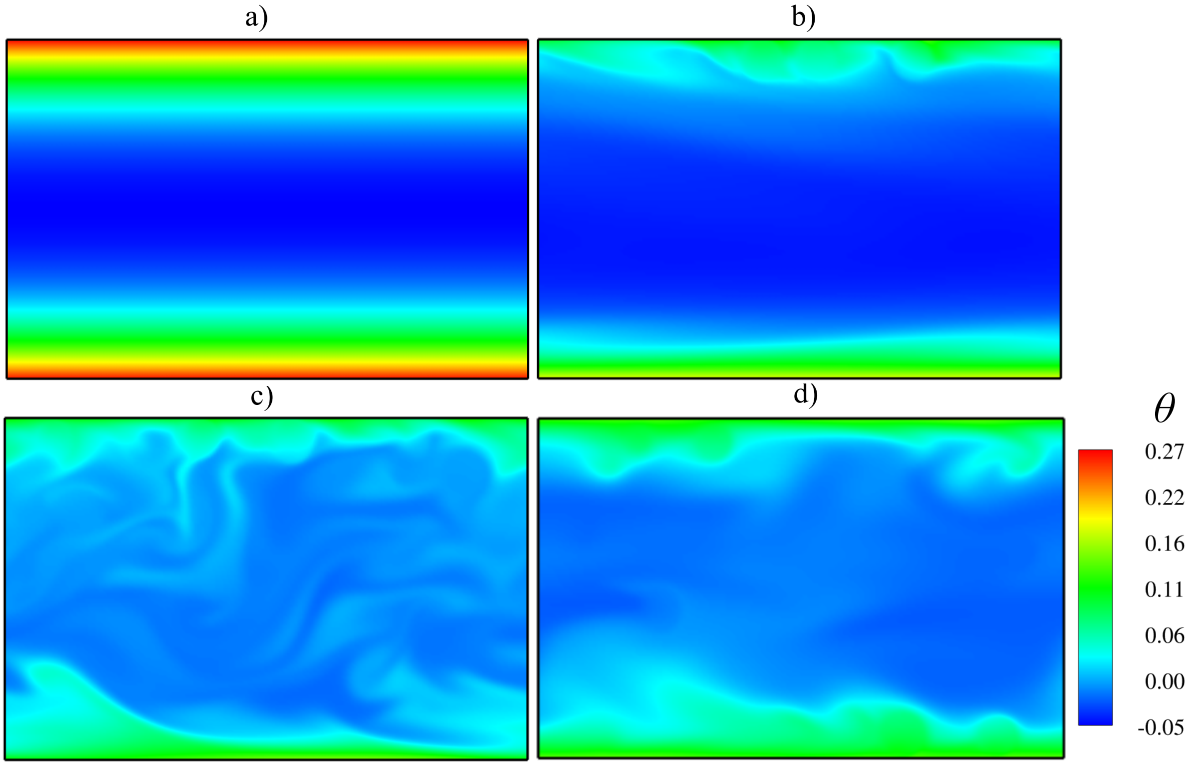

Figure 4.13: The temperature field in the center plane of the channel for different inclination angles, compared with single phase flow, a) single phase flow in a horizontal channel, b) γ=0°, c)γ=60° and d) γ=90°, Re$_\tau$=49.

Chapter 5

Evaporation of droplets using the front-tracking method

5.1 Background

Heat and mass transfer phenomena in two-phase flows have been studied due to their importance in many processes. The evaporation of raindrops or fuel droplets during the combustion in engines are two examples in which mass and heat transfer appear in multiphase flows. Using the formulation developed in this project, the front-tracking method was extended to simulate the evaporation of droplets at non-isothermal conditions. It is important to emphasize that the direct numerical simulation with phase change is in its infancy and there are only few examples available in the literature. For instance, boiling flows and solidification have been studied using DNS (e.g. Esmaeeli & Tryggvason (2004*a*), Esmaeeli & Tryggvason (2004*b*) and Tryggvason et al. (2011)). Tanguy et al. (2007) developed a model to simulate the evaporation of a single droplet using the level-set method. They presented and validated simple cases where the droplet is static and the mass flux at the interface is constant, and even when they considered the case of a moving droplet, the falling velocity of the drop is considered constant. Schlottke & Weigand (2008) reported a complete model for the evaporation of droplets using the volume of fluid method, described some features of the implementation to improve the accuracy of the solution and presented the mass fraction, temperature and velocity fields of the flow around a droplet that evaporates at high Reynolds number. Safari et al. (2014), presented an evaporation model and numerical simulations using the lattice Boltzmann method to study the non-isothermal evaporation of a stationary droplet and the effects of an external flow. There are some papers in which the results DNS of the evaporation phenomenon are reported using commercial software, for instance, in the work of Banerjee (2013) and Zhao et al. (2014) , the evaporation of droplets is explored using ANSYS FLUENT, and results of velocity, mass fraction and temperature fields for different flow conditions are shown. However, in the opinion of the author of this thesis, the use of commercial software is not the best way to study in detail this kind of problems due to inaccuracy of the solution and the limitations of the numerical implementation into the software.

It is important to mention that even when there are some developments of the mass transfer in two-phase flows using the front-tracking method (Aboulhasanzadeh et al. (2012), Aboulhasanzadeh et al. (2013)), as far as the author of this thesis knows the implementation described in this chapter is the first one in which the evaporation phenomenon is completely solved using the front-tracking method. Some illustrative results of the numerical simulations are presented in order to show the capabilities of the evaporation model developed.

5.2 Evaporation model

Consider a drop immersed in an atmosphere of a mixture of the liquid vapor and a gas, the drop is pulled downwards by the effect of the gravity and evaporates as it falls (see Figure 5.1). The mass reduction in the drop is influenced by the local thermodynamics conditions which in turn are modified by the dynamics of the drop motion. The evaporation model is based on the simultaneous solution of the mass, momentum, energy and species conservation equations for incompressible fluids properly adapted to incorporate the possibility of the mass transfer at the boundary between the phases. The set of equations are defined in the whole domain including the interface. It is convenient to start with the vapor mass equation to introduce the model. The transport equation for the vapor mass fraction can be described with the equation of a single component in a multicomponent gas mixture as:

$$\frac{\partial \rho Y_v}{\partial t} + \nabla \cdot (\rho \mathbf{u} Y_v) = \nabla \cdot (\rho D_{vg} \nabla Y_v) + \dot{m}, \tag{5.1}$$

where ρ is the local density, Y_v is the mass vapor fraction, $\mathbf{u}$ is the velocity field and D_{vg} is the binary diffusion coefficient, the volumetric source of the mass vapor ($\dot{m}$) is concentrated at the interface and it can be calculated through the integration of the mass flux at the surface. The mass conservation equation must take into account the vapor mass generated by the evaporation at the interface of the two-phases. This is accomplished by inserting an expression for the velocity difference across the surface on the right hand side of the equation as follows (Tryggvason et al. 2011):

$$\nabla \cdot \mathbf{u} = -\left(\frac{1}{\rho_v} - \frac{1}{\rho_l}\right) \int_S \delta^\beta(\mathbf{x} - \mathbf{x}_f) \dot{m''} dS_f. \tag{5.2}$$

The momentum conservation equations solved for this model are unchanged as those presented in Chapter 1. Taking into account the latent heat generated by the phase change and neglecting the viscous dissipation, the energy equation can be written as:

$$\rho c_p \left(\frac{\partial T}{\partial t} + \nabla \cdot (\mathbf{u} T)\right) = \nabla \cdot (k \nabla T) + L\dot{m}, \tag{5.3}$$

where c_p and k are the specific heat and the conductivity, respectively, T is temperature and L is the latent heat of the evaporating fluid. From the jump condition at the interface for the species conservation equation it is possible to calculate the mass flux as (Schlottke & Weigand (2008)):

$$\dot{m}'' = \frac{D_{vg}\rho_g \nabla Y_v \cdot \mathbf{n}_\Gamma}{1 - Y_v^\Gamma}. \tag{5.4}$$

The vapor mass fraction depends on the saturated vapor pressure (p_v^Γ), which can be computed through the Clausius-Clapeyron relation:

$$p_v^\Gamma = p \exp\left(-\frac{Lm_v}{R}\left(\frac{1}{T^\Gamma} - \frac{1}{T^B}\right)\right), \tag{5.5}$$

then, the vapor mass fraction at the interface is given by:

$$Y_v^\Gamma = \frac{p_v^\Gamma m_v}{(p - p_v^\Gamma)m_g + p_v^\Gamma m_v}, \tag{5.6}$$

where m_v and m_g are the molar masses of vapor and gas respectively, R is the perfect gas constant, T^B is the liquid boiling temperature for the ambient pressure condition and T^Γ is the temperature at the interface.

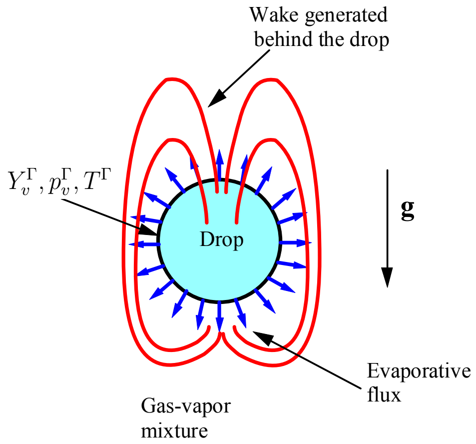

Figure 5.1: Physical model of the evaporation of a droplet.

5.3 Validation of the code: Evaporation of a planar surface

In order to validate the model developed, a simple case was solved analytically and compared with the numerical solution. The one-dimensional case in which a planar surface is evaporated was analyzed. A sketch of the physical problem is shown in Figure 5.2, The test problem consists of an open container partially filled with liquid and surrounded by a gas. Since the vapor mass fraction in the surrounding gas is less than the vapor mass fraction at the liquid-gas interface, the vapor diffuses from the interface to the gas while the evaporation occurs.

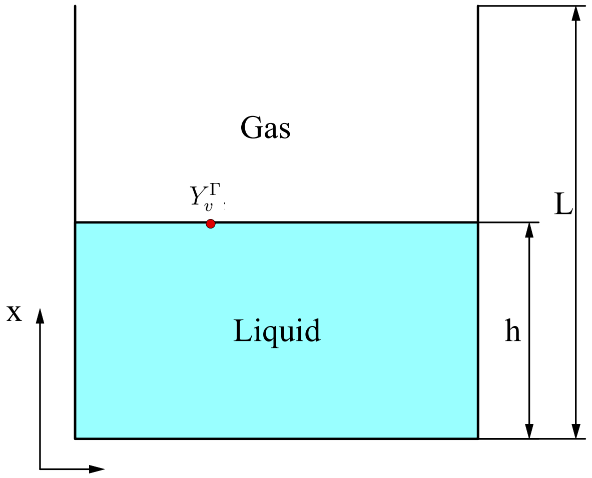

Figure 5.2: Sketch of the physical model for the evaporation of a planar surface.

The problem described above can be solved analytically. First, from the mass conservation equation in steady-state, we have (Safari et al. (2014)):

$$\frac{d\dot{m}}{dx} = \frac{d(\rho u)}{dx} = 0, \tag{5.7}$$

then the mass flux through the interface in this isothermal evaporation of the surface is constant:

$$\dot{m} = \rho u = \dot{m}_v'' + \dot{m}_g'' = constant, \tag{5.8}$$

where $\dot{m}_v''$ and $\dot{m}_g''$ are the vapor and gas mass fluxes through the surface respectively. Since the mass flux of gas is equal to zero, the vapor mass fraction equation can be written as:

$$\dot{m}_v'' = Y_v \dot{m}_v'' - \rho D_{vg} \frac{dY_v}{dx}, \tag{5.9}$$

where Y_v is the local vapor mass fraction that depends on the x direction and D_{vg} is the binary mass diffusivity of the gas and vapor. Equation 5.9 must be solved for the boundary conditions:

$$Y_v(h) = Y_v^\Gamma; \qquad Y_v(L) = Y_\infty, \tag{5.10}$$

where Y_v^Γ is the vapor mass fraction at the interface and and Y_∞ is the vapor mass fraction at the gas phase (related to the relative humidity). Solving the differential equation 5.9 from $h \to \infty$, it is possible to find a solution for the vapor mass flux through the interface:

$$\dot{m}_v'' = -\frac{\rho D_{vg}}{L-h}\ln(1+B_y), \tag{5.11}$$

where B_y is the so called mass transfer number (Safari et al. (2014)) and is given by:

$$B_y = \frac{Y_v^\Gamma - Y_\infty}{1-Y_v^\Gamma}. \tag{5.12}$$

The vapor mass fraction profile $Y_v(x)$ can be found by the integration of the equation 5.9 from $h \to x$; namely

$$Y_v(x) = 1 - (1-Y_v^\Gamma)\exp\left(\ln(1+B_y)\frac{x-h}{L-h}\right). \tag{5.13}$$

The evaporation model described in the first section of this chapter was solved numerically using the finite-volume/front-tracking method in one dimension and compared with the analytical solution (eq. 5.13) in order to validate part of the evaporation model. In this case, the vapor mass fraction at the interface is kept constant due to the system is considered istohermal. In Figure 5.3, the vapor mass fraction is plotted as a function of the x direction, with the interface located at the middle of the container. As can be observed, the numerical and analytical solutions are practically indistinguishable. The maximum value of the vapor mass fraction is at the interface and reduces to attain the value of Y_∞ at the top wall of the container which in this case is zero.

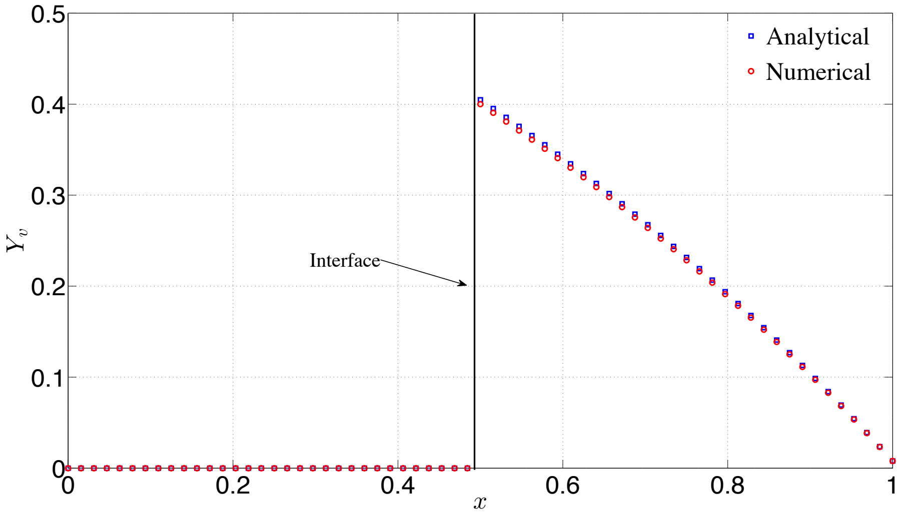

Figure 5.3: Vapor mass fraction profile.

It is also possible to compare the solution of the vapor mass flux through the interface calculated from the numerical solution of equation 5.4 and the analytical solution (eq. 5.11) for different mass transfer numbers. In Figure 5.4, such comparison is shown and we concluded that the numerical solution is reproducing very well the analytical solution of the model.

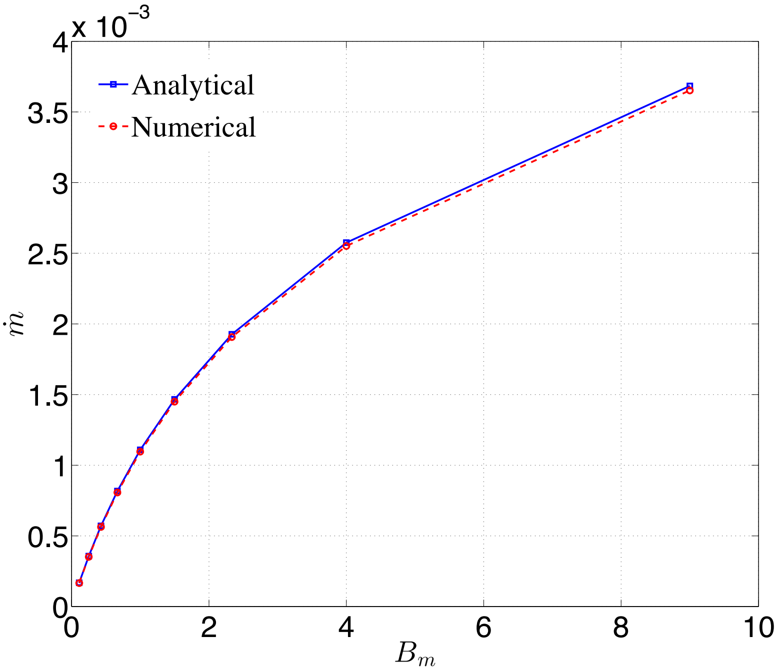

Figure 5.4: Vapor mass flux through the interface as a function of the evaporation number. The analytical solution corresponds to equation 5.11.

5.4 Evaporation of a droplet

Once the evaporation model was validated with a simple problem, the complete model described in section 5.2 was implemented in the front-tracking code in order to simulate the evaporation of droplets in two-dimensions. In Figure 5.5, a sketch of the problem for a single droplet is shown. The droplet is initially near the top of the computational domain and falls due to the acceleration of gravity. For the momentum equations periodic boundary conditions are imposed on the top and bottom wall and outflow boundaries in the lateral walls of the domain. Such outflow conditions are necessary due to the generation of volume of vapor during the evaporation process. For the vapor mass fraction equation, periodic boundary conditions are used again in the top and bottom wall and a constant vapor mass fraction is imposed in the lateral walls as boundary conditions. For all the simulations the temperature of the droplet and the surrounding gas phase is always less than the boiling vaporization temperature of the liquid phase.

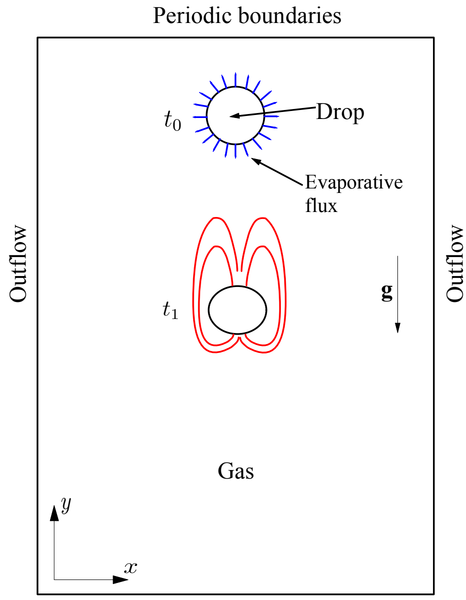

Figure 5.5: Sketch of the computational domain solved for the droplet evaporation problem.

The simulations reported in this thesis were performed using two-hypothetical fluids with material properties reported in Table 5.1. The conservation equations were discretized in an uniform mesh of 256 × 256 grid points. In the first simulation of the evaporation of a single droplet, the initial temperature in all the domain is fixed $T = 0.5$, the lifetime of the droplet can be calculated by the decreasing of the area of the droplet. In Figure 5.6, the evolution of the area of the droplet as a function of time is plotted; it can be observed that the first stage of the evaporation consists of a rapid evaporation in which the area as a function of time decreases almost linearly. In a second stage, the mass flux at the interface reduces since the air near the droplet is saturated with the vapor and the evaporation process is slower than in the first stage.

Kinematic viscosity ratio(ν_l/ν_g)	10
Density ratio (ρ_l/ρ_g)	10
Thermal diffusivity ratio (α_g/α_l)	10
Latent heat of vaporization (L)	2
Acceleration of gravity (g)	2
Surface tension (σ)	0.1
Binary diffusion coefficient (D_{vg})	0.001

Table 5.1: Flow conditions for the simulations.

In Figure 5.7, the vapor mass fraction fields are shown at the different times marked

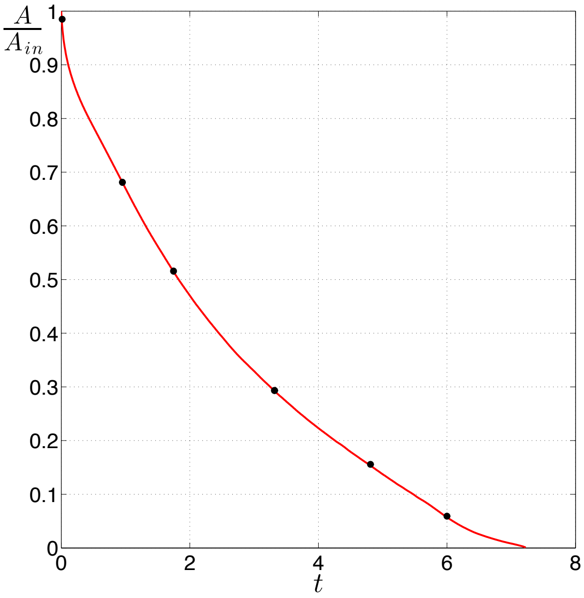

Figure 5.6: Evolution of the area of the droplet as a function of time.

with a black dot in Figure 5.6. The droplet falls by the acceleration of gravity and starts to evaporate, and as it was expected, the highest concentration of the vapor mass fraction is at the interface. Also, the elongated dipolar vortex form in the wake behind the droplet concentrates more vapor mass fraction in the recirculation zones of the wake of the droplet. Then the evaporation is much more intense in the front of the drop where the gradients of vapor mass fraction are stronger than behind the drop, where the vapor plume is formed. In the first stages of the simulation, the droplet deforms from circular to an ellipse. However, as the drop loses mass, the shape is restored to a circle by the surface tension force. Due to the periodic boundary conditions imposed in the vertical direction, the vapor mass fraction accumulates at the central part of the computational domain. This can be observed in the lower panels of Figure 5.7. The last panel shows the vapor mass fraction field when the mass of the droplet is about 6% of the initial mass and the code runs until the mass is about 4% without any problems. However, it is important to highlight that once the size of the droplet is comparable with the mesh size, numerical errors appear and a wrong solution is obtained from the simulation.

The temperature fields for different stages of the evaporation process are plotted in Figure 5.8. Note that the constant temperature boundary conditions were imposed in the lateral walls of the domain for the energy equation (eq. 5.3). As it is shown, since the evaporation process requires energy, the gas that surrounds the droplet is cooled and the temperature at the surface of the droplet decreases. This effect is taken into account in the last term of the energy equation that is the latent heat required to evaporate a certain quantity of liquid at the interface of the droplet. Also, in the wake generated by the droplet the zones of low temperature mix with the zones of high temperature producing a temperature plume behind the droplet.

From eqs. 5.5 and 5.6, the vapor pressure and then the vapor mass fraction at the interface depends on the temperature difference between the local temperature and the boiling temperature. In Figure 5.9 the area of the droplet as a function of time is plotted for different initial temperatures. Also, in the left panel of the Figure, the average mass flux is plotted as a function of time for the same three cases. The average mass flux at the interface was calculated as:

$$\dot{m}_{av} = \frac{1}{S}\int_S \dot{m}'' ds. \tag{5.14}$$

As it can be observed, the lifetime of the droplet decreases as the initial temperature of the gas is increased. Also, as it was expected, the average mass flux depends directly on the initial temperature, as the temperature increases the average flux. After an initial short time the average mass flux remains almost constant during the simulations; this can be explained by the fact that the gradients of the vapor mass fraction decreases because the gas that surrounds the droplet is saturated by the vapor and the average of vapor mass fraction at the interface is almost constant.

5.5 Evaporation of multiple droplets

In order to analyze the influence of the droplet-droplet interactions during the evaporation process, the code was extended to simulate multiple droplets. In Figure 5.10, the results of a simulation of three droplets is presented. Initially the droplets are at the top of the computational domain separated by a distance of two diameters. Snapshots of the vapor mass fraction field are shown. In this case, the initial temperature is $T = 0.75$ and the material properties of the fluids are the same as shown in Table 5.1, but the simulation was done in a larger domain and using a mesh with 512×512 grid points. When the vapor plume behind the front droplet saturates of vapor the region to be occupied by the middle and back droplets, the vapor mass fraction gradient at the interface of those droplets decreases and the evaporation is slower than in the front droplet. Since the front droplet evaporates faster than the others, the middle droplet reaches and deviates it from its natural path (see panel d) of Figure 5.10). This is caused by two effects: first, because of the low pressure zone created by the front droplet that produces an over-acceleration to the other droplets and second, since the front droplet loses mass much faster than the others, the velocity of the first droplet also decreases much faster than the velocity of the other droplets as it evaporates. However, once the middle droplet takes the front position the evaporation rate increases and it losses mass quickly such that its falling velocity is reduced and the back droplet is able to reach it (see panel f) of Figure 5.10).

The same description can be appreciated from Figure 5.11 where the area of the droplets as a function of time is plotted. The strongest interaction is between the middle and back droplet. As can be seen, the evaporation rate is slower in the middle droplet since the vapor generated by the others saturates the surrounding gas and the mass flux decreases. However, once the middle droplet reaches the front one, the evaporation process is faster at the interface of such droplet than at the back droplet. Finally, once the back droplet change the path of the middle one, the evaporation rate seems to be equal at the two droplets since the the curves of the evolution of the areas are approximately parallel.

As was commented, the extension of the evaporation model to three dimensions is almost straightforward. The model is able to capture the physical effects that occurs during the evaporation of droplets and it can be used to analyze the parameters that govern the evaporation process at different flow conditions. In the case of the evaporation of multiple droplets, systematic simulations in a larger domain are required in order to study the interactions of the droplets and analyze in a quantitative way the effect on the evaporation process.

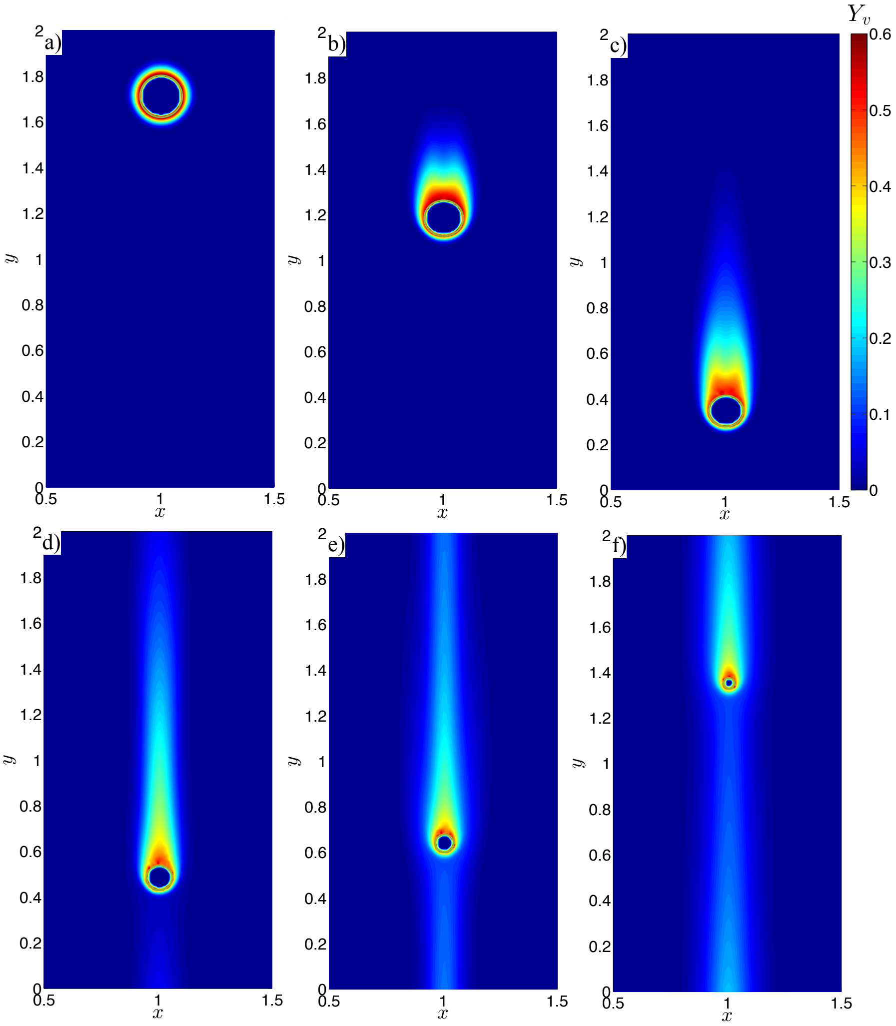

Figure 5.7: Temporal evolution of the vapor mass fraction field a) $t = 0.25$, b) $t = 1$, c) $t = 1.75$, d) $t = 3.25$, e) $t = 4.75$ and f) $t = 6$. The vapor mass fraction is color coded according to the color scale shown at the upper right side.

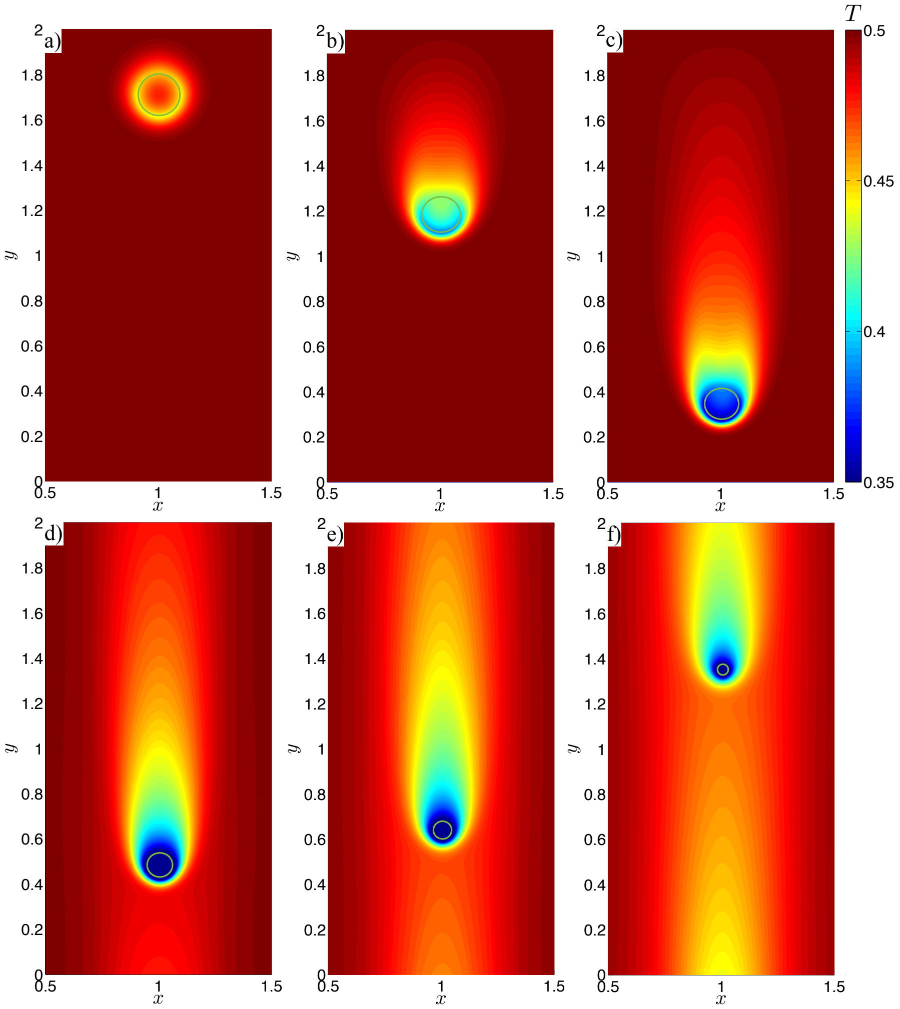

Figure 5.8: Temporal evolution of the temperature field a) $t = 0.25$, b) $t = 1$, c) $t = 1.75$, d) $t = 3.25$, e) $t = 4.75$ and f) $t = 6$.

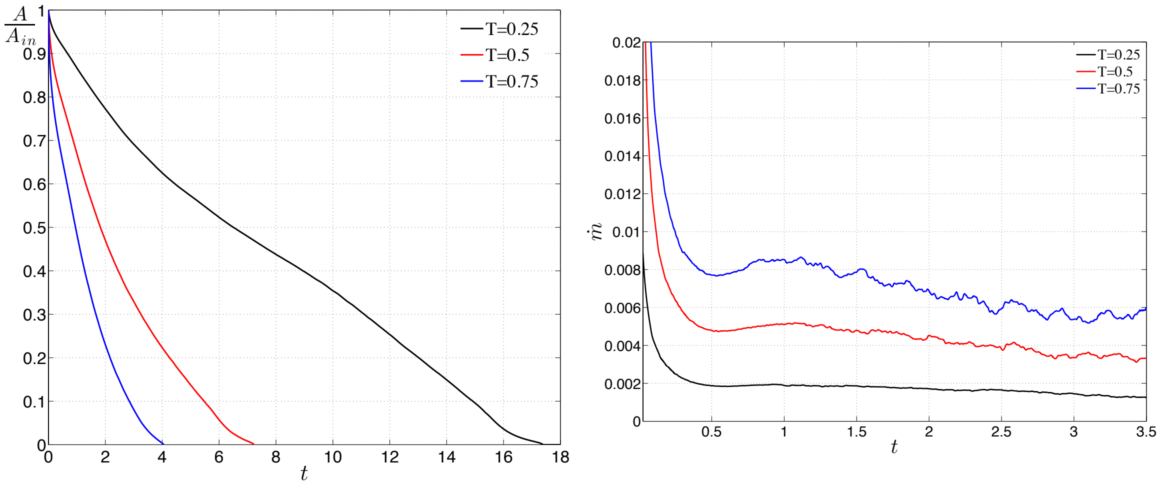

Figure 5.9: Left panel: Evolution of the droplet area as a function of time for different initial temperatures. Right panel: Average mass flux as a function of time for different initial temperatures.

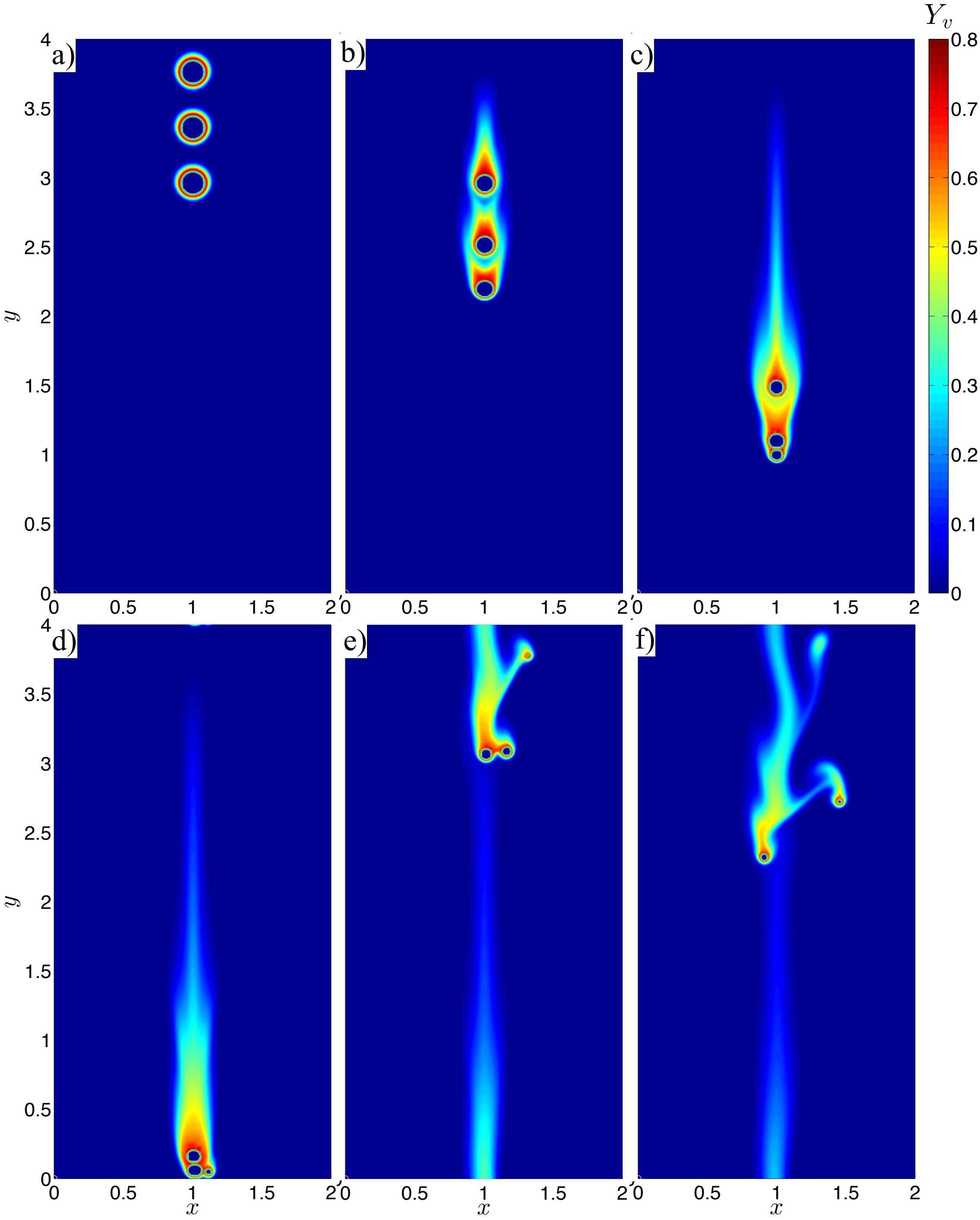

Figure 5.10: Temporal evolution of the vapor mass fraction field a) $t = 0.25$, b) $t = 1.25$, c) $t = 2.25$, d) $t = 3.75$, e) $t = 3.75$, f) $t = 4.5$.

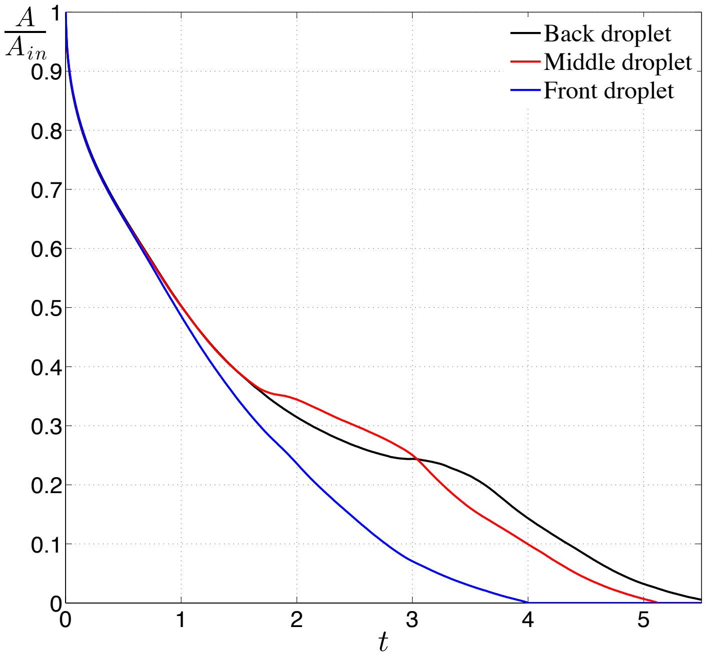

Figure 5.11: Evolution of the areas of the three droplets as a function of time.

Chapter 6

Simulation of a VAWT using the immersed boundary method

In order to demonstrate the versatility of the immersed boundary methods, the implementation of direct numerical simulations of a Vertical Axis Wind Turbine (VAWT) is carried out. The mathematical model to include solid bodies as immersed boundaries was developed adapting the front-tracking method described in the previous chapters of this thesis. The code was written in CUDA C in order to take the advantages of the GPU architecture to parallelize the solution of the linear systems. Here only the implementation of the model and preliminary results are reported, since the main objective of this chapter is to demonstrate that the model and code can be used in a totally different physical context.

6.1 Mathematical and numerical models

Consider a fluid in which one or more solids can be immersed with an arbitrary shape, if we use a regular grid to discretize the domain, some of the control volumes will be in the fluid region and others inside the solids. In order to identify cells inside and outside the solid, we define an indicator field as follows (Tryggvason et al. (2011)):

$$\mathbf{I}(\mathbf{x}) = \begin{cases} 1 & \text{inside the fluid,} \\ 0 & \text{inside the solid.} \end{cases} \tag{6.1}$$

The velocity in any cell of the computational domain is given by:

$$\mathbf{u}(\mathbf{x}) = I(\mathbf{x})\mathbf{u}_f(\mathbf{x}) + (1 - I(\mathbf{x}))\mathbf{u}_s(\mathbf{x}), \tag{6.2}$$

where $\mathbf{u}_f$ is the velocity in the fluid region and $\mathbf{u}_s$ is the velocity of the solid. The velocity in the fluid is dictated by the mass and momentum conservation equations for incompressible flows:

$$\nabla \cdot \mathbf{u}_f = 0. \tag{6.3}$$

$$\frac{\partial \mathbf{u}_f}{\partial t} + \nabla \cdot \mathbf{u}_f \mathbf{u}_f = -\frac{\nabla p}{\rho} + \nu \nabla^2 \mathbf{u}_f, \tag{6.4}$$

where p is pressure and ν is the kinematic viscosity of the fluid. The motion of the rigid body is modeled by the Newton-Euler equations (Glowinski et al. (2001)):

$$F = m\frac{d\mathbf{u}_s}{dt}, \tag{6.5}$$

$$\tau = I\frac{d\omega}{dt}, \tag{6.6}$$

where m is the mass and I is the moment of inertia of the solid body. The coupling between the equations in the fluid and the solid regions is the hydrodynamical force (F) and the torque (τ) acting over the solid. In order to calculate the hydrodynamical force, the integral of the stress tensor over the surface of the body is calculated (see equation 2.3 of Chapter 2). The strategy of the solution of the set of equations presented above is practically the same as that developed in the case of the rising of bubbles. Also, the same parallelization technique was implemented in order to accelerate the computations.

6.2 Results

6.2.1 Cylinder rotating around a circle

Before simulating the flow around a VAWT, the model was applied to a simpler problem in which a cylinder rotates around a circle. In Figure 6.1, a sketch of the problem is shown. A uniform flow from left to right interacts with a cylinder that is constrained to move around a circle marked with a dashed line in the figure. The computational domain consists in a rectangle with free slip boundary conditions at the upper and bottom walls, inlet flow on the left and outflow on the right wall. The domain was discretized with a regular grid of 384 X 192 control volumes in the x and y directions, respectively. The model described in the previous section is used to simulate this problem, according to the following steps. First, the Navier-Stokes equations are solved using the standard finite-volume method; then the hydrodynamical force and torque are calculated and used in the Newton-Euler equations to calculate the translational and angular velocities of the solid body. In general, for an arbitrary motion of a solid body immersed in a fluid, both Newton-Euler equations must be solved to calculate the velocity of the solid body; however, in the case described in Figure 6.1, those equations are simplified by using the constraint that the motion is limited to a circle. Then, the translational velocity of the cylinder can be calculated as (Juarez & Glowinski (2003)):

$$\mathbf{u}_s = l\omega(\cos\phi, \sin\phi), \tag{6.7}$$

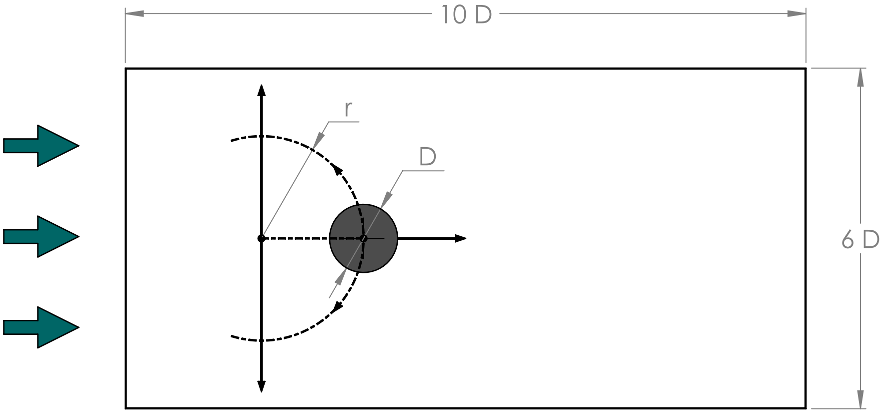

Figure 6.1: Sketch of the problem.

where l is the distance from the center of the cylinder to the center of rotation and ϕ is the angle formed by the position of the cylinder respect to the horizontal. With this simplification, only equation 6.6 is required to calculate the velocity of the rigid body.

In Figure 6.2, the vorticity field at two instants of time is plotted for the flow around a cylinder with $Re = 250$. The simulation starts with the cylinder at the position of panel a) and as is shown the classic vortex street is developed in the wake of the cylinder. After a certain period of time, the cylinder is released and is free to rotate around the circle. At this point, the hydrodynamical torque with respect to the center of the circle moves the cylinder to the position shown in panel b). In Figure 6.3, the position of the centroid of the cylinder as a function of time was plotted. As can be observed, the initial position of the cylinder is at $\phi = \pi/2$; once the cylinder is released, the position changes quickly to $\phi = 0$. The simulation correctly predicts the motion of the cylinder when the vector of the hydrodynamical force and the vector of the position of the cylinder taking as reference the center of rotation produce a torque. However, once the position is $\phi = 0$, those vectors are parallel and the torque is zero, then the cylinder stays at this position oscillating with a tiny frequency due to the non-axisymmetric pressure field behind the cylinder.

6.2.2 Numerical simulation of a VAWT

The VAWT is a wind turbine where the main rotor shaft and the airfoils are set transversal to the wind. On the left side in Figure 6.4, the configuration of a three blades VAWT is shown. The most important advantage of these wind turbines is that they do not need to face into the wind to be useful, no matter which direction the wind is coming from, it will rotate the blades. However, the efficiency of such wind turbines is very low, and a detailed understanding of the aerodynamics of the wind-blade interaction is useful for optimizing the performance. In order to simplify the mathematical model, the simulations were performed in two dimensions. This simplification is suitable since the height of the

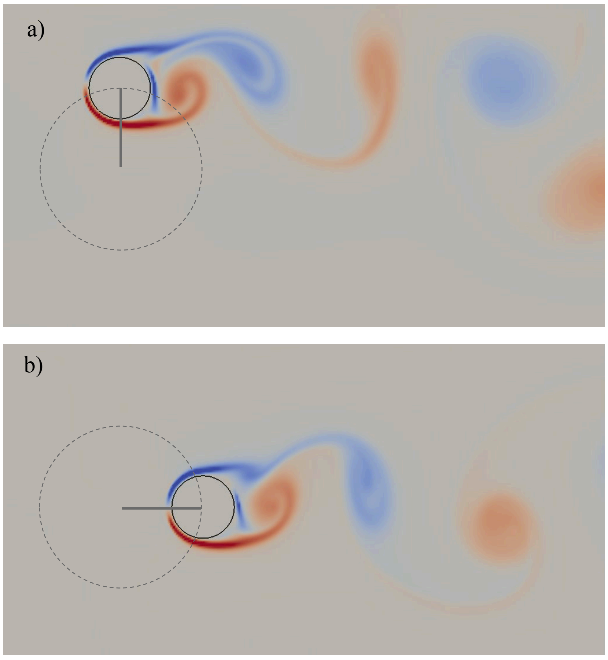

Figure 6.2: Vorticity field around a cylinder at two instants of time during its rotation over a fixed circle.

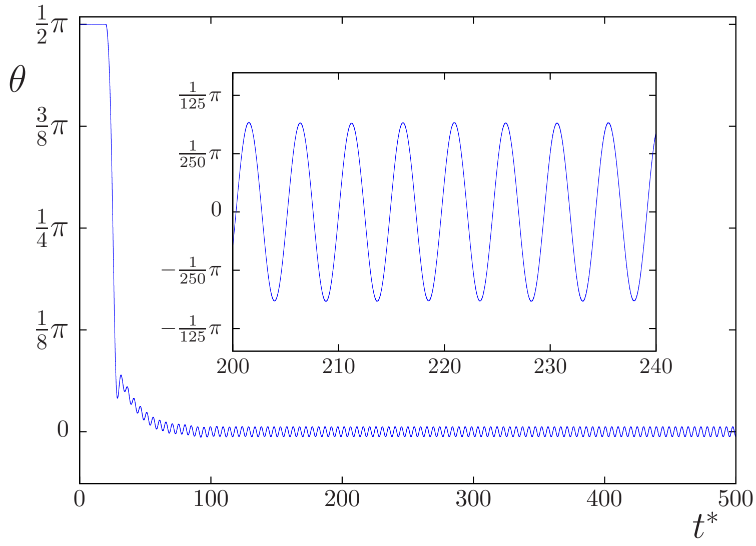

Figure 6.3: Vorticity field around a cylinder at two instants of time during its rotation around a fixed point.

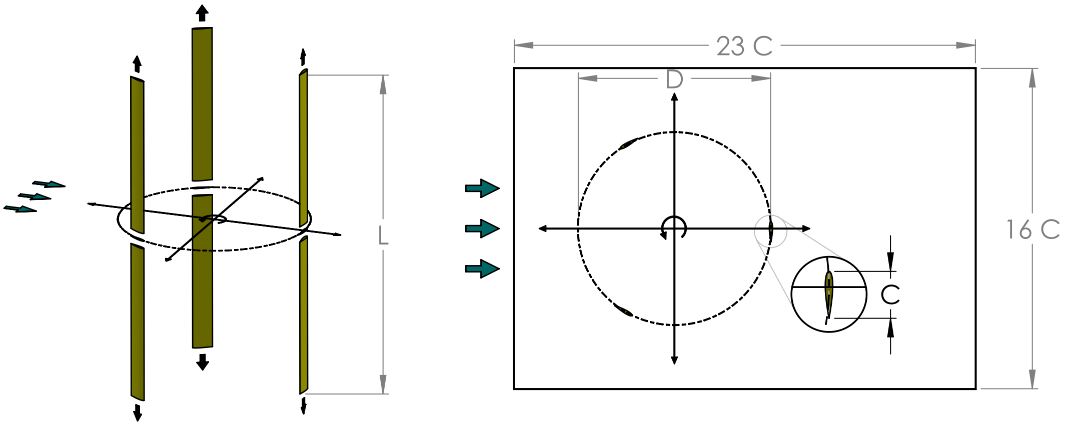

Figure 6.4: Sketch of the physical model for the VAWT.

turbine is very large compared with the core of the aerodynamical profile. On the right hand side of Figure 6.4, the physical model is presented; the characteristic length of the problem is the core of the airfoil (C) and the computational domain consists of three airfoils separated uniformly by an angle of $3\pi/2$ from each other within a rectangular region. The distance from the centroid of the airfoil to the center of rotation of the wind turbine is 4.8C. A uniform flow comes from left to right and interacts with the three blades of the VAWT. Any blade profile can be simulated in the code, but the simulation was made using the NACA0010 profile. For the solution of the Navier-Stokes equations, outlet boundary condition in the right edge of the computational domain and free-slip boundaries in the top and bottom walls were imposed. The computational domain presented in Figure 6.4 was discretized in a mesh with 2944×2048 grid points in which the Navier-Stokes and the second Newton-Euler equation (equations 6.3, 6.4 and 6.6) were solved.

In Figure 6.5, a snapshot of the vorticity field around the blades of the VAWT is shown and the circle and center of rotation of the blades are also plotted. In this simulation, the Reynolds number based on the length of the core of a blade is 500. As can be observed, the wake behind each airfoil depends on the position that is changing as the VAWT rotates. However, vortex shedding occurs behind the three airfoils. The vortices detached in the wake of the blade, that is in the upstream position, affects the flow over the blade in the downstream position. Such interactions can alter the torque on the downstream blade and the efficiency of the VAWT can be strongly affected. The main idea of this project in the near future, is to study in detail the blade-wake interactions in order to find the optimum configuration of the VAWT at different flow conditions. It is important to mention, that in the simulation of Figure 6.5, the VAWT does not revolve with a uniform velocity; the turbine moves certain angle, stops and again moves back. This oscillatory motion can be caused by the interactions of the vortices detached by the blades affecting the others.

In order to quantify the momentum transmitted from the flow to the VAWT, the torques over each blade and the total torque are plotted in Figure 6.6. It can be observed that the

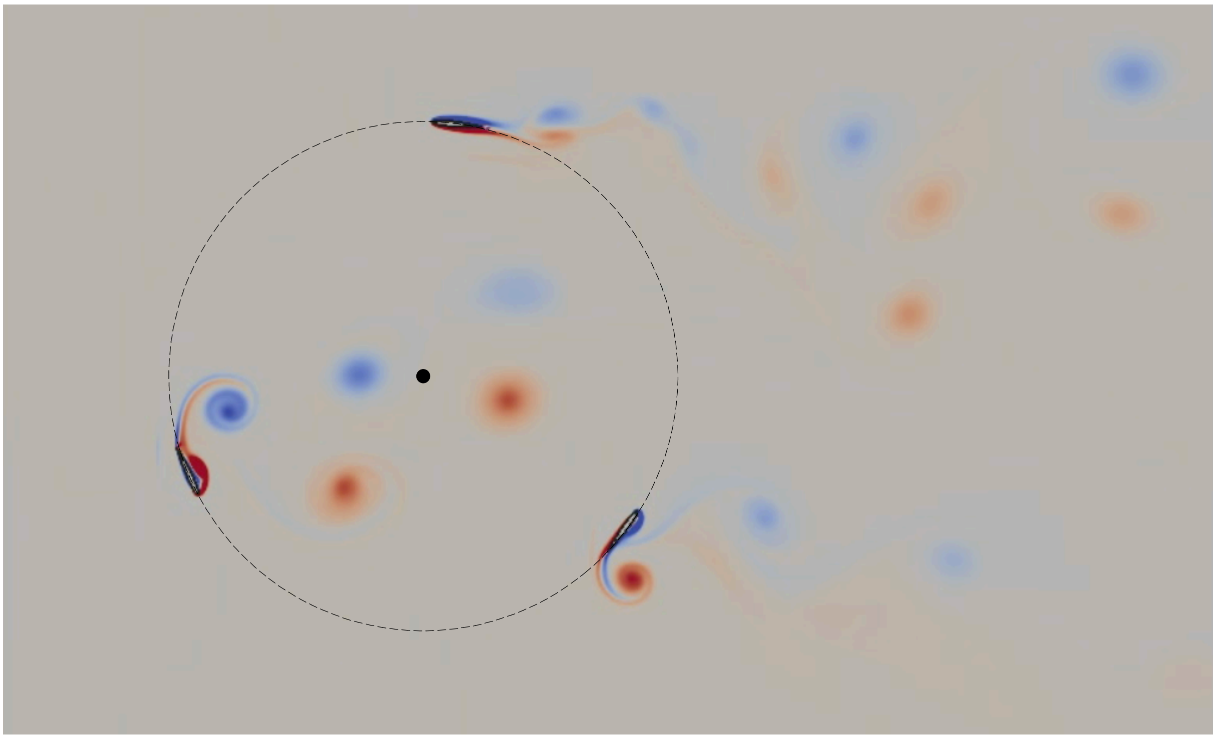

Figure 6.5: Vorticity field of the flow generated by the VAWT.

torque in all cases oscillates around zero, and it is clear that in many instants of time the torque over one airfoil has an opposite direction with respect to the torque over another one of the blades. This means that at those instants of time the torques act against each other. This combination of forces and torques directly affects the behavior and efficiency of the VAWT. With an adequate configuration, those losses of energy can be suppressed or minimized.

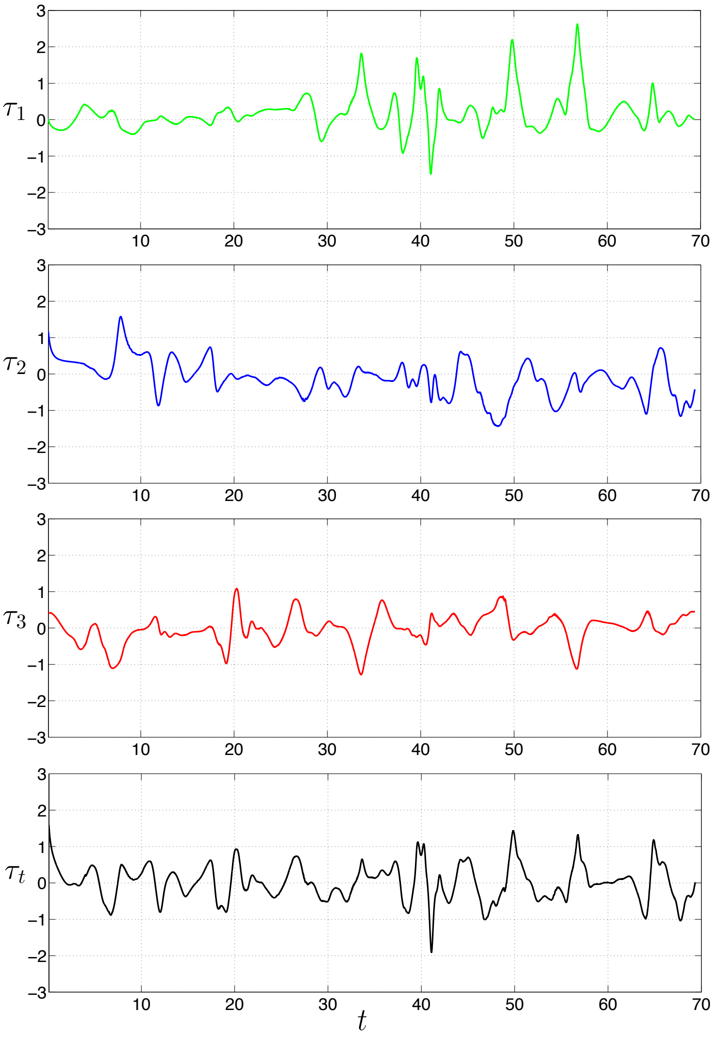

Figure 6.6: Hydrodynamical torque generated at the center of rotation of the VAWT by each blade and the Total torque.

Conclusions

The front-tracking method coupled with the solution of the conservation equations was implemented in order to compute bubbly flows in two and three dimensions adding the heat and mass transfer phenomena. The analysis of bubble dynamics were carried out in two and three dimensions separately and the results showed the differences in the motion of the bubbles and the wake developed behind the bubbles. Also, the numerical implementation was optimized using the advantage of the architecture of the GPU's in order to accelerate the solution of the conservation equations. The pressure and indicator function Poisson equations were solved using the CUSP library from CUDA that allows an efficient storage of sparse diagonal matrices and contains robust solvers that allow us to simulate air-water systems.

In the first part of this project the detailed study of the bubble dynamics in two dimensions were described by means of a numerical solution of the finite volume/front-tracking method. The analysis was focused on examples where the ratio of the density of the fluid to the density of the gas in the bubble is 10^3 and the simulations were made for a long enough time to consider that the dynamics are not influenced by the initial conditions. Also, we compared the numerical results with the observations of the ascent of bubbles in a Hele-Shaw cell which constitutes a physical model that approximates the conditions considered in the calculations. The bubble dynamics in two dimensions can be conceptually decomposed in four parts: vertical and horizontal motions, bubble rotation and the deformation of the shape of the bubble. The vertical displacement is promoted by buoyancy and is resisted or assisted by the vertical components of the force on the bubble. The asymmetric forces acting on the bubble due to vorticity generation promote forces with components non parallel to the instantaneous displacement vector. Besides the two translational motions, the bubble also rotates. Finally, there is the deformation of the bubble surface due to the interplay between the stresses and surface tension forces. For the water-air case where we have put the emphasis of our analysis, we find that the surface tension is dominant and the originally circular shape of the bubbles undergoes only a small deformation to take the shape of an ellipse. The most relevant consequence of the deformation is that vorticity is generated more efficiently than in a circular bubble since there are zones with smaller radius of curvature. The present study provides an interesting example of the advantages and limitations of using a two dimensional simulation for interpreting the three dimensional phenomenon that occurs in a Hele-Shaw cell. Specifically, it is remarkable to conclude that the two dimensional model correctly predicts the linear relation between the Archimedes number and the terminal Reynolds number. It is also interesting to find that the slope increases (thereby reducing the difference between experiment and the two dimensional model) as the gap is larger. The vortex pattern in the wake behind a bubble when the diameter of the bubble is larger than the gap coincides with those of a von Karman vortex street, but when the diameter of the bubble is equal to the gap, the vortex distribution is a distorted von Karman distribution. This phenomenon may be of relevance in the design of parallel plate heat exchangers.

In the second part of the thesis, the results of the fully-three dimensional model implementation was presented. The results of the simulations for a single bubble at low Reynolds numbers for different flow conditions were shown and the qualitative shape of the bubbles were in agreement with the experimental results reported by Clift et al. (1978). The wake behind the bubbles is formed by two elongated vortices and the flow at these conditions is axis-symmetric. When the Reynolds number increases, the numerical results showed that the vortices in the wake break down due to the instabilities that appear in the pressure field. The consequence of the vortices breaking in the wake of the bubble is the continuous vortex shedding behind the bubble which produces horizontal forces that promote a lateral motion. Under these conditions, the bubble follows a spiral trajectory. Also, the rising velocity oscillates around an average value with a frequency that is twice the frequency of the oscillation of the motion of the bubble. The rising velocity calculated from the numerical simulations was compared for different flow conditions with experimental data reported for two different authors and the values obtained are in agreement within an error that is less than 7% for all cases. It is important to highlight that very few authors have reported the quantitative comparison of the direct numerical simulations of bubble dynamics with experiments due to the difficulties to simulate bubbly flows in which the density ratio is 1/1000. With our implementation, the comparison is direct and all the parameters used to perform the simulations correspond to the material properties of air-water systems.

The model was extended to simulate a system with multiple bubbles. We used the code to solve two cases and the results correctly showed that small bubbles ascend in a straight path and that the bubble-wake interactions can cause a dramatic changes in the trajectories. In the case of larger bubbles, we found spiral paths. Only some local alterations in the trajectories of the bubbles can be observed due to the bubble-wake interactions and the qualitative behavior of the flow is not globally affected. The dynamics of multiple bubbles is very complex and systematic studies can be carried out with the code developed in this thesis in order to try to understand some features of such phenomenon, but we only displayed representative examples.

With the purpose of studying the heat transfer in bubbly flows, the energy equation was added to the finite volume/front-tracking code and a detailed study of bubbly flows in inclined channels was carried out. The main objective of such study was to quantify the effect of the angle of inclination on the flow and the heat transfer. From the results we conclude that for the turbulent flows some alterations were found in the flow as one changes the inclination angle. For sloping channels the bubbles migrate to the top wall and form layers that improve the mixing of the fluid but reduce the fluid velocity compared to the single phase flow. The results also show that even when the flow structure is dependent on the angle of inclination, it has little effect on the global heat transfer into the channel. However, some local changes in the heat transport are observed in the average temperature profiles across the channel. On the other hand, for laminar flows it was found that the flow and also the heat transfer depends strongly on the angle of the channel. The Nusselt number measured on the top wall of the channel increases as we change the angle until it reaches a maximum between 30° and 60°. Then, the Nusselt number decreases as the inclination angle goes to 90°. This effect was also clarified by analyzing the temperature profiles for the different cases. For the sloping channels it was observed that the mixing generated by the bubbles near the top wall of the channel decreases the temperature since the heat is better transported from the wall to the core of the fluid for those cases.

In order to implement the mass transfer in two-phase flows, a two-dimensional model for the evaporation phenomenon was developed and coupled with our two dimensional finite volume/ front-tracking code. The first results for the evaporation of a planar surface were validated with a simple analytical model. Simulations of the evaporation of a single and multiple droplets were carried out and the results showed that the implementation captures the main physical effects that occur during the evaporation process. Also, it is important to highlight that the extension to the three dimensional code is straightforward.

Finally, the mathematical model and the numerical implementation to simulate a Vertical Axis Wind Turbine was developed and some preliminary results of the simulations were presented.

Bibliography

Aboulhasanzadeh, B., Hosoda, S., Tomiyama, A. & Tryggvason, G. (2013), 'A validation of an embedded analytical description approach for the computations of high Schmidt number mass transfer from bubbles', *Chem. Eng. Sci.* **101**, 165–174.

Aboulhasanzadeh, B., Thomas, S., Taeibi-Rahni, M. & Tryggvason, G. (2012), 'Multiscale computations of mass transfer from buoyant bubbles', *Chem. Eng. Sci.* **75**, 456–467.

Andersen, A., Pesavento, U. & Wang, J. Z. (2005), 'Unsteady aerodynamics of fluttering and tumbling plates', *J. Fluid Mech.* **541**, 65–90.

Banerjee, R. (2013), 'Numerical investigation of evaporation of a single ethanol/iso-octane droplet', *Fuel* **107**, 724–739.

Bhaga, D. & Weber, M. (1981), 'Bubbles in viscous liquids: shapes, wakes and velocities', *J. Fluid Mech.* **105**, 61–85.

Bunner, B. & Tryggvason, G. (2002*a*), 'Dynamics of homogeneous bubbly flows part 1. rise velocity and microstructure of the bubbles', *J. Fluid Mech.* **466**, 17–52.

Bunner, B. & Tryggvason, G. (2002*b*), 'Dynamics of homogeneous bubbly flows part 2. velocity fluctuations', *J. Fluid Mech.* **466**, 53–84.

Chahed, J., Roig, V. & Masbernat, L. (2003), 'Eulerian-eulerian two-fluid model for turbulent gas-liquid bubbly flows', *Int. J. Multiphase Flow* **29**, 23–49.

Chen, L., Garimella, S., Reizes, J. & Leonardi, E. (1999), 'The development of a bubble rising in a viscous liquid', *J. Fluid Mech.* **387**, 61–96.

Clift, R., Grace, J. & Weber, M. (1978), *Bubbles, drops and particles*, Academic Press.

Dabiri, S. & Tryggvason, G. (2015), 'Heat transfer in turbulent bubbly flow in vertical channels', *Chem. Eng. Sc.* **122**, 106–113.

de Vries, A. (2001), Path and wake of a rising bubble, PhD thesis, Twente University, The Netherlands.

Deen, N. & Kuipers, J. (2013), 'Direct numerical simulation of wall-to liquid heat transfer in dispersed gas-liquid two-phase flow using a volume of fluid approach', *Chem. Eng. Sci.* **102**, 268–282.

Deen, N., van Sint Annaland, M. & Kuipers, J. (2006), ‘Direct numerical simulation of heat transport in dispersed gas-liquid two-phase flow using a front tracking approach’, *Fifth International Conference on CFD in the Procedure Industries* .

Donnelly, B., O’donovan, T. & Murray, D. (2009), ‘Surface heat transfer due to sliding bubble motion’, *Applied Thermal Engineering* **29**, 1319–1326.

Drew, D. & Passman, S. (1999), *Theory of multicomponent fluids*, 1 edn, Springer-Verlag.

Esmaeeli, A. & Tryggvason, G. (1999*a*), ‘Direct numerical simulations of bubbly flows. Part 1. Low Reynolds number arrays’, *J. Fluid Mech.* **385**, 325–358.

Esmaeeli, A. & Tryggvason, G. (1999*b*), ‘Direct numerical simulations of bubbly flows. Part 2. Moderate Reynolds number arrays’, *J. Fluid Mech.* **385**, 325–358.

Esmaeeli, A. & Tryggvason, G. (2004*a*), ‘Computations of film boiling. Part I: Numerical method’, *Intnl J. Heat Mass Transfer* **47**, 5451–5461.

Esmaeeli, A. & Tryggvason, G. (2004*b*), ‘Computations of film boiling. Part II: Multimode film boiling’, *Intnl J. Heat Mass Transfer* **47**, 5463–5476.

Gibson, J. F. (2014), Channelflow: A spectral Navier-Stokes simulator in C++, Technical report, U. New Hampshire. `Channelflow.org`.

Glowinski, R., Pan, T., Hesla, T., Joseph, D. & Périaux, J. (2001), ‘A fictitious domain approach to the direct numerical simulation of incompressible viscous flow past moving rigid bodies: Application to particulate flow’, *J. Comput. Phys.* **169**, 363–426.

Gunsing, M. (2004), Modelling of bubbly flows using volume of fluid, front tracking and discrete bubble models, PhD thesis, Twente University, The Netherlands.

Horowitz, M. & Williamson, C. (2010), ‘The effect of Reynolds number on the dynamics and wakes of freely rising or falling spheres’, *J. Fluid Mech.* **651**, 251–294.

Hua, J. & Lou, J. (2007), ‘Numerical simulation of bubble rising in viscous liquid’, *J. Comput. Phys.* **22**, 769–795.

Johnson, S., Thompson, M. & Hourigan, K. (2001), ‘Flow past elliptical cylinders at Low Reynolds Numbers’, *Proceedings 14th Australasian Fluid Mechanics Conference* .

Juarez, L. & Glowinski, R. (2003), ‘Numerical simulation of the motion of pendula in an incompressible viscous fluid by Lagrange multiplier/fictitious domain method’, *Fourteenth International Conference on Domain Decomposition Methods* .

Kashinsky, O., Randin, V. & Chinak, A. (2013), ‘The effect of channel orientation on heat transfer and wall shear stress in the bubbly flow’, *Thermophysics and Aeromechanics* **20**, 391–398.

Kashinsky, O., Randin, V. & Chinak, A. (2014), 'Heat transfer and shear stress in a gas-liquid flow in an inclined flat channel', *J. Eng. Thermophys.* **23**, 39–46.

Kawamura, H., Ohsaka, K., Abe, H. & Yamamoto, K. (1998), 'DNS of turbulent heat transfer in channel flow with low to medium-high Prandtl number fluid', *Int J.,Heat Fluid Flow* **19**, 482–491.

Kelley, E. & Wu, M. (2005), 'Path instabilities of rising air bubbles in a Hele-Shaw cell', *Phys. Rev. Lett.* **79**, 1265–1268.

Kitagawa, A. & Murai, Y. (2013), 'Natural convection heat transfer from a vertical heated plate in water with microbubble injection', *Chem. Eng. Sc.* **99**, 215–224.

Kozuka, M., Seki, Y. & Kawamura, H. (2009), 'DNS of turbulent heat transfer in a channel flow with a high spatial resolution', *Int J.,Heat Fluid Flow* **30**, 514–524.

Lu, J., Fernandez, A. & Tryggvason, G. (2005), 'The effect of bubbles on the wall drag in a turbulent channel flow', *Phys. Fluids* **17**.

Lu, J. & Tryggvason, G. (2006), 'Numerical study of turbulent bubbly downflows in a vertical channel', *Phys. Fluids* **18**.

Lu, J. & Tryggvason, G. (2008), 'Effect of bubble deformability in turbulent bubbly upflow in a vertical channel', *Phys. Fluids* **20**.

Maxworthy, T. (1986), 'Bubble formation, motion and interaction in a Hele-Shaw cell', *J. Fluid Mech.* **173**, 95–114.

Mingming, W. & Morteza, G. (2002), 'Experimental studies on the shape and path of small air bubbles rising in clean water', *Phys. Fluids* **14**, 49–52.

Mougin, G. & Magnaudet, J. (2002), 'Path instability of a rising bubble', *Phys. Rev. Lett.* **88**, 1.

Ohta, M., Imura, T., Yoshida, Y. & Sussman, M. (2005), 'A computational study of the effect of initial bubble conditions on the motion of a gas bubble rising in viscous liquids', *Intnl J. Multiphase Flow* **31**, 223–237.

Ormieres, D. & Provansal, M. (1999), 'Transition to turbulence in the wake of a sphere', *Phys. Rev. Lett.* **83**, 80–83.

Perry, A., Chong, M. & Lim, T. (1982), 'The effect of Reynolds number on the dynamics and wakes of freely rising or falling spheres', *J. Fluid Mech.* **116**, 77–90.

Peskin, C. (1977), 'Numerical analysis of blood flow in the heart', *J. Comput. Phys.* **25**, 220–252.

Pfleger, D., Gomes, S., Gilbert, N. & Wagner, H. (1999), 'Hydrodynamic simulations of laboratory scale bubble columns fundamental studies of the eulerian-eulerian modeling approach', *Chem. Eng. Sc.* **54**, 5091–5099.

Piedra, S. (2011), 'Numerical simulations of bubble dynamics in two-dimensions', *Master's thesis. Universidad Nacional Autónoma de México, Mexico* .

Piedra, S., Lu, J., Ramos, E. & Tryggvason, G. (2015), 'Numerical study of the flow and heat transfer of bubbly flows in inclined channels', *Submitted to Intnl J. Heat Fluid Flow* .

Piedra, S. & Ramos, E. (2012), Dynamical interaction of bubbles in two dimensions, *in* J. Klapp, A. Cros, O. Velasco & C. Stern, eds, 'Experimental and Theoretical Advances in Fluid Dynamics', Springer-Verlag.

Piedra, S., Ramos, E. & Herrera, J. (2015), 'Dynamics of two dimensional bubbles', *Accepted in Phys. Rev. E* .

Prosperetti, A. & Tryggvason, G. (2007), *Computational Methods for Multiphase Flow*, Cambridge University Press.

Roig, V., Roudet, M., Risso, F. & Billete, A. (2012), 'Dynamics of a high-Reynolds-number bubble rising within a thin gap', *J. Fluid Mech.* **107**, 444–466.

Safari, H., Hassan-Rahimian, M. & Krafczyk, M. (2014), 'Consistent simulation of droplet evaporation based on the phase-field multiphase Lattice Boltzmann method', *Phys. Rev. E* **90**, 033305–1–033305–13.

Sanada, T., Shirota, M. & Watanabe, M. (2007), 'Bubble wake visualization by using photochromic dye', *Chem. Eng. Sci.* **62**, 7264–7273.

Sanada, T., Watanabe, M., Fukano, T. & Kariyasaki, A. (2005), 'Behavior of a single coherent gas bubble chain and surrounding liquid jet flow structure', *Chem. Eng. Sc.* **60**, 4886–4900.

Scardovelli, R. & Zaleski, S. (1999), 'Direct numerical simulation of free-surface and interfacial flow', *Annu. Rev. Fluid Mech.* **31**, 567–603.

Schlottke, J. & Weigand, B. (2008), 'Direct numerical simulation of evaporating droplets', *J. Comput. Phys.* **227**, 5215–5237.

Shew, W., Poncet, S. & Pinton, J. (2006), 'Force measurements on rising bubbles', *J. Fluid Mech.* **569**, 51–60.

Stene, J. (2010), Numerical Simulation of interfacial and multiphase flows using the front tracking method, PhD thesis, National University of Singapore, Singapore.

Sussman, M., Smereka, P. & Osher, S. (1994), 'A level set approach for computing solutions to incompressible two-phase flows', *J. Comput. Phys.* **114**, 146.

Tanguy, S., Thibaut, M. & Berlemont, A. (2007), 'A level set method for vaporizing two-phase flows', *J. Comput. Phys.* **221**, 837–853.

Tomiyama, A., Celata, G., Hosokawa, S. & Yoshida, S. (2002), 'Terminal velocity of single bubbles in surface tension force dominant regime', *Intnl J. Multiphase Flow* **28**, 1497–1519.

Troshko, A. & Hassan, Y. (2001), 'A two-equation turbulence model of turbulent bubbly flows', *Int. J. Multiphase Flow* **27**, 1965–2000.

Tryggvason, G., Bunner, B., Esmaeeli, A., Juric, D., Al-Rawahi, N., Tauber, W., Han, J., Nas, S. & Jan, Y. (2001), 'A front-tracking method for the computations of multiphase flow', *J. Comput. Phys.* **169**, 708–759.

Tryggvason, G., Scardovelli, R. & S., Z. (2011), *Direct numerical simulations of gas-liquid multiphase flows*, 1 edn, Cambridge Press.

van Sint Annaland, M., Deen, N. & Kuipers, J. (2005), 'Numerical simulation of gas bubbles behaviour using a three-dimensional volume of fluid method', *Chem. Eng. Sci.* **60**, 2999–3011.

van Sint Annaland, M., Dijkhuizen, W., Deen, N. & Kuipers, J. (2006), 'Numerical simulation of gas bubbles behaviour using a three-dimensional volume of fluid method', *AIChE J* **52**, 99–110.

Veldhuis, C., Biesheuvel, A. & van Wijngaarden, L. (2008), 'Shape oscillations on bubbles rising in clean and tap water', *Phys. Fluids* **20**, 040705–1–040705–12.

Versteeg, H. & Malalasekera, W. (1995), *An introduction to Computational Fluid Dynamics, The Finite Volume Method*, Prentice Hall.

Williamson, C. (1988), 'Defining a universal and continuous Strouhal-Reynolds number relationship for the vortex shedding of a circular cylinder', *Phys. Fluids* **31**, 2742–2744.

Williamson, C. (1996), 'Vortex dynamics in the cylinder wake', *Annu. Rev. Fluid Mech.* **28**, 477–539.

Williamson, C. & Roshko, A. (1988), 'Vortex formation in the wake of an oscillating cylinder', *J. Fluids Struct.* **2**, 355–381.

Zhang, D., Deen, N. & Kuipers, J. (2006), 'Numerical simulation of the dynamic flow behavior in a bubble column: A study of closures for turbulence and interface forces', *Chem. Eng. Sc.* **61**, 7593–7608.

Zhao, P., Li, G. & Yusong, Y. (2014), 'Numerical simulation and experimental study of heat and mass transfer in fuel droplet evaporation', *Heat and Mass Transfer* **50**, 1145–1154.